

Development of a Control System to Improve the Stability of the FLUTE Electron Gun

(Entwicklung einer Regelung zur Verbesserung der
Stabilität der FLUTE Elektronen-Kanone)

Master thesis
of

Marvin-Dennis Noll

at the Institute for Beam Physics and Technology

Reviewer: Prof. Dr.-Ing. John Jelonnek (IHM)
Second Reviewer: Prof. Dr. Anke-Susanne Müller (IBPT)
Advisor: Dr. Nigel Smale (IBPT)

15.11.2020 – 07.07.2021

Erklärung zur Selbstständigkeit

Ich versichere wahrheitsgemäß, die Arbeit selbstständig angefertigt, alle benutzten Hilfsmittel vollständig und genau angegeben und alles kenntlich gemacht zu haben, was aus Arbeiten anderer unverändert oder mit Abänderungen entnommen wurde und dass ich die Satzung des KIT zur Sicherung guter wissenschaftlicher Praxis in der gültigen Fassung vom 24.05.2018 beachtet habe.

Karlsruhe, den 16.07.2021,

Marvin-Dennis Noll

Als Prüfungsexemplar genehmigt von

Karlsruhe, den 16.07.2021,

Prof. Dr.-Ing. John Jelonnek (IHM)

Contents

1	Introduction	3
2	Theoretical Framework	5
2.1	Relativistic Electrons	5
2.2	Signal Analysis	5
2.2.1	Auto Correlation and Cross Correlation	5
2.2.2	Estimating the Spectrum of a Stochastic Process	6
2.3	Feedback Control Systems	8
2.3.1	Disturbance Rejection and Input Tracking	9
2.3.2	Stability	9
2.4	Metrics to Quantify the Stability of a Signal	10
3	The Stability of FLUTE the Electron Gun and Proposed Stabilizing Solution	11
3.1	The Electron Gun	12
3.2	Relation between RF power and Electron Energy	14
3.3	Current RF Stability and Proposed Solution	14
4	Interfacing FLUTE	17
4.1	Inputs	17
4.1.1	Accessing EPICS channels in Python with PyEpics	17
4.1.2	Properties of the Available Process Variables	18
4.1.3	Filtering the RF power Signals	21
4.2	Output: Controllable RF Attenuator	21
4.2.1	Defining Requirements	21
4.2.2	Evaluation of the ZX73-2500-S+ Controllable RF Attenuator	22
4.2.2.1	Common Measurement Setup	25
4.2.2.2	Relation between Control Voltage and Attenuation	26
4.2.2.3	Influence of Supply Voltage Noise on Attenuation	30
4.2.2.4	Influence of RF Frequency on Attenuation	32
4.2.2.5	Influence of Case Temperature Variations on Attenuation	33
4.2.2.6	$V_{control}$ Frequency response	36
4.2.2.7	Combined Maximum Error of the Attenuation and Conclusion	37
4.2.3	Test of the Attenuator with FLUTE	38
5	Controller Design and Evaluation	41
5.1	Plant Identification	41
5.1.1	Principle	41
5.1.2	Identifying the Plant Attenuator+RF	41
5.2	Measurement Filter	45
5.3	Controller Design	50
5.3.1	Choosing a Controller Type	50
5.3.2	Designing a Discrete Time PID Controller	50
5.3.2.1	Controller Tuning	52

5.3.3	Analyzing the Input Tracking and Disturbance Rejection	54
5.3.4	Analyzing the Stability	57
5.3.5	Offline Evaluation with Measured Data	59
5.4	Implementation of the Control System in Software	60
5.5	Evaluation of the Control System (Online)	62
5.6	Further Improvements to the Control System	66
5.6.1	Changing the Controller Architecture: Disturbance Feed-Forward of the Gun Temperature	66
5.6.2	Feed-Back on Faraday-Cup Measurements	67
6	Summary and Outlook	69
Appendix		71
A	Complementary Material Controller Design	71
B	Lab Test and Measurement Equipment	74
Acknowledgments		77

List of Figures

1.1	Schematic of the finished accelerator showing all installed and planned components [5]	3
2.1	General structure of a time continuous feedback control system	9
3.1	Schematic of the <i>Ferninfrarot Linac- und Test-Experiment</i> (FLUTE) Radio Frequency (RF) system	11
3.2	Cross section drawing of the electron gun together with the solenoid (which is used for focusing the electron beam) showing the photo-cathode (red) and the electron and laser beam trajectories (modified version from [21] and [20])	13
3.3	Plot of the electrical field in z direction over the length of the gun cavity (redrawn from [21] using geometrical measurements from [22])	13
3.4	Deviation of the cavity RF power over the course of one hour	15
3.5	Periodogram of Figure 3.4; calculated using the Welch method	15
4.1	Comparing the quantization noise of three process variables	19
4.2	Histogram of the sample time intervals Δ of the plots in Figure 4.1	20
4.3	The ZX73-2500-S+ controllable RF attenuator by Mini-Circuits	23
4.4	Controllable attenuator design around the HP HSMP-3814 RF PIN diodes (redrawn and simplified from [31])	24
4.5	Attenuation vs. frequency over DC control voltage; measured with network analyzer (see B.5.1, parameters: #AVG: 16, IF-BW: 10 kHz); plotted in dashed lines are the measurements from the data sheet (see [30, p. 2])	24
4.6	Measurement setup: DUT(red), RF generator/power splitter/meter(blue), DC sources/meters(green), temperature probe(yellow)	26
4.7	Measured attenuation $A(V_{control}, f = 3 \text{ GHz})$ of the ZX73-2500-S+ as a function of the control voltage input $V_{control}$ along with the sensitivity $S(V_{control}, f = 3 \text{ GHz})$	28
4.8	Zoomed in version of Figure 4.7 shows the attenuation and sensitivity around the operating point $V_{control,o} = 10 \text{ V}$	28
4.9	Long term stability of $V_{control}$ as delivered by the Keysight 34972A DAC (ch. 205); measured with Keysight 34470A; room temperature during measurement: $\mu_\vartheta = 19.12^\circ\text{C}$, $\sigma_\vartheta = 0.28^\circ\text{C}$	29
4.10	Influence of the supply voltage V_+ on the attenuation	31
4.11	Long term stability of V_+ as delivered by the Keysight 34972A DAC (ch. 204); measured with Keysight 34470A; room temperature during measurement: $\mu_\vartheta = 19.12^\circ\text{C}$, $\sigma_\vartheta = 0.28^\circ\text{C}$	31
4.12	Influence of an offset frequency $f - 3 \text{ GHz}$ on the attenuation	33
4.13	Raw measurement result of the influence of the case temperature ϑ_{case} on the attenuation; color coded is the relative elapsed time of the measurement	34
4.14	Influence of the case temperature ϑ_{case} on the attenuation	34
4.15	Comparison between the temperature stability in the “RF lab” and inside the FLUTE Low Level RF (LLRF) cabinet	35

4.16	Spectrum (measured with Holzworth HA7062A (subsubsection B.6.1)) showing the effect of modulating $V_{control}$ with different frequencies (Modulation amplitude: 1 V)	37
4.17	Time signal $V_{control}$ used to calculate Figure 4.19	38
4.18	Time signal $A(V_{control})$ used to calculate Figure 4.19	39
4.19	Measured $A(V_{control})$ with FLUTE; error bars show the span between minimum and maximum values in each $V_{control}$ step	39
5.1	Section of the input sequence (blue) and the system response (orange); Note the inverse relation: A higher attenuation A causes a lower cavity power P_{cavity}	42
5.2	Validation of the estimated process models for the plant; the legend also shows the model fits in percent	43
5.3	Impulse responses of a moving average filter ($N = 100$), a Finite Impulse Response (FIR) lowpass ($N = 50$, $f_c = 0.1$ Hz) and a Infinite Impulse Response (IIR) Butterworth lowpass ($N = 50$, $f_c = 0.1$ Hz)	46
5.4	Effects of the three different lowpass filters in Figure 5.3 on noisy data	47
5.5	Pole-Zero maps for two FIR filters with a common cutoff frequency $f_c = 10$ mHz but different filter orders N ; \circ denotes zeros, \times denotes poles, (k) is a k -times pole	48
5.6	Magnitude response of two FIR filters with a common cutoff frequency $f_c = 10$ mHz but different filter orders N	49
5.7	Block diagram of a generic Proportional Integral Derivative (PID) controller	50
5.8	Required system architecture for the Matlab PID Tuner; PID Tuner input is the system block $Sys[z]$ (green), generated output is the controller $G[z]$ (blue)	53
5.9	Step response of the input tracking F_T for controller $G_1[z]$ and $G_2[z]$, designed with the plant $P[z]$ and a measurement filter of order $N = 10$, response time goal to 5 s and 10 s	55
5.10	Step response of the input tracking F_T for controller $G_3[z]$ and $G_4[z]$, designed with the plant $P[z]$ and a measurement filter of order $N = 40$, response time goal to 5 s and 10 s	55
5.11	Step response of the disturbance rejection F_{DR} for controller $G_1[z]$ and $G_2[z]$, designed with the plant $P[z]$ and a measurement filter of order $N = 10$, response time goal to 5 s and 10 s	56
5.12	Step response of the disturbance rejection F_{DR} for controller $G_3[z]$ and $G_4[z]$, designed with the plant $P[z]$ and a measurement filter of order $N = 40$, response time goal to 5 s and 10 s	56
5.13	Nyquist plot to analyze the stability of the closed-loop control system based on the locus plot of the open-loop system; Note the critical point $(-1, 0j)$ is always on “left” of the curve indicating stability	58
5.14	Two signs of an unstable closed loop system, in this case caused by a measurement filter with too high order and/or a too aggressive controller	58
5.15	Output of the Simulink model in Figure A.3; step size $T = 0.2$ s, end time 3600 s. Simulation time on a computer equipped with an Intel i7-3770: 3.5 s	60
5.16	Cavity power over about 15 h (about three hours of downtime removed for clarity around the 7 h mark); control system switched off at 6 h (recording started 2021/05/01 20:00)	63
5.17	Spectrogram of the cavity power in Figure 5.16	63
5.18	Time plots comparing between the control system on and off	64
5.19	Power spectrum of the plots in Figure 5.16 computed with Welch’s method; shaded areas show the uncertainty according to Equation 2.31	64
5.20	Relative standard deviation $STD\%(t, T)$	65

5.21	Relative standard deviation $STD\%(T)$, shaded areas show $\min\{STD\%(t, T_0)\}$ and $\max\{STD\%(t, T_0)\}$, solid lines show $\text{mean}\{STD\%(t, T_0)\}$ for a fixed window size $T = T_0$	65
5.22	Schematic for a control system that uses disturbance feed-forward of the measurable disturbance $d(t)$ in addition to the feed-back loop; changes to the classical control system architecture in Figure 2.1 highlighted in yellow(changed) and green(added) (based on [14, p. 221])	67
5.23	Cavity power without control interaction, with the controller acting on the cavity power and with the controller acting on charge; Note the three curves are measured at different times and have no relation to one another	68
5.24	Electron charge without control interaction, with the controller acting on the cavity power and with the controller acting on charge; Note the three curves are measured at different times and have no relation to one another	68
A.1	Screenshot of the Matlab System Identification Toolbox; to the right the process models estimator window	71
A.2	Screenshot of the Matlab PID Tuner from the Control Systems Toolbox	71
A.3	Simulink model to evaluate the designed controller together with the measurement filter (σ_{11}) compared to the uncontrolled system (in P2ZU) using measured disturbance data (in the vector $d2$); below a view of the scope data	72
A.4	Screenshot of the control system's GUI application	73

List of Tables

4.1	Comparing quantization steps	18
4.2	Requirements for the controllable RF attenuator	22
4.3	Controllable RF attenuator evaluation test results	38
5.1	Process models of the plant as estimated by the Matlab System Identification Toolboxes process model estimator	43
5.2	Parameters of a discrete time PID controller in parallel form calculated with the Matlab PID Tuner; N is the order of the used measurement filter	54
5.3	Quantitative assessment of the controllers performance	62
B.1	Agilent 34411A specifications	74
B.2	Agilent 34411A some SCPI commands	74
B.3	Keysight 34470A specifications	74
B.4	Keysight 34470A some SCPI commands	74
B.5	Keysight 34972A specifications	74
B.6	Keysight 34972A some SCPI commands	75
B.7	Rohde and Schwarz SMC100A specifications	75
B.8	Rohde and Schwarz SMC100A some SCPI commands	75
B.9	HP E4419B specifications	75
B.10	HP E4419B some SCPI commands	75
B.11	Agilent E5071C specifications	76

Acronyms

- ASCII** American Standard Code for Information Interchange. 25

BIBO Bounded Input Bounded Output. 9

CA Channel Access. 17

CER Coherent Edge Radiation. 3

CERN Conseil Européen pour la Recherche Nucléaire. 12

CSR Coherent Synchrotron Radiation. 3

CSS Control System Studio. 17, 62

cSTART compact Storage ring for Accelerator Research and Technology. 1, 3

DAC Digital-to-Analog Converter. 27

DFT Discrete Fourier Transform. 6, 18

EPICS Experimental Physics and Industrial Control System. 14, 17, 21, 60, 67

ESD Energy Spectral Density. 6

FIR Finite Impulse Response. viii, 45–49

FLUTE Ferninfrarot Linac- und Test-Experiment. vii, viii, 1, 3, 5, 11, 12, 41–43, 50, 52, 54, 59, 62, 67

FPGA Field-Programmable Gate Array. 21

GPIB General Purpose Interface Bus. 25

GUI Graphical User Interface. 42, 53, 60, 61

IDE Integrated Development Environment. 17

IIR Infinite Impulse Response. viii, 46, 47

KARA Karlsruhe Research Accelerator. 25

KIT Karlsruhe Institute of Technology. 1

LINAC Linear Accelerator. 3, 67

LLRF Low Level RF. vii, 21, 33, 35, 38, 62

LTI Linear Time Invariant. 9, 18, 41, 50, 67

LXI LAN eXtensions for Instrumentation. 25

PID Proportional Integral Derivative. viii, ix, 50–54, 60, 61, 67

PRBS Pseudo Random Binary Sequence. 41, 42

PSD Power Spectral Density. 6, 7

PV Process Variable. 17

RF Radio Frequency. vii, ix, 1, 4, 11, 12, 14, 15, 18, 19, 21, 22, 24–26, 32, 33, 35, 38, 41, 45, 62, 67

SCPI Standard Commands for Programmable Instruments. 25

SNR Signal-to-Noise Ratio. 27

STFT Short Time Fourier Transform. 8

THz terahertz. 1, 3

UV ultraviolet. 3, 4

VXI-11 VME eXtensions for Instrumentation protocol specification 11. 25, 60

WSS Wide Sense Stationary. 6

Abstract

FLUTE, a compact linear accelerator, is currently designed and under commission at Karlsruhe Institute of Technology (KIT). Its main purposes are to serve as a technology platform for accelerator research, the generation of strong and ultra short terahertz (THz) pulses and in the future as an injection device for the **compact Storage ring for Accelerator Research and Technology** (cSTART).

At the current commissioning state, the klystron which powers the microwave cavity in the electron gun and, in later stages, the linear accelerator is fed by a pulse forming network, which is driven by a high voltage source connected to mains power. To ensure stable energies of the emitted electron bunches, several parameters of the cavity, such as temperature, as well as the power supply, such as RF power, have to stay inside tight tolerance bands.

In the past, a predominant source of instability were slow drifts of the RF power due to interference with the 50 Hz of the mains voltage. After dealing with this issue, the cavity RF power stability was improved significantly, which also improves the electron stability. But further improvements to the stability are still desired to make the whole system usable for scientific experiments, such as THz spectroscopy.

In this work, instead of passively optimizing the stability of system components, an active approach is evaluated. By means of a control system, the amplitude of the low power RF input signal of klystron, the effects of noise and/or drifts shall be mitigated.

As part of the development process, first the stability issue is analyzed and metrics for the stability are defined. Then the solution, a control system, is proposed. After that, the necessary building blocks of such a control system are treated in detail. From an evaluation of the sensors and actuators, the controller is designed and its positive effect on the gun stability is verified both by simulation and on the actual FLUTE accelerator. In both cases a considerable improvement is noticeable.

Kurzfassung

1. Introduction

In this thesis methods to improve the stability of the electron gun of the FLUTE accelerator are studied.

FLUTE is a Linear Accelerator (LINAC) based THz photon source currently under commission aiming to be a source of high field THz pulses in the femtosecond range, provide a test facility for accelerator research and an injection device for cSTART (see [1]) in the future. [2]

The design aims for a final electron momentum of 41 MeV/c and bunch charges of 1 pC to 3000 pC with lengths of 1 fs to 300 fs. The bunches are emitted with a repetition frequency of up to 10 Hz. [3]

Figure 1.1 shows the finished accelerator schematically. The accelerator mainly consists of the low energy section, the LINAC and the four-dipole bunch compressor.

Along with several diagnostic devices, the low energy section contains the electron gun that pre-accelerates electrons to 7 MeV/c. The electrons are generated at the cathode inside the gun photo-electrically through stimulation with ultraviolet (UV) radiation (270 nm) generated by a Ti:Sa laser. After that a solenoid is used to focus the electron beam for injection into the LINAC section. The LINAC, a 156-cell traveling wave structure, is then used to accelerate the electrons to 41 MeV/c. With a setup of four dipole magnets, the bunches are compressed longitudinally before the last dipole is used to generate Coherent Synchrotron Radiation (CSR) and Coherent Edge Radiation (CER) for THz experiments. [4]

At the time of writing, the low energy section is fully operational and at the end a Faraday cup is installed to measure the bunch charges.

Scientific experiments, such as THz spectroscopy, rely on a known and stable wavelength of the THz radiation. As the THz radiation is emitted from a metal target by the photo effect after being hit by the electron bunches, the wavelength and the wavelength stability of the THz photons depend on the energy and the energy stability of the electrons. Also as FLUTE being a test facility, adding and changing out components, possibly developed by other research institutes, is a common routine. To ensure compatibility among these components, reliable beam parameters at the interfaces between them are necessary. These

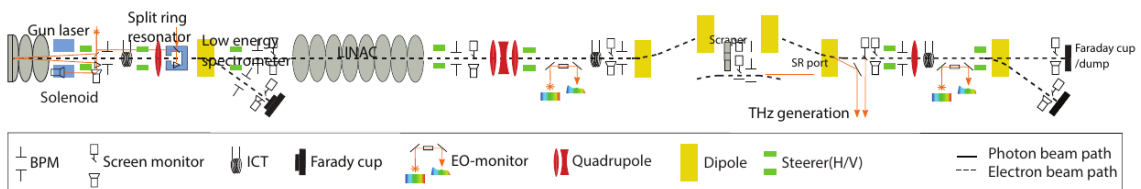


Figure 1.1: Schematic of the finished accelerator showing all installed and planned components [5]

parameters include the beams position in the x - and y -direction, the beam steering angle, the electron energy, the emittance and the charge of the bunch and its dimensions. Since focusing and steering of the beam is done with electromagnets, it is also effected by the electron energy, as the deflection of an electron in a magnetic field is a function of its velocity, so ultimately its energy.

Besides depending on the UV pulses hitting the cathode, there is also a strong dependence of the electron energies on the geometrical, electrical and thermal characteristics of the electron gun and its RF power supply. These characteristics are not independent of each other and changes to them can have a multitude of intrinsic or extrinsic causes.

To improve the stability of the electron energy, in this thesis these causes are analyzed and measures against them or their effects are developed.

2. Theoretical Framework

2.1 Relativistic Electrons

In a (linear) particle accelerator, charged particles, such as electrons, are accelerated to increase their total energy over their energy at rest.

Compared to heavier particles, such as protons ($m_p = 938.27 \text{ MeV}/c^2$), electrons are light particles ($m_p = 0.511 \text{ MeV}/c^2$). They are typically accelerated to speeds comparable to the speed of light to achieve kinetic energies usable for scientific experiments. For this reason, relativistic mechanics are needed to describe their movements.¹ [6]

With the speed of light $c = 2.998 \times 10^8 \text{ m s}^{-1}$ and the particle velocity v , it is common to define [7]:

$$(\text{normalized velocity}) \quad \beta = \frac{v}{c} \quad (2.1)$$

$$(\text{relativistic mass factor}) \quad \gamma = \frac{1}{\sqrt{1 - \beta^2}} \quad (2.2)$$

$$(\text{relativistic momentum}) \quad p = \gamma mv \quad (2.3)$$

The total energy of a particle is [6]

$$E = \sqrt{(mc^2)^2 + (pc)^2}, \quad \text{with the rest energy } mc^2 \quad (2.4)$$

and the kinetic energy is

$$T = E - mc^2. \quad (2.5)$$

With electrons leaving the FLUTE electron gun with a momentum of $p = 7 \text{ MeV}/c$, this is equivalent to

$$E = \sqrt{(m_e c^2)^2 + (pc)^2} = 7.018\,627\,188\,6 \text{ MeV} \quad (2.6)$$

$$\gamma = \frac{E}{m_e c^2} = 13.735\,11 \quad (2.7)$$

$$\beta = \sqrt{1 - \gamma^{-2}} = 0.9973 \quad (2.8)$$

2.2 Signal Analysis

2.2.1 Auto Correlation and Cross Correlation

The *cross covariance* between two stochastic processes $x[n]$ and $y[n]$ is a measure of the similarity between $x[n]$ at index n_1 and $y[n]$ at index n_2 and is defined as

$$r_{xy}[n_1, n_2] = E \{ (x[n_1] - \mu_x[n_1])(y[n_2] - \mu_y[n_2])^* \}. \quad (2.9)$$

¹As relativistic mechanics are a super set of classical mechanics, the equations also apply for slower particles.

For the special case of $y[n] := x[n]$, $r_{xx}[n_1, n_2]$ is called *auto covariance* and is a measure of self similarity of $x[n]$ [8, p. 172].

The processes $x[n]$ and $y[n]$ are called *Wide Sense Stationary (WSS)* if the following two properties hold [8, p. 167]. First, their means $\mu_\xi[n]$ are constant, i.e. they do not depend on the sample index:

$$\mu_x[n] = \mu_x \quad (2.10)$$

$$\mu_y[n] = \mu_y \quad (2.11)$$

Also the auto covariance does not depend on the absolute sample indices n_1 and n_2 , but merely on the difference between them:

$$r_{xy}[n_1, n_2] = r_{xy}[m], \quad \text{with: } m := n_2 - n_1 \quad (2.12)$$

If both process in Equation 2.9 are WSS, Equation 2.9 simplifies to

$$r_{xy}[m] = E \{ (x[n] - \mu_x)(y[n - m] - \mu_y)^* \}. \quad (2.13)$$

For the auto covariance both means are identical and can be moved outside the expectation operator:

$$r_{xx}[m] = E \{ (x[n])(y[n - m])^* \} - \mu_x^2. \quad (2.14)$$

When analyzing signals, the stochastic processes are often unknown and only one realization $x[n]$ is known. But if the process generating $x[n]$ is (*weakly*) *ergodic*, then one realization is enough to determine the auto covariance of the process [9, p. 252]. Then the auto covariance can be estimated with

$$\hat{r}[m] = \frac{1}{N} \sum_{n=m+1}^N x[n] x^*[n - m] \quad m \in [0, N - 1] \quad (2.15)$$

2.2.2 Estimating the Spectrum of a Stochastic Process

For a deterministic, time-discrete signal $x[n] \in \mathcal{L}_1$, the Discrete Fourier Transform (DFT) exists[10] and is defined as

$$X[k] = \sum_{n=0}^{N-1} x[n] e^{-j \frac{2\pi}{N} k n} \quad k, n \in [0, N - 1], \quad (2.16)$$

using $k = \frac{N}{2\pi} \omega = N f$ as the independent, discrete frequency variable. From the complex sequence $X[k]$, often only the magnitude (or energy) is of greater interest while the phase information are neglected. Therefore, S_{xx} is defined as

$$S_{xx} = |X[k]|^2 \quad (2.17)$$

and called the *Energy Spectral Density (ESD)*.

If $x[n]$ is the realization of a stochastic process, then it is of random nature rather than deterministic. Because realizations of physical processes do not posses finite energy, they are not in the \mathcal{L}_1 set and their DFT is not defined [11, p. 5].

In this case instead of an energy spectral density, the spectrum of the average power of the process, called the *Power Spectral Density (PSD)*, can be used instead. To compute the PSD, there are two possibilities:

$$\Phi_{xx}[k] = \sum_{m=-\infty}^{\infty} r[m] e^{-j \frac{2\pi}{N} k m} \quad (2.18)$$

$$\Phi_{xx}[k] = \lim_{N \rightarrow \infty} E \left\{ \frac{1}{N} \left| \sum_{n=0}^{N-1} x[n] e^{-j \frac{2\pi}{N} k n} \right|^2 \right\} \quad (2.19)$$

When assuming $r[m]$ decays “fast enough”, i.e.

$$\lim_{N \rightarrow \infty} \frac{1}{N} \sum_{m=-N}^N |m| |r[m]| = 0 \quad (2.20)$$

then Equation 2.18 and Equation 2.19 are equal[11, p. 7].

For measured data however neither equations can be used directly. For Equation 2.18 the auto covariance sequence $r[m]$ is unknown. But it could be estimated with Equation 2.15. In case of Equation 2.19 it is not possible to evaluate the limit, because only finite length data can be sampled and also the expectation can not be computed since in general there is only one realization available. Both operations can be neglected when doing an estimation.

With these practical changes in place, Equation 2.18 and Equation 2.19 become

$$\hat{\Phi}_{c,xx}[k] = \sum_{m=-(N-1)}^{N-1} \hat{r}[m] e^{-j\frac{2\pi}{N}km} \quad (\text{Correlogram}) \quad (2.21)$$

$$\hat{\Phi}_{p,xx}[k] = \frac{1}{N} \left| \sum_{n=0}^{N-1} x[n] e^{-j\frac{2\pi}{N}kn} \right|^2 \quad (\text{Periodogram}). \quad (2.22)$$

Both methods yield equal results, if $r[m]$ is estimated with the biased estimator $\hat{r}[m]$ in Equation 2.15 in contrast to the unbiased estimator (compare [11, p. 24])

$$\hat{r}_{\text{unbiased}}[m] = \frac{1}{N-m} \sum_{n=m+1}^N x[n] x^*[n-m] \quad m \in [0, N-1]. \quad (2.23)$$

[12] shows one key weakness of the unmodified periodogram method in Equation 2.22: The variance does not decrease significantly with more samples N . Instead the variance of the periodogram for each frequency approaches the square of the actual PSD:

$$\lim_{N \rightarrow \infty} \text{Var} \left\{ \hat{\Phi}_{p,xx}[k] \right\} = \Phi_{xx}^2[k] \quad (2.24)$$

Furthermore the periodogram/correlogram suffer from the smearing and leakage effects because the limited length of the data samples always causes an implicit windowing, thus reducing frequency resolution.

There are several popular methods that improve on the periodogram/correlogram concepts:

Blackman-Tukey: Because of the poor accuracy of $\hat{r}[m]$ for $k \approx N$ in the definition of $\hat{\Phi}_{c,xx}[k]$ and the bigger the N , the more small errors in $\hat{r}[m]$ sum up, truncating/windowing of $\hat{r}[m]$ with $w[k]$ (length M) can be beneficial for the accuracy of the estimation.

$$\hat{\Phi}_{BT,xx}[k] = \sum_{m=-(M-1)}^{M-1} w[k] \hat{r}[m] e^{-j\frac{2\pi}{N}km} \quad (2.25)$$

The choice of the window $w[k]$ trades frequency resolution for variance and smearing for leakage reduction [11, p. 41].

Barlett: The Barlett method reduces the variance of the periodogram by splitting the N data samples in $Q = N/M$ blocks and averaging together the sub-periodograms:

$$\hat{\Phi}_{q,xx}[k] = \frac{1}{M} \left| \sum_{n=0}^{M-1} x_q[n] e^{-j\frac{2\pi}{M}kn} \right|^2 \quad (2.26)$$

$$\hat{\Phi}_{B,xx}[k] = \frac{1}{Q} \sum_{q=1}^Q \hat{\Phi}_{q,xx}[k] \quad (2.27)$$

The variance of the estimation scales with Q [12, p. 6]:

$$\text{Var} \left\{ \hat{\Phi}_{B,xx}[k] \right\} = \frac{1}{Q} \Phi_{xx}^2[k] \quad (2.28)$$

Welch: The Welch method combines splitting the data into Q segments with windowing each segment and allowing the segments to overlap. With $P = 1/M \sum_{n=0}^{M-1} |w[n]|^2$ being the “power” of the window, the Welch method is computed as

$$\hat{\Phi}_{s,xx}[k] = \frac{1}{MP} \left| \sum_{n=0}^{M-1} x_s[n] e^{-j \frac{2\pi}{M} k n} \right|^2 \quad (2.29)$$

$$\hat{\Phi}_{W,xx}[k] = \frac{1}{Q} \sum_{s=1}^Q \hat{\Phi}_{s,xx}[k]. \quad (2.30)$$

Compared to the Barlett method, the overlapping of up to 50% (see [13]) allows increasing Q , thus reducing the variance.

$$\text{Var} \left\{ \hat{\Phi}_{W,xx}[k] \right\} = \frac{1}{Q} \Phi_{xx}^2[k] \quad (2.31)$$

In case of a non-stationary signal $x[n]$, one possibility to analyze and display the spectral content is the use of the Short Time Fourier Transform (STFT) and the spectrogram, which is a two dimensional power spectral density function mapping frequency and time to a third coordinate like height, intensity or color.

To calculate the spectrogram, the signal is split into segments with the sliding window $w[n-m]$ for which duration the signal is assumed to be stationary. For each segment at time index m , the periodogram is calculated according to

$$\hat{\Phi}_{xx}[k,m] = \frac{1}{N} \left| \sum_{n=0}^{N-1} w[n-m] x[n] e^{-j \frac{2\pi}{N} k n} \right|^2. \quad (2.32)$$

2.3 Feedback Control Systems

Feedback control systems are used to control a dynamic system (plant) in such a way that its output $y(t)$ follows a certain input $x(t)$ and disturbances on the output $d(t)$ are rejected. The general structure of a closed loop control system is shown in Figure 2.1. To achieve the tracking of the input and the stabilization of the output, a controller $G(s)$ uses the error $e(t)$ to control the plant $P(s)$ accordingly. The error is defined as

$$e(t) = x(t) - r(t) = x(t) - [y(t) * h(t)] \quad (2.33)$$

with $h(t)$ being the inverse Laplace transform of the filters transfer function $H(s)$.

Feedback control systems, or closed-loop systems, are to be differentiated from open-loop systems, in which there is no return path, so they cannot compensate for *unknown* disturbances. If $d(t)$ is known $\forall t$, then an open loop system would be possible and any errors could simply be compensated.

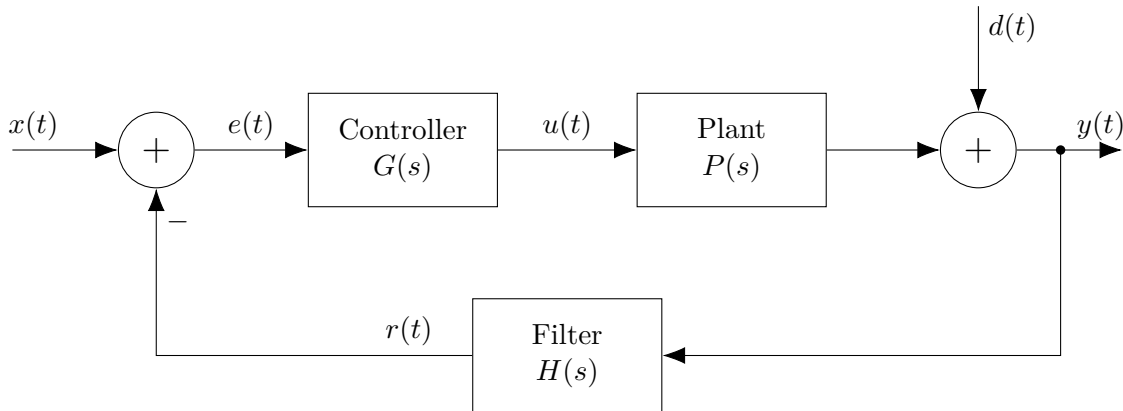


Figure 2.1: General structure of a time continuous feedback control system

2.3.1 Disturbance Rejection and Input Tracking

Disturbance rejection and input tracking are two important characteristics to evaluate a stable controller. To calculate them, the block diagram in Figure 2.1 and the Laplace transform of the inputs/outputs is used.²

To calculate how the output $y(t)$ depends on the input $x(t)$, the input tracking transfer function can be used.[14, p. 88] It is calculated as the transfer function $F_T = Y(s)/X(s)$ by setting $d(t) = 0$:

$$Y(s) = G(s)P(s)E(s) \quad \text{with: } E(s) = X(s) - H(s)Y(s) \quad (2.34)$$

$$\Leftrightarrow Y(s)[1 + G(s)P(s)H(s)] = G(s)P(s)X(s) \quad (2.35)$$

$$\Leftrightarrow F_T := \frac{Y(s)}{X(s)} = \frac{G(s)P(s)}{1 + G(s)P(s)H(s)}. \quad (2.36)$$

On the other hand, the transfer function $F_{DR} = Y(s)/D(s)$ can be used to describe the systems response to a disturbance.[14, p. 88] It is defined by letting $x(t) = 0$ and calculating

$$Y(s) = G(s)P(s)E(s) + D(s) \quad \text{with: } E(s) = -H(s)Y(s) \quad (2.37)$$

$$\Leftrightarrow Y(s)[1 + G(s)P(s)H(s)] = D(s) \quad (2.38)$$

$$\Leftrightarrow F_{DR} := \frac{Y(s)}{D(s)} = \frac{1}{1 + G(s)P(s)H(s)}. \quad (2.39)$$

2.3.2 Stability

The application of a controller to a system is only useful if the resulting system has a stable behavior. One possible definition of stability is the Bounded Input Bounded Output (BIBO) criterion[14, p. 82]:

Definition 1. (*BIBO stability*) A Linear Time Invariant (LTI) system is said to be BIBO stable if for some $M, N \in \mathbb{R}^+$, the response to a bounded input $|u(t)| \leq M$ results in a bounded output $|y(t)| \leq N$.

For a given control system, one way to analyze its stability is to plot the locus $z = F_o(s = j2\pi f)$ of the open loop frequency response

$$F_o(s) = G(s)P(s)H(s) \quad (2.40)$$

from $f = 0$ to $f = \infty$ and using the Nyquist stability criterion. For the special case of a stable open loop $F_o(s)$ ³ the Nyquist stability criterion can be stated as[14, p. 111]

²The Laplace transform of a function in time $f(t)$ is written as $F(s) = \mathcal{L}\{f(t)\}$.

³The stability of $F_o(s)$ can often easily be determined from the block diagram.

Definition 2. (*Nyquist stability criterion*) If the open loop $F_o(s)$ is stable, then the closed loop is stable if $z = F_o(s = j2\pi f)$ does not go through or encircles $z = -1$.

2.4 Metrics to Quantify the Stability of a Signal

“Stability” can have different meanings depending on the context. In case of signal processing, a signal is usually said to be *stable* if it has only little variation around its mean or some target value, i.e. the mean has to be constant and the variance stays below some threshold. Stability is not to be confused with stationarity, which requires the mean and the variance and the autocorrelation stay constant over time [15]. To express stability as a single numerical value, there are several possibilities, some are described in the following.

Relative Standard Deviation

This measures the stability as the standard deviation but related to the mean value to make it comparable to other quantities with different scaling or units.

The relative, or percentual, standard deviation of the stationary stochastic process X is defined using the mean μ_X and the standard deviation σ_X as

$$\%STD_X := \frac{\sigma_X}{\mu_X}. \quad (2.41)$$

If the process X is non stationary, $\%STD_X$ depends on the absolute time t and the window size T for which the process is assumed to be stationary:

$$\%STD_X = \%STD_X(t, T) \quad (2.42)$$

In that case, for a fixed window size $T = T_0$, a mean percentual standard deviation can be computed with (assuming discrete time steps t_n , $n \in [0, N - 1]$)

$$\%STD_X(T = T_0) = \frac{1}{N} \sum_{n=0}^{N-1} \%STD_X(t_n, T_0) \quad (2.43)$$

Mean Squared Error

The mean squared error sums up the squared errors $(x[n] - x_t[n])^2$ of $x[n]$ from a set value $x_t[n]$. To remove the effect of the length of the data sequence, the sum is divided by the length of the sequence N :

$$MSE_x := \frac{1}{N} \sum_{n=0}^{N-1} (x[n] - x_t[n])^2 \quad (2.44)$$

Relative Power of Most Prominent Noise

This novel approach compares the power of the most prominent noise power source $P_{noise, max}$ of the signal x with the total power P_x :

$$MPN_x := \frac{P_{noise, max}}{P_x} \quad (2.45)$$

3. The Stability of FLUTE the Electron Gun and Proposed Stabilizing Solution

This chapter deals with the electron gun of FLUTE and its power supply. Then based on fundamental equations of electron gun's microwave cavity, the dependence of the electron energy from the RF supply is derived, which motivates why the RF supply should be stable. Then a solution to stabilize the RF is proposed.

The electron gun is powered by a 50 MW klystron, a high-power vacuum tube RF amplifier. The input signal for the klystron is a 2.998 55 GHz harmonic oscillator pre-amplified to 200 W. The supply input is generated by a pulse forming network and a transformer. The pulse forming network mainly consists of capacitors to store electrical energy and is charged with a constant current source. The connection of these devices is shown in Figure 3.1.

A 5 Hz master clock (“trigger”) is used to switch on the output of the pulse forming network to the klystron and the oscillator every 0.2 s for 4.5 μ s. During this time, the laser could also be triggered causing a stimulated emission of an electron bunch from the cathode. But even without the laser being active, powering the electron gun with the klystron generates an electron beam through thermionic emission of electrons. This undesired effect is called *dark current*.

The current source to charge the pulse forming network is powered by mains voltage. This makes it susceptible to noise on the mains and also caused slowly time varying drifts of the klystron power due the pulse forming network being triggered at different relations to the mains 50 Hz. This issue has been remedied in [16] by adding synchronization to the mains phase.

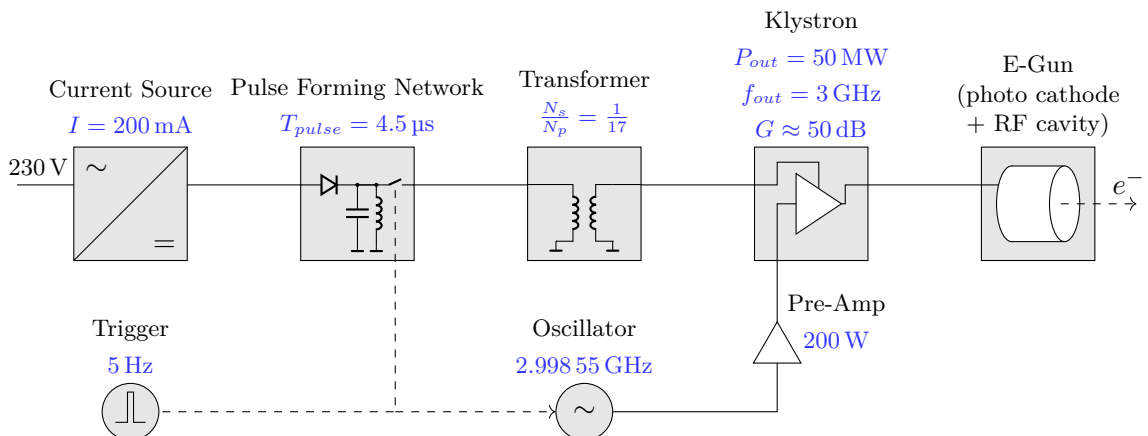


Figure 3.1: Schematic of the FLUTE RF system

3.1 The Electron Gun

The electron gun of FLUTE was originally designed and operated in CTF II at Conseil Européen pour la Recherche Nucléaire (CERN). [17] It is of the “BNL type” (see [18], based on the original design by [19]) and was developed at CERN. [20]

The gun is made up of a 2.5 cell microwave cavity with a removable copper cathode embedded in the cone shaped back at the end of the half cell (see Figure 3.2). Cooling is achieved with a two-stage water cooling system: A temperature control unit uses a short water circuit to cool the gun while itself uses a heat exchanger to a bigger outside climate unit.

Applying RF power to the cavity through the hole-coupled wave guide causes a standing wave inside the cavity. Because of the cavity’s dimensions, only the fundamental mode TM_{010} is excited, for which the relation between resonance frequency f_{010} and radius a of the cavity is given by

$$\frac{f_{010}}{2\pi} = \frac{2.405 \cdot c}{a}. \quad (3.1)$$

For the TM_{010} mode there is only an electrical field in the z direction, i.e. along the beam axis. This $E_z(z)$ field is used to accelerate the electrons. For the FLUTE gun, $E_z(z)$ has been measured in [21], see Figure 3.3. These measurements are also verified in [17].

To tune the resonance frequency f_{010} , which depends on the cavity’s radius a , to the target design frequency of 2.998 55 GHz, two methods are used. For once the cavity is equipped with piston tuners that allow changing the geometries of each cell slightly. Additionally because of the expansion and contraction of the copper body due to temperature changes, the set-point of the water cooling system can also be changed to alter the cavity geometry.

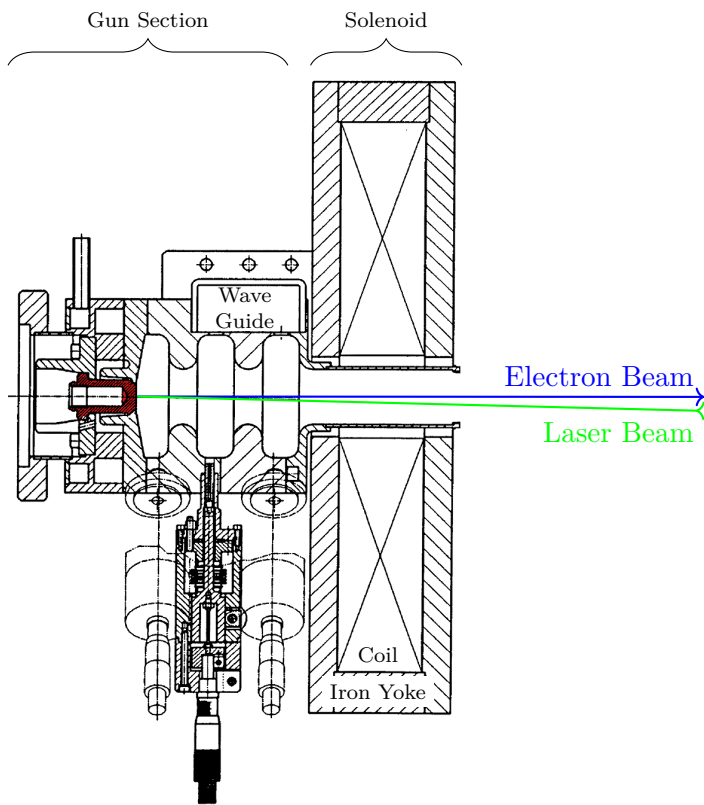


Figure 3.2: Cross section drawing of the electron gun together with the solenoid (which is used for focusing the electron beam) showing the photo-cathode (red) and the electron and laser beam trajectories (modified version from [21] and [20])

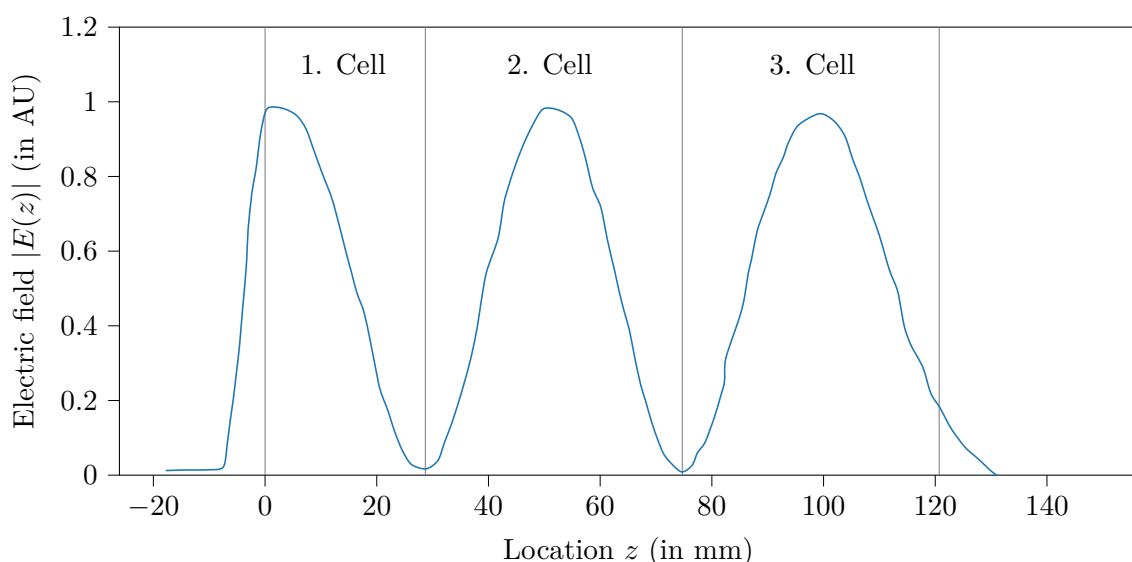


Figure 3.3: Plot of the electrical field in z direction over the length of the gun cavity (redrawn from [21] using geometrical measurements from [22])

3.2 Relation between RF power and Electron Energy

A standing wave inside a RF cavity for a TM_{010} mode can be written as

$$E_z(z, t) = E(z) \cos(\omega t + \phi). \quad (3.2)$$

The time t has to be expressed in terms of the electron velocity $v(z)$ as

$$t = t(z) = \int_0^z \frac{dz}{v(z)}, \quad (3.3)$$

which is the arrival time of the electron at location z .

If moving through an accelerating gap of length L inside a cavity, an electron with charge q gains the energy

$$\Delta W = q \int_{-L/2}^{L/2} E(z) \cos(\omega t(z) + \phi) dz \quad (3.4)$$

This can be rewritten as

$$\Delta W = q V_0 T \cos(\phi) \quad (3.5)$$

using the axial RF voltage

$$V_0 := \int_{-L/2}^{L/2} E(z) dz \quad (3.6)$$

and the travel time factor T . [7, p. 32]

With the *shunt impedance* R_s , the axial RF voltage can be brought into relation with the RF power, that need to be induced into the cavity to compensate losses in the non-perfect conducting walls and power lost to the electron beam. [23]

The shunt impedance is defined as

$$R_s = \frac{V_0^2}{P_{RF}} \quad (3.7)$$

Equation 3.5 and Equation 3.7 show that the RF supply has a great impact on the electron energy, so it needs to be stable.

Additionally, there is the so called *R over Q*, defined as

$$\frac{R}{Q} = \frac{(V_0 T)^2}{\omega U} \quad \text{with: } R = R_s T^2 \text{ (effective shunt impedance)} \quad (3.8)$$

using the total stored electromagnetic energy U and the quality factor $Q = \omega U / P_{RF}$.

This shows the gained energy also depends on the properties of the cavity.

3.3 Current RF Stability and Proposed Solution

To get an overview of the current stability of the RF power, the deviation of the cavity power process value (Experimental Physics and Industrial Control System (EPICS): F:RF:LLRF:01:GunCav1:Power:Out Value) from its mean is plotted over one hour, see Figure 3.4.

With the metrics defined in section 2.4, the STD % is 0.15 % and the MSE is 38.54.

From the time plot in Figure 3.4 and the periodogram in Figure 3.5 it becomes clear that there is random white noise, but also a periodic part and a slow drift in the signal. While it is not possible to counteract the random fluctuations by any practical means, it is however possible to compensate for the slower disturbances.

Hence in the next chapters, a **control system** is developed to counteract these noise components.

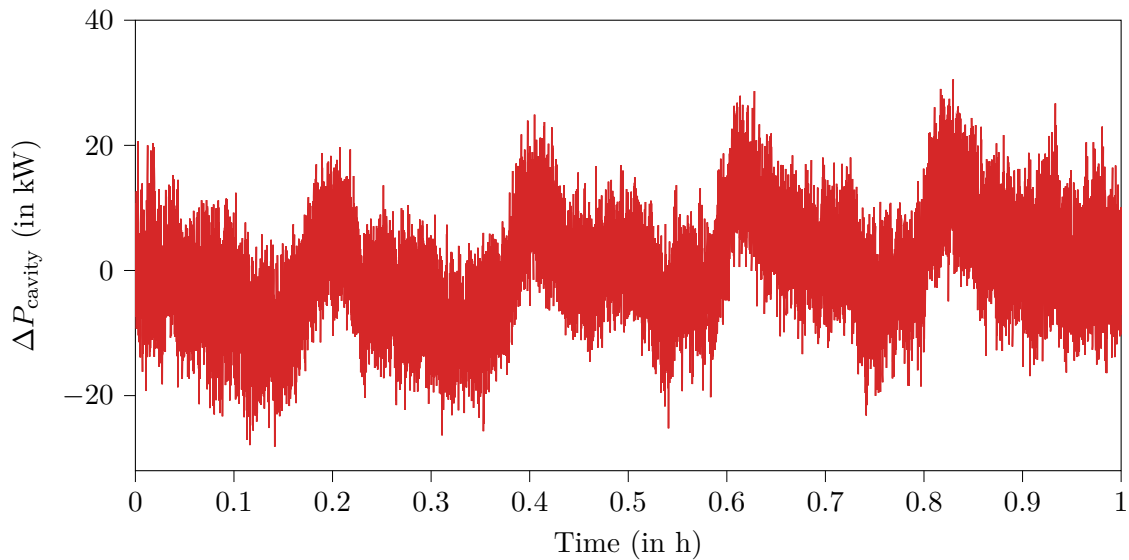


Figure 3.4: Deviation of the cavity RF power over the course of one hour

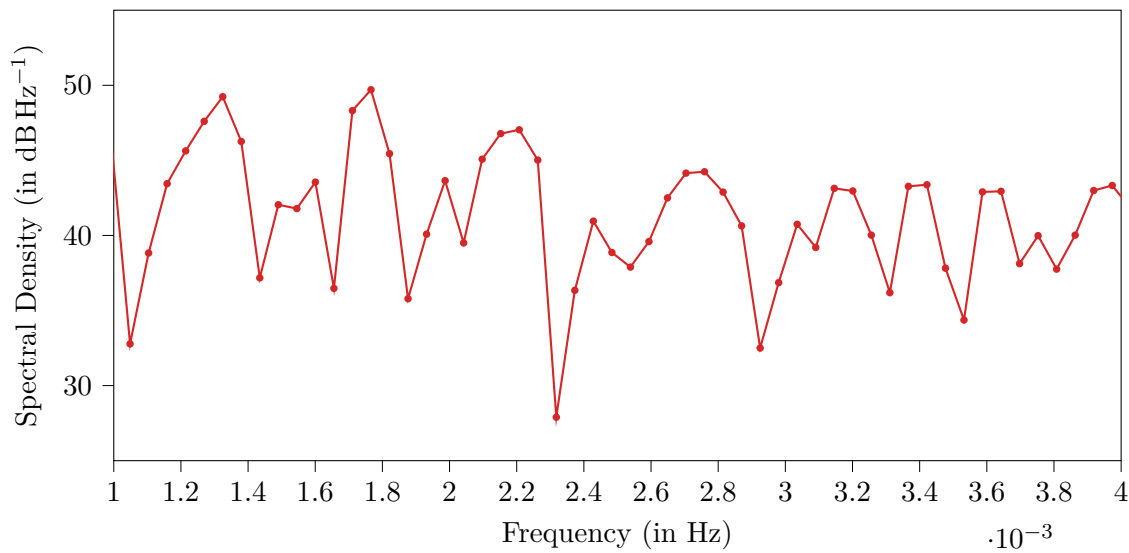


Figure 3.5: Periodogram of Figure 3.4; calculated using the Welch method

4. Interfacing FLUTE

This chapter covers methods on interfacing the FLUTE accelerator, that is how to read diagnostic measurements into the control system from FLUTE and how to influence the electron acceleration appropriately to achieve stabilization.

In this chapter *input* and *output* refer to the view from the control system.

4.1 Inputs

FLUTE uses the *EPICS*[24] for control of various parts of the accelerator, to send real time data to be archived and to build user interfaces via *Control System Studio (CSS)*[25], a development studio based on the Java Integrated Development Environment (IDE) Eclipse. [26]

EPICS offers client/server and publish/subscribe paradigms to access data in so called Process Variable (PV) through channels. Modules are usually written in the C programming language. To ease the access to EPICS channels in programs written with the Python language, the package *PyEpics*[27] can be used. Since all data of interest as input for the control system can be extracted through an EPICS channel, the next section deals with using PyEpics to obtain the data.

4.1.1 Accessing EPICS channels in Python with PyEpics

Before usage PyEpics needs to be installed, e.g. with `pip3 install pyepics` from the *PyPi* repository. If the computer running the Python code can reach the EPICS Channel Access (CA) repeater on the machine network, the connection is established automatically in the background. To get a channel value asynchronously, i.e. at an arbitrary time, the function `caget(pvname)` can be used with the name of the desired process value, see Listing 4.1.

Listing 4.1: Using `caget()` to get the value of an EPICS process value

```
1 from epics import caget
2 print(f"Cavity RF power: {caget('F:RF:LLRF:01:GunCav1:Power:Out')}")
```

Another way is to setup a channel object and create a subscription with an user defined callback function that is executed each time the process variable changes. This implements synchronous access to the PV and can be compared to an interrupt rather than polling the variable as in Listing 4.1.

For a non trivial example see Listing 4.2. In this program, the time differences between new values and their statistics are printed to the console.

Listing 4.2: Using a user defined callback function to access an EPICS process value

```
1 from epics import ca
2 import time
3 import numpy as np
```

```

4
5 dts=np.array([])
6 lastCalled=time.time()
7
8 def call(pvname, value, **kwargs):
9     global lastCalled, dts
10    now=time.time()
11    dt=now-lastCalled
12    lastCalled=now
13    dts=np.append(dts, dt)
14
15 chid=ca.create_channel("F:RF:LLRF:01:GunCav1:Power:Out")
16 - , - , eventID=ca.create_subscription(chid, callback=call, use_time=True)
17
18 while(True):
19     time.sleep(2)
20     print(f"N:{len(dts)},mean:{np.mean(dts)},min:{np.min(dts)},max:{np.max(dts)},std:{np.std(dts)}")
```

4.1.2 Properties of the Available Process Variables

In this section some process variables that may be used as inputs for the control system are analyzed. These are:

- **F:RF:LLRF:01:GunCav1:Power:Out Value:** The RF power measured in the half cell of the gun cavity
- **F:AX:DAQDT:01:1:Wave:05:Sample Value:** The charge measured with a Faraday cup (RadiaBeam Technologies FARC-04 [28]) and amplified with a charge sensitive amplifier (PCB 421A25 [29])
- **F:INJ-1:Gun:01:Temperature:Body Value:** The body temperature of the cavity

In Figure 4.1 all three are plotted for a duration of 15 min without any interference to the system and the system being in steady state operation.

In addition the sample times of the process variables is examined if the method with a custom callback is used (see Listing 4.2) or the data is extracted from the archive. The differences in the sample times are calculated according to

$$\Delta = t_{n+1} - t_n. \quad (4.1)$$

Then a histogram with the relative frequency on the y axis is used as an estimator for the probability density function of the sample time intervals (see Figure 4.2). The histogram shows that the time series resulting from recording process variables out of the EPICS system are highly unevenly spaced. Thus the data needs to be converted to posses evenly spaced sample times to use common signal processing methods like the DFT or digital LTI filters. For offline analysis of prerecorded data, it can easily be resampled to a fixed time grid. But for online operation of a filter or a whole control system it is not possible to use an arbitrary resample method because they are often non causal or introduce significant group delay when made causal. Instead calling `caget()` with a (software-) timer can be used to get evenly spaced samples online.

Table 4.1: Comparing quantization steps

PV	N_{unique}	q_{avg}	q_{norm}
F:RF:LLRF:01:GunCav1:Power:Out Value	84	0.6935	0.011 904
F:AX:DAQDT:01:1:Wave:05:Sample Value	22	0.015	0.045 45
F:INJ-1:Gun:01:Temperature:Body Value	18	0.1294	0.055 55

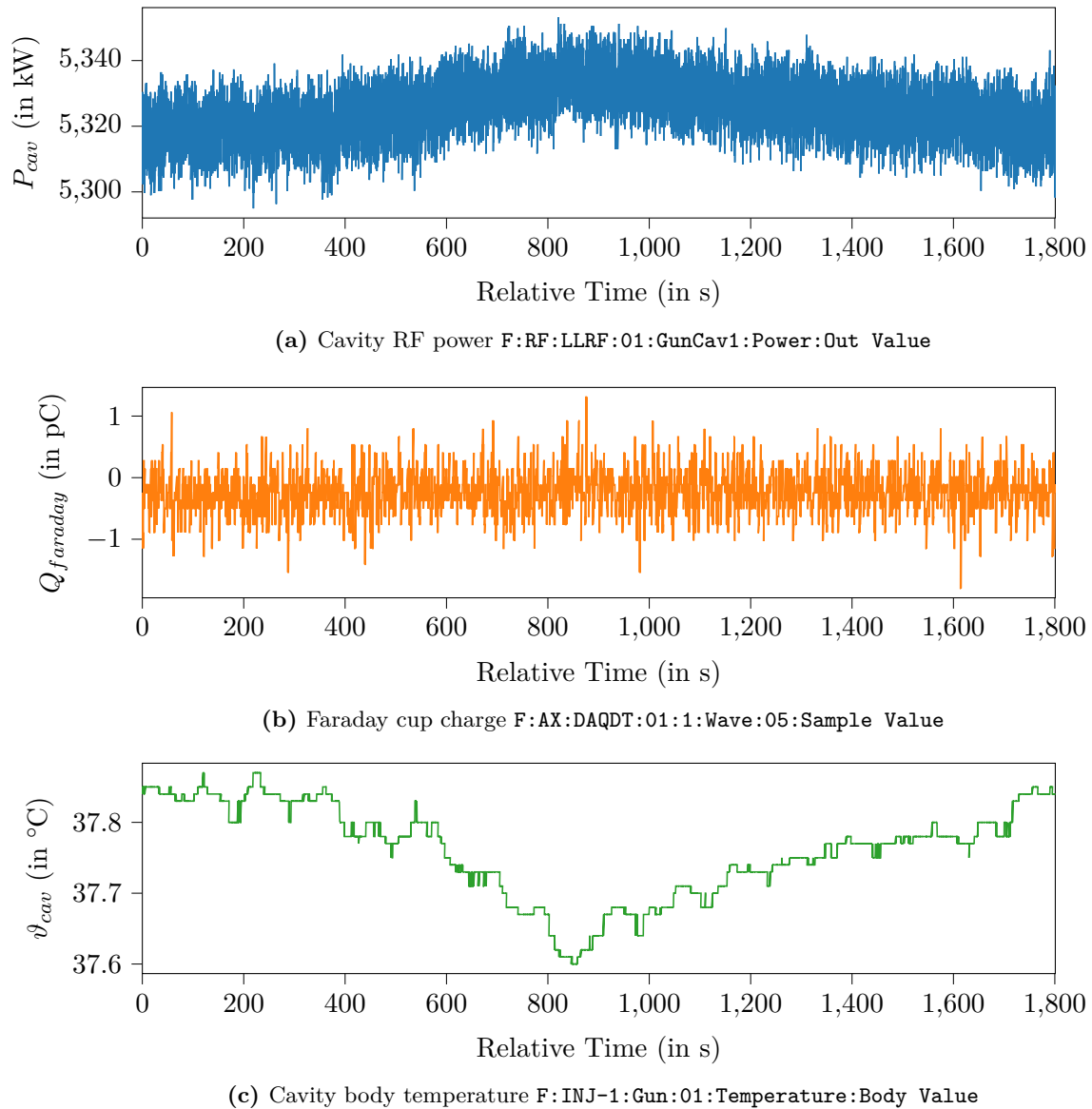


Figure 4.1: Comparing the quantization noise of three process variables

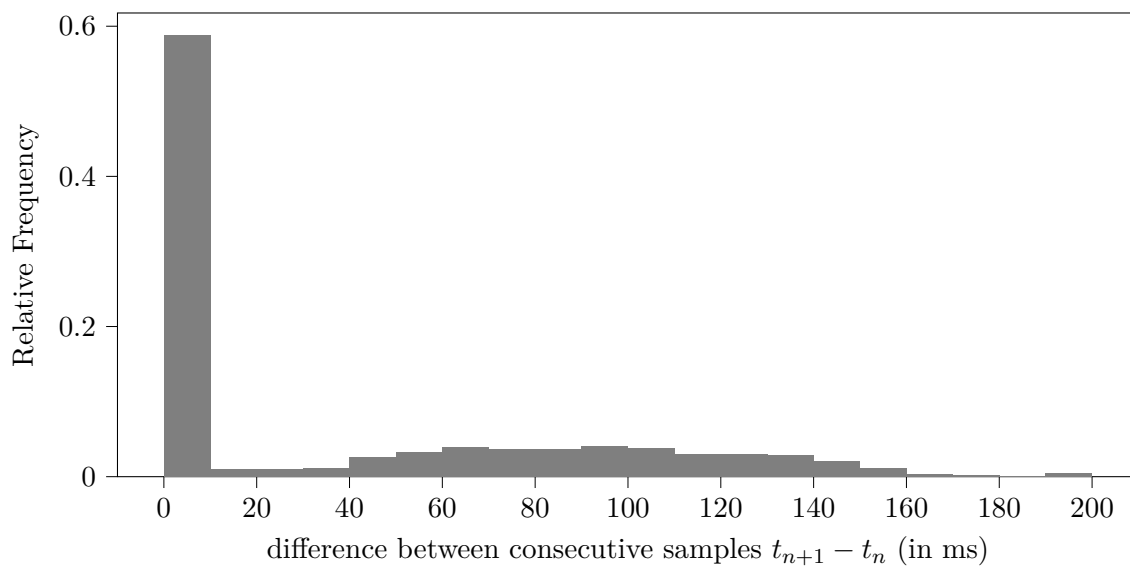


Figure 4.2: Histogram of the sample time intervals Δ of the plots in Figure 4.1

4.1.3 Filtering the RF power Signals

In case of the klystron output RF power or the power at the cavity, filtering of the signal is needed to remove zero outliers. These outliers occur if a high voltage arc occurs inside the cavity. This is detected and the LLRF control system shuts off the RF power for the current pulse (called a “breakdown”). These outliers are not representative of the average RF power inside the cavity over multiple pulses and thus would greatly impair the controller performance. For that reason, before any further filtering to remove noise etc, a breakdown removal filter is used (Listing 4.3). In principle the new power value is checked to be inside a band the size of which is determined by the mean deviation of the N_{filt} previous values and a scaling m . The percentile differences are used here as they are robust against outliers (i.e. other breakdowns) in the N_{filt} previous values opposed to a normal standard deviation. The scaling with $(2 * 1.2815)^{-1}$ is used to make the mean deviation comparable to a standard deviation.

Listing 4.3: Breakdown removal filtering

```

1 if(abs(P[i]-np.median(P[i-3*Nfilt:i-Nfilt])) <
2 m*(np.percentile(P[i-3*Nfilt:i-Nfilt],90)-np.percentile(P[i-3*Nfilt:i-Nfilt],10)/(2*1.2815))):
3     P_filt = np.append(P_filt,P[i])
4 else:
5     breakdown_locations_predicted = np.append(breakdown_locations_predicted,i)
6     P_filt = np.append(P_filt,np.median(P[i-3*Nfilt:i-Nfilt]))

```

4.2 Output: Controllable RF Attenuator

The output signal computed by the control systems has to have a way of influencing the RF power sent to the cavity. This could be done over an EPICS channel (e.g. with the PyEpics function `caput()` to set the value of a process variable via a channel access). However to make it possible to move the control system from a general purpose personal computer to a dedicated digital signal processor, Field-Programmable Gate Array (FPGA) or similar in the future, using a physical device in the signal path is preferred.

4.2.1 Defining Requirements

The controllable attenuator should allow to vary the attenuation in a span big enough to counteract typical instabilities on the FLUTE RF power. The set attenuation should be stable. This is especially needed in cases where the control system is not enabled. Then the attenuator should not add noise or drift to stay “transparent” for other systems. To allow for other attenuator or amplifiers in the signal path to compensate the attenuation around its operating point, the nominal attenuation should be as low as possible. The attenuation resolution should be low enough to allow for fine control and not to add noticeable quantization noise. Also the setup time for a new value should be small enough to not be visible to the control system.

Other factors like the control/supply voltages and the operating temperature range are limited by the available hardware or governed by the mounting location.

All requirements are summarized in Table 4.2.

Table 4.2: Requirements for the controllable RF attenuator

Requirement	Value/Range
attenuation adjustment	$\pm 0.2 \text{ dB}$
attenuation stability	$\pm 0.001 \text{ dB}$
nominal attenuation at operating point	< 10 dB
attenuation resolution	0.001 dB
setup time	10 ms
operating temperature range	$(25.0 \pm 0.1)^\circ\text{C}$
supply voltage	3 V to 12 V
control voltage	3 V to 12 V

4.2.2 Evaluation of the ZX73-2500-S+ Controllable RF Attenuator

The *ZX73-2500-S+* is a voltage controllable RF attenuator with coaxial SMA connectors by the company Mini-Circuits. As there is no alternative model from Mini-Circuits and devices from other manufacturers are offered with similar specifications, only the *ZX73-2500-S+* is evaluated in detail in this section.

The *ZX73-2500-S+* attenuator consists of a brass housing/shielding containing the Mini-Circuits RVA-2500+, a variable SMD attenuator in the DV874 case form factor. The RF input and output are connected with female SMA screw connectors. The power supply and control voltage are connected with solder pins. In order to use shielded cables and a reliable connection, for all measurements SMA connectors are soldered to the supply and control pins. According to equivalent circuit in the data sheet [30], it can be assumed it is based on the common quad- π pin diode design introduced in [31]. In this attenuator design, the resistors in a fixed π -configuration attenuator are switched out for RF PIN diodes with the appropriate biasing and matching resistors and capacitors, see Figure 4.4. At high frequencies, PIN diodes behave like resistors with the differential resistance

$$r_d = f(I_F) \quad (4.2)$$

being an inverse function of the forward bias current, which makes the attenuator adjustable.

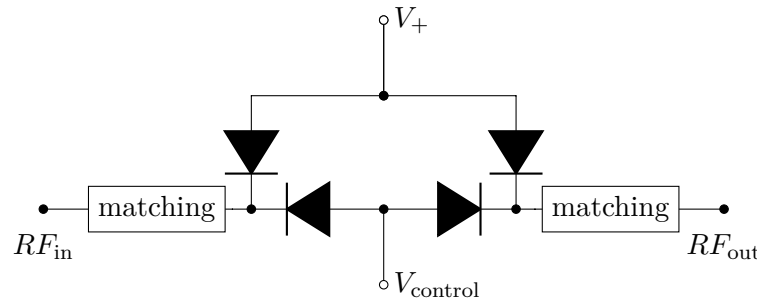
The attenuation versus frequency measurements from the manufactures data sheet are redone to both get a first impression of the device and verify it is generally operational and also as a sanity check for the used laboratory test equipment. Because the signal used by the FLUTE RF system is a 3 GHz single harmonic, the frequency measurement range is augmented over the maximum of 2.5 GHz in the data sheet to 4 GHz. Between the measurement of each network analyzer trace, the control voltage $V_{control}$ of the attenuator is set to 0 V, 2 V, 4 V, 6 V or 12 V. The result is shown in Figure 4.5¹. When comparing the measured plots to the plots in the data sheet, there are obvious discrepancies. For $V_{control} = 0 \text{ V}$ the attenuator is very susceptible to noise on the control input, which could explain the differences for this curve. In the case of 2 V and 4 V, the almost constant offset scales with a similar logarithmic fashion as the attenuation does, which suggests device tolerances causing the deviations.

From this quick examination it is not possible to predict how the attenuator behaves for small changes in $V_{control}$ and how changes in the environment, such as the body temperature or the supply voltage, cause unwanted variations in the attenuation.

¹A thru calibration of the network analyzer reduces the influence of the cables and connectors on the measurement. The change in attenuation due to play in the connectors and slight bend changes in the cables exceeds the trace noise (0.004 dB_{rms}) and causes an uncertainty of about 0.5 dB



(a) left: ZX73-2500-S+ with cover; right: cover removed showing RVA-2500+ and a buffer capacitor



(b) equivalent circuit from the manufacturer (redrawn from [30])

Figure 4.3: The ZX73-2500-S+ controllable RF attenuator by Mini-Circuits

For this reason, with different measurement setups, the ZX73-2500-S+ is examined in greater detail in the next sections.

To compare desired and spurious influences on the attenuation, the following model is used. The attenuation of the ZX73-2500-S+ A depends on the control voltage $V_{control}$ but also on the supply voltage $V+$, the case temperature ϑ_{case} and the RF frequency f :

$$A = \underbrace{A(V_{control}, V+, \vartheta_{case}, f)}_{\vec{x}} = A(\vec{x}) \quad (4.3)$$

Other influences are not modeled as they are difficult to control, such as the manufacturing tolerances between different devices, or assumed to be negligible, such as component degradation or humidity.

In the next sections, the influence of each component of the parameter vector \vec{x} on A is measured. As a coarse approximation, all influences are assumed to have linear effect. Then the total derivative of A , ΔA can be written as

$$\underbrace{A(\vec{x} - \vec{x}_o) - A(\vec{x}_o)}_{\Delta A} = \sum_{j=0}^3 \frac{\Delta A}{\Delta x_j} \Delta x_j \quad (4.4)$$

where the $\Delta A / \Delta x_j$ approximate the partial derivatives dA/dx_j .

With Equation 4.4, the maximum error on the attenuation, that is the variation around the operating point with a fixed $V_{control}$, can be approximated with

$$\Delta A_{max} = \sum_{j=0}^3 \left| \frac{\Delta A}{\Delta x_j} \cdot \Delta x_j \right| = \sum_{j=0}^3 \left| \frac{\Delta A}{\Delta x_j} \right| \cdot |\Delta x_j|. \quad (4.5)$$

If not specified otherwise, the operating point

$$A(\vec{x}_o) =: A_o = A(V_{control}, V+, \vartheta_{case}, f) \quad (4.6)$$

$$A_o = A(10 \text{ V}, 3 \text{ V}, 20^\circ\text{C}, 3 \text{ GHz}) \quad (4.7)$$

is used.

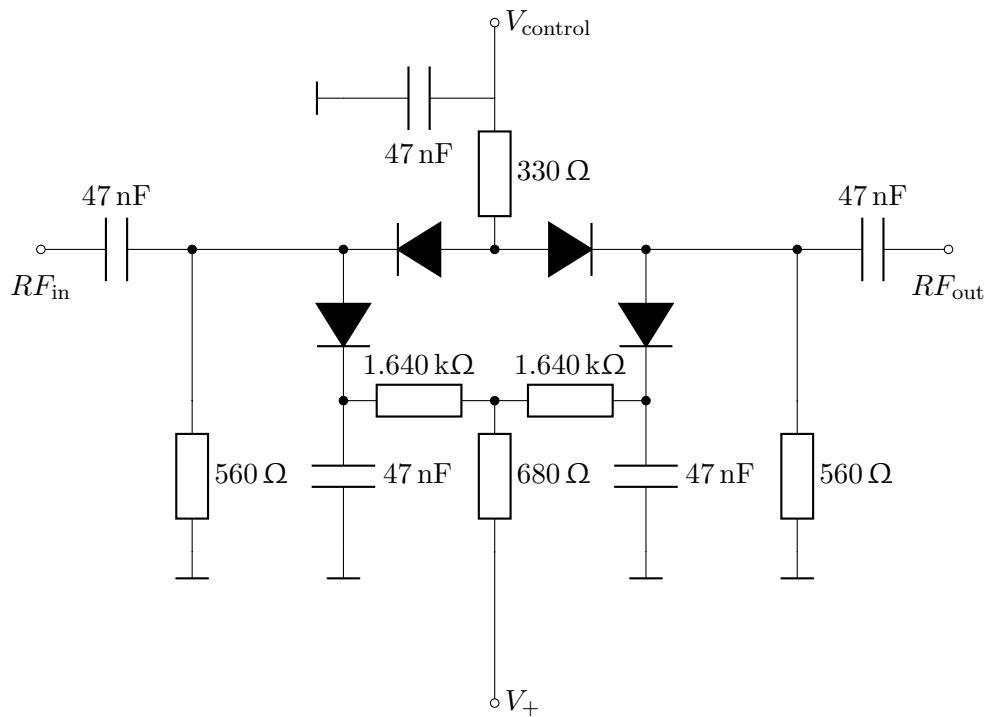


Figure 4.4: Controllable attenuator design around the HP HSMP-3814 RF PIN diodes (redrawn and simplified from [31])

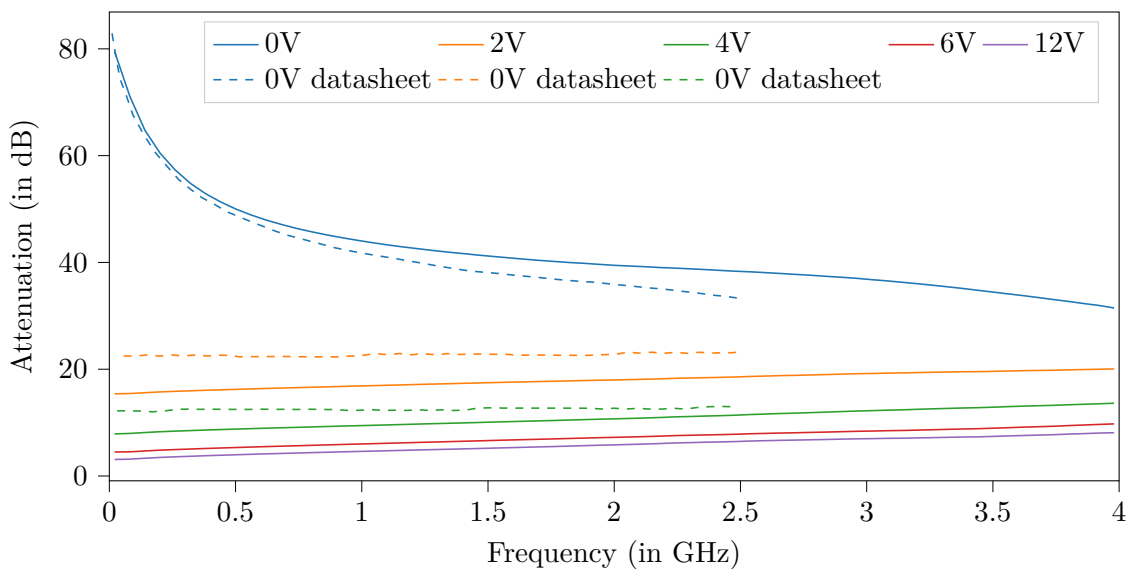


Figure 4.5: Attenuation vs. frequency over DC control voltage; measured with network analyzer (see B.5.1, parameters: #AVG: 16, IF-BW: 10 kHz); plotted in dashed lines are the measurements from the data sheet (see [30, p. 2])

4.2.2.1 Common Measurement Setup

For the following measurements a common setup is used to ease the recording of data and the sequential control for parameter studies. The needed tasks are:

- Supply the attenuator with the supply voltage V_+
- Supply the attenuator with the adjustable control voltage $V_{control}$
- Supply the RF input power with variable frequency f
- Measure the RF output power
- Record all data as time series to a computers storage device

To achieve this, the setup in Figure 4.6 is used. The supply and control voltage are generated by a Keysight 34972A with a 34907A module (see subsubsection B.2.1). To get a more accurate measurement of the actual voltages, two digital multimeters (Models 34470A and 34411A, see subsubsection B.1.2) are connected directly at the $V_{control}$ and V_+ pins. The RF signal is generated by a Rhode und Schwarz SMC 100A signal generator. With the HP E4419B and its two inputs and a power splitter, it is possible to directly get the attenuation of the ZX73-2500-S+. The body temperature of the device is monitored with a PT100 temperature sensor connected to the 34972A.

Each of the lab devices used is compatible with VME eXtensions for Instrumentation protocol specification 11 (VXI-11), which is a widely adopted standard that is used to send American Standard Code for Information Interchange (ASCII) Standard Commands for Programmable Instruments (SCPI) commands over an ethernet network (called LAN eXtensions for Instrumentation (LXI)) or General Purpose Interface Bus (GPIB).[32] This enables remote and programmatically control of the devices over the network. With the library *python-vxi11*, it is now possible to write a custom script, that sets the measurement devices to known initial conditions, drives the inputs of the attenuator and records the generated data. Timing the output of new set-values and recording of data is done with the *Advanced Python Scheduler*.[33]

The whole setup of the hardware in Figure 4.6 and the Python software, a measurement frequency of about 0.5 Hz to 1 Hz can be achieved, which is enough because most measurements taken are of a static nature and in the case of the temperature influence measurement, the thermal time constant is in the order of a few seconds. The limiting device is the HP E4419B which takes the longest to perform one measurement. Without it, measurement frequencies of over 4 Hz are possible.

All measurements are performed in the “RF lab” in building 348 (Karlsruhe Research Accelerator (KARA) hall on KIT Campus North) which is air conditioned to about $(20 \pm 2)^\circ\text{C}$.

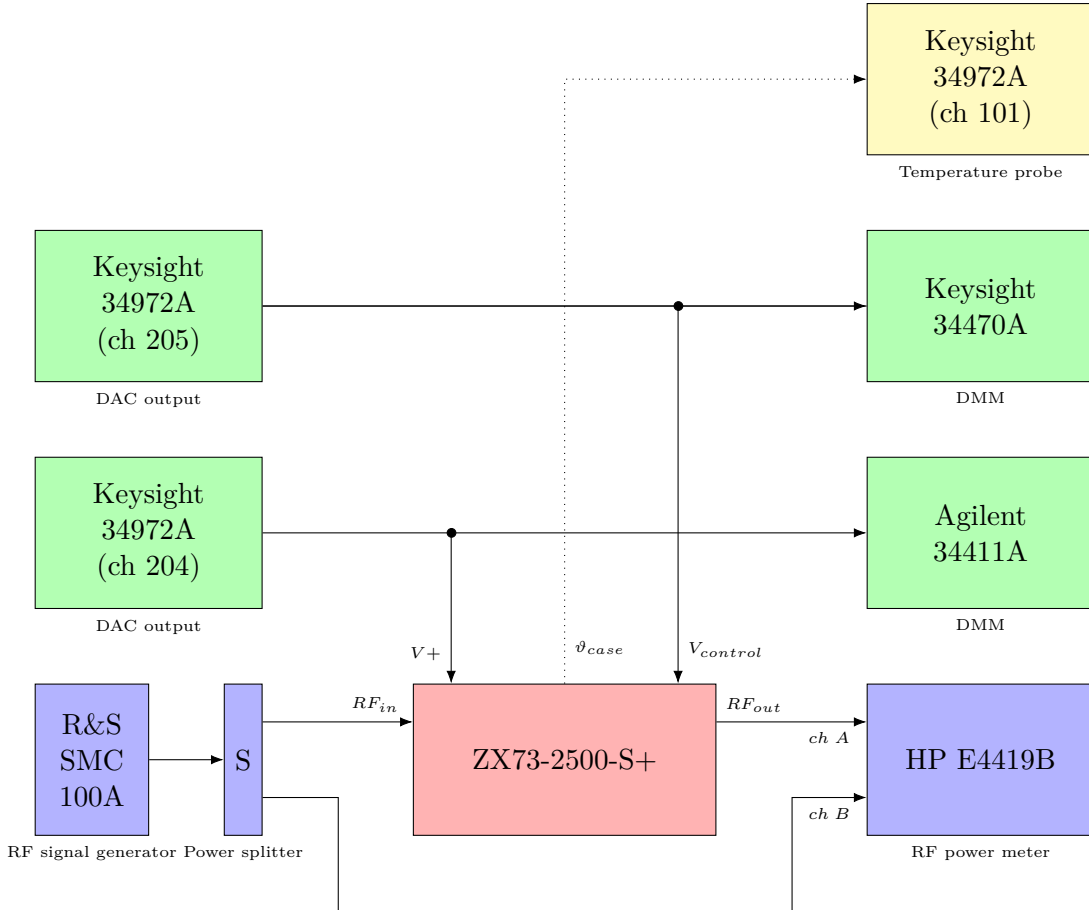


Figure 4.6: Measurement setup: DUT(red), RF generator/power splitter/meter(blue), DC sources/meters(green), temperature probe(yellow)

4.2.2.2 Relation between Control Voltage and Attenuation

In this section, the relation between the control voltage and the attenuation is examined. All other parameters are kept constant:

$$A(\vec{x}) := A(V_{control}) \quad (4.8)$$

The measured spectra in Figure 4.5 already suggest that there is a non linear relationship between the control voltage $V_{control}$ and the attenuation $A(V_{control})$ of the attenuator:

$$A(V_{control}) \neq \text{const.} \cdot V_{control} + A_0. \quad (4.9)$$

This also means the sensitivity

$$S(V_{control}) := \frac{\Delta A(V_{control})}{\Delta V_{control}} \quad (4.10)$$

is not a constant. In other words, for a desired relative change in attenuation, the needed adjustment in $V_{control}$ depends on the chosen operating point $A_o = A(V_{control,o})$.

With all other variables being at the operating point in Equation 4.6, $A(V_{control})$ is measured by stepping $V_{control}$ in 0.1 V increments up and down between 0 V and 12 V several times with each value held constant for 30 s. $A(V_{control})$ is then calculated as the mean of all measurements $A_j(V_{control})$ with the same $V_{control}$ with

$$A(V_{control}) = \frac{1}{N} \sum_{j=0}^{N-1} A_j(V_{control}). \quad (4.11)$$

With the averaging done in Equation 4.11 and $N = 120$, the resulting mean standard deviation is $\sigma_A = 0.00574 \text{ dB}$. Figure 4.7 shows the resulting plot.

The plot shows the attenuation can be varied over more than 30 dB and the magnitude of the sensitivity being large for small control voltages (1 V to 3 V). Since the required change in attenuation of less than 1 dB is much smaller, it is only necessary to vary $V_{control}$ around the operating point.

The optimal operating point for $V_{control}$ is selected by considering the following three aspects. First, the absolute attenuation at the operating point should be as low as possible to not worsen the Signal-to-Noise Ratio (SNR) of the signal path. Second the control voltage has to fit in the possible output voltage range of the voltage source and still allow for adjustment towards both lower and higher voltages. In case of the Keysight 34972A/34907A the maximum possible output voltage is 12 V. Third, the sensitivity should be as low as feasible to make the attenuation less susceptible to noise on the $V_{control}$ input.

For these reasons, $V_{control,o} = 10 \text{ V}$ (as already used in Equation 4.6) is chosen as the operating point, which allows $V_{control}$ to be varied in 8 V to 12 V. At the operating point \vec{x}_o (with $V_{control,o} = 10 \text{ V}$), the measured attenuation is

$$A(V_{control}) = 6.4859 \text{ dB} \quad (4.12)$$

Figure 4.8 shows the attenuation and sensitivity around the operating point.

The sensitivity at the operating point is determined with discrete forward differentiation as

$$S(V_{control}) = S(10 \text{ V}) = \frac{\Delta A}{\Delta V_{control}} = -0.151 \text{ dB V}^{-1}. \quad (4.13)$$

For further error calculations, the maximum $\Delta A(V_{control})/\Delta V_{control}$ is needed. Figure 4.8 shows the maximum magnitude of $\Delta A(V_{control})/\Delta V_{control}$ to be at the lower edge of the $V_{control}$ range of $S(8 \text{ V})$:

$$\left[\frac{\Delta A(V_{control})}{\Delta V_{control}} \right]_{\max} = -0.242 \text{ dB V}^{-1} \quad (4.14)$$

The minimum possible step size of the attenuation can be calculated using $[\Delta A(V_{control})/\Delta V_{control}]_{\max}$ and the DAC output resolution of the Keysight 34907A ($2^4 \text{ V}/2^{16}-1 = 366.22 \mu\text{V}$):

$$\delta A(V_{control}) = 0.242 \text{ dB V}^{-1} \cdot 366.22 \mu\text{V} = 0.00008862524 \text{ dB} \quad (4.15)$$

To assess the stability of $V_{control}$, delivered from the Keysight 34972A (see subsubsection B.2.1) Digital-to-Analog Converter (DAC), its stability over the course of one day is measured. For that the voltage is taken once every 2 seconds with a Keysight 34470A multimeter (see subsubsection B.1.2). The result is shown in Figure 4.9.

This measurement shows the stability of $V_{control}$ to be

$$\sigma_{V_{control}} = 0.173 \text{ mV} \quad (4.16)$$

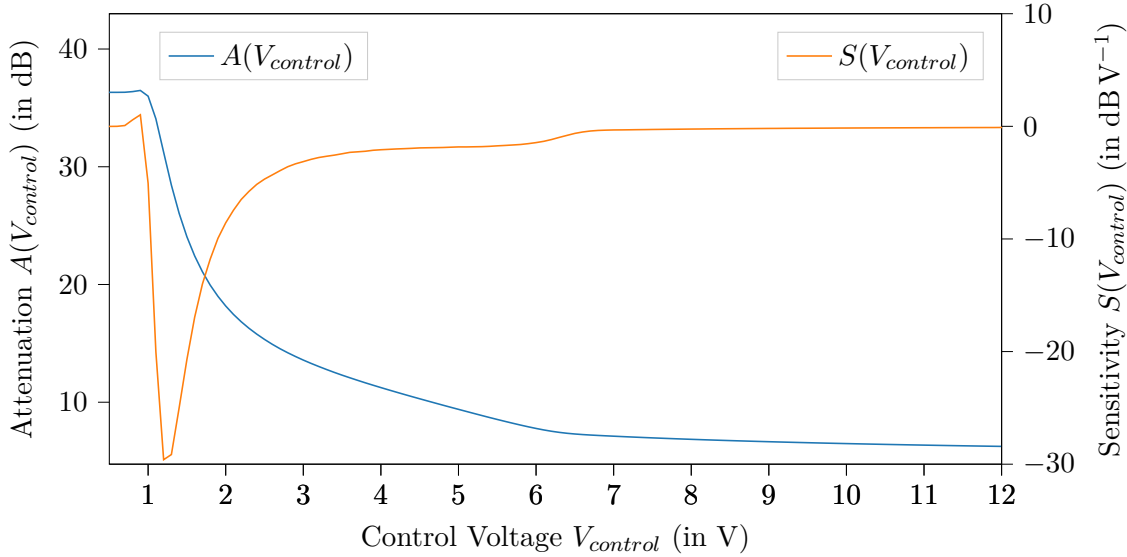


Figure 4.7: Measured attenuation $A(V_{control}, f = 3 \text{ GHz})$ of the ZX73-2500-S+ as a function of the control voltage input $V_{control}$ along with the sensitivity $S(V_{control}, f = 3 \text{ GHz})$

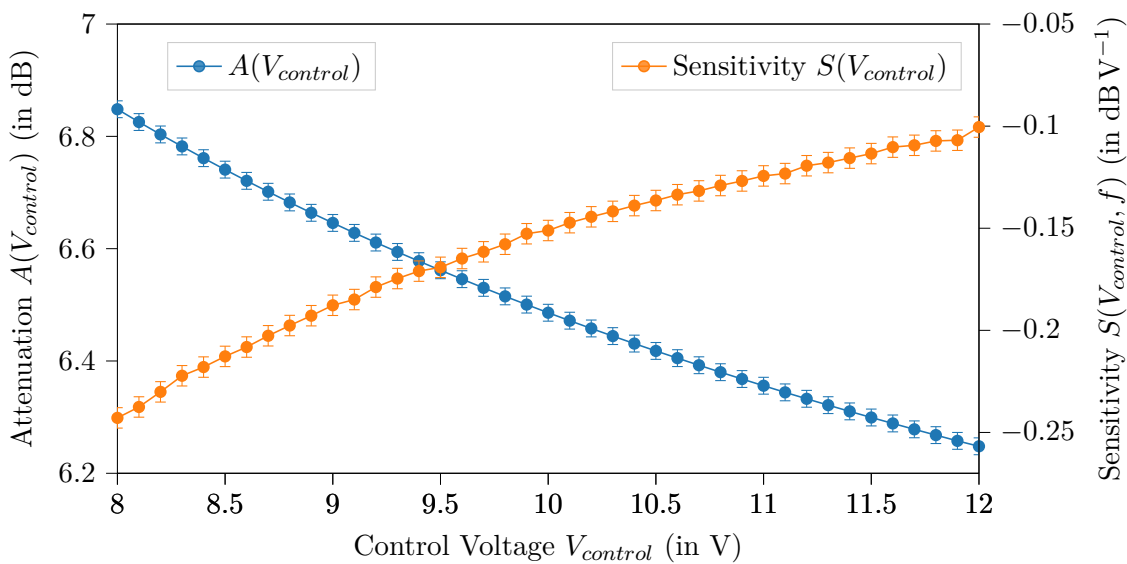


Figure 4.8: Zoomed in version of Figure 4.7 shows the attenuation and sensitivity around the operating point $V_{control,o} = 10 \text{ V}$

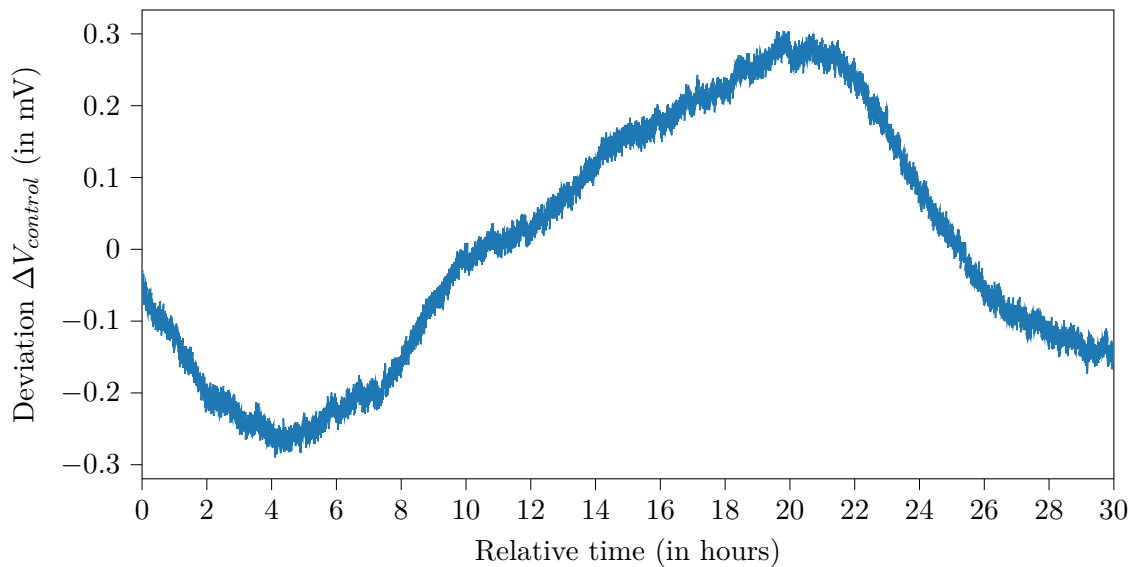


Figure 4.9: Long term stability of $V_{control}$ as delivered by the Keysight 34972A DAC (ch. 205); measured with Keysight 34470A;
room temperature during measurement: $\mu_\vartheta = 19.12^\circ\text{C}$, $\sigma_\vartheta = 0.28^\circ\text{C}$

4.2.2.3 Influence of Supply Voltage Noise on Attenuation

To get the required stability for the power supply voltage, the effect of the supply voltage V_+ on the attenuation $\Delta A/\Delta V_+(V_+)$ has to be examined first. To do that V_+ is varied $\pm 0.2\text{ V}$ around the nominal supply voltage at the operating point $V_{+o} = 3\text{ V}$, all other parameters are kept constant and the attenuation is measured. To make the measurement more robust against fluctuations of the room temperature and drift of the devices, the procedure of stepping through the voltages is repeated in a similar fashion as for the influence of $V_{control}$ and the means for each set V_+ are computed. The result is shown in Figure 4.10.

The plot shows $A(V_+)$ to be of linear nature over the measured range. Therefore using a linear regression of the measured data points, the influence on the attenuation can be estimated to

$$\frac{\Delta A(V_+)}{\Delta V_+}(V_+) \approx \frac{\Delta A(V_+)}{V_+} = \left[\frac{\Delta A(V_+)}{V_+} \right]_{\max} = 0.003\,559\,2 \text{ dB V}^{-1}. \quad (4.17)$$

Next the stability of the supply voltage is measured. for that the stability over the course of one day is measured. The voltage is taken once every two seconds with a Keysight 34470A multimeter (see subsubsection B.1.2). The result is shown in Figure 4.11.

Comparing Figure 4.11 with Figure 4.9 suggest a relation between the deviations in $V_{control}$ and V_+ . Since they are both generated by the same Keysight 34907A module, this is plausible. The slightly changing room temperature is assumed to be the common cause. By calculating the correlation coefficients between ΔV_+ and $\Delta V_{control}$ and also between ΔV_+ and $\Delta \vartheta_{ambient}$, this can be verified:

$$\text{Corr}(\Delta V_+, \Delta V_{control}) = 0.992\,04 \quad (4.18)$$

$$\text{Corr}(\Delta V_+, \Delta \vartheta_{ambient}) = -0.922\,42 \quad (4.19)$$

$$(4.20)$$

The long term measurement yields a standard deviation of

$$\sigma_{V_+,longterm} = 0.154\text{ mV}, \quad (4.21)$$

which is also used as the worst case stability

$$\sigma_{V_+} = 0.154\text{ mV} \quad (4.22)$$

There is also a constant offset of $\mu_{V_+,longterm} = -1.35\text{ mV}$, but it is disregarded since it can easily be compensated by slightly increasing the supply voltage.

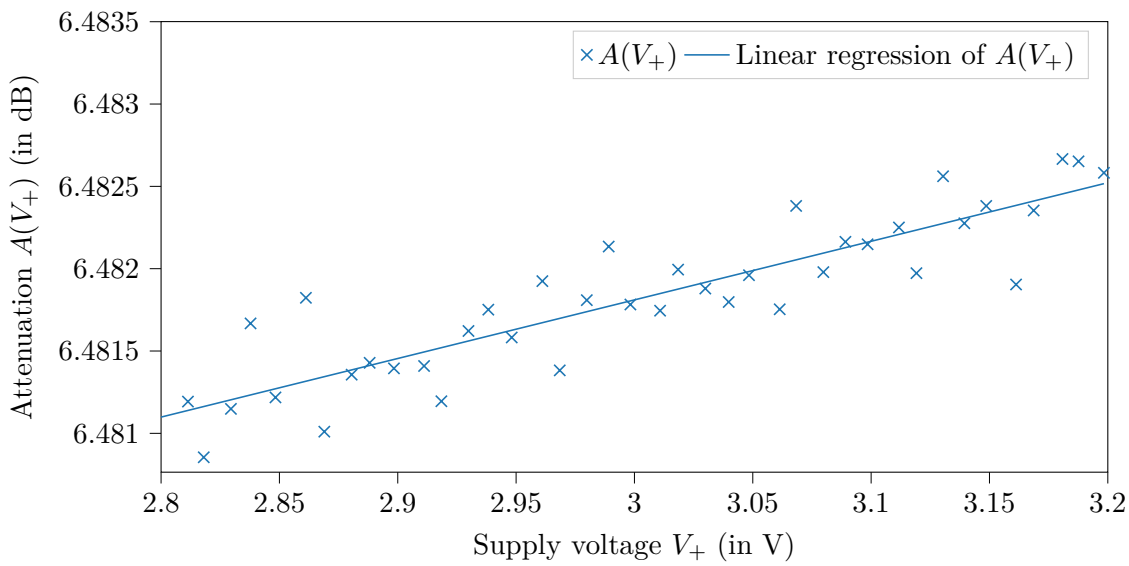


Figure 4.10: Influence of the supply voltage V_+ on the attenuation

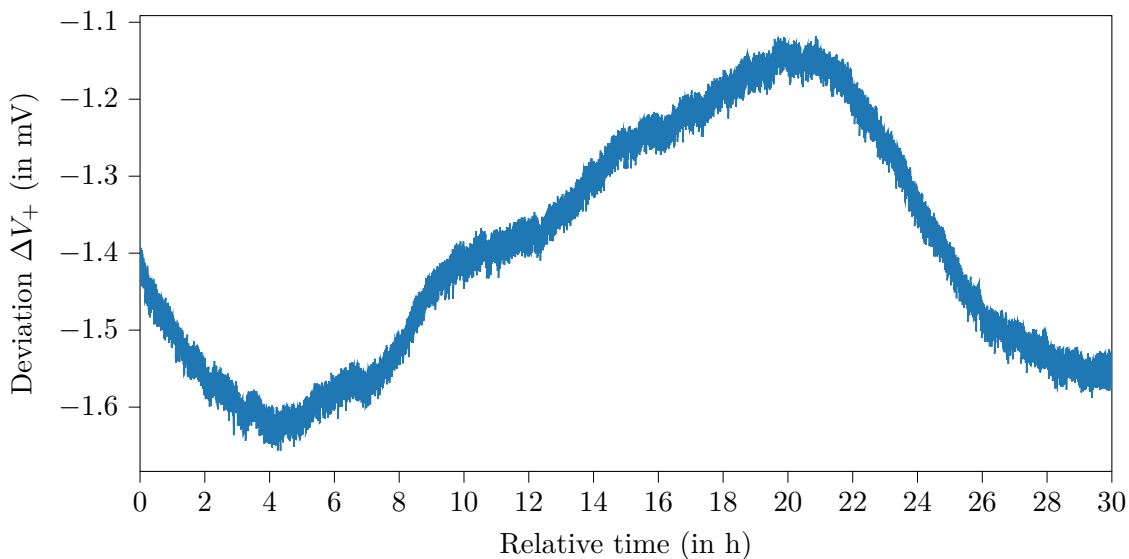


Figure 4.11: Long term stability of V_+ as delivered by the Keysight 34972A DAC (ch. 204); measured with Keysight 34470A;
room temperature during measurement: $\mu_\vartheta = 19.12^\circ\text{C}$, $\sigma_\vartheta = 0.28^\circ\text{C}$

4.2.2.4 Influence of RF Frequency on Attenuation

In this section the influence of a varying RF frequency on attenuation $\Delta A/\Delta f(f)$ is examined. For that the set frequency of the R&S SMC100 signal generator is varied while the attenuation is measured. The result is shown in Figure 4.12.

Phase noise measurements of the FLUTE main oscillator² yield the phase noises

$$\mathcal{L}(f_o = 10 \text{ Hz}) = -78.63 \text{ dBc} \quad (4.23)$$

$$\mathcal{L}(f_o = 1 \text{ kHz}) = -116.26 \text{ dBc} \quad (4.24)$$

$$\mathcal{L}(f_o = 10 \text{ kHz}) = -139.29 \text{ dBc} \quad (4.25)$$

$$\mathcal{L}(f_o = 1 \text{ MHz}) = -142.29 \text{ dBc}, \quad (4.26)$$

with f_o being the offset frequency from the carrier and the unit dBc measuring the offset power from the carrier.

Since this shows the oscillator to be much more stable than $f_o = 10 \text{ kHz}$, it is sufficient to consider only Figure 4.12 (b). In the range of $\pm 1 \text{ kHz}$ around the operating point frequency of 3 GHz, $\Delta A/\Delta f(f)$ is almost constant. From the data points, the value can be calculated to

$$\frac{\Delta A(f)}{\Delta f}(f) \approx \frac{\Delta A(f)}{\Delta f} = \left[\frac{\Delta A(f)}{\Delta f} \right]_{\max} = 0.000\,004\,661\,9 \text{ dB Hz}^{-1}. \quad (4.27)$$

²Using the phase noise analyzer HA7062C by Holzworth, see subsubsection B.6.1

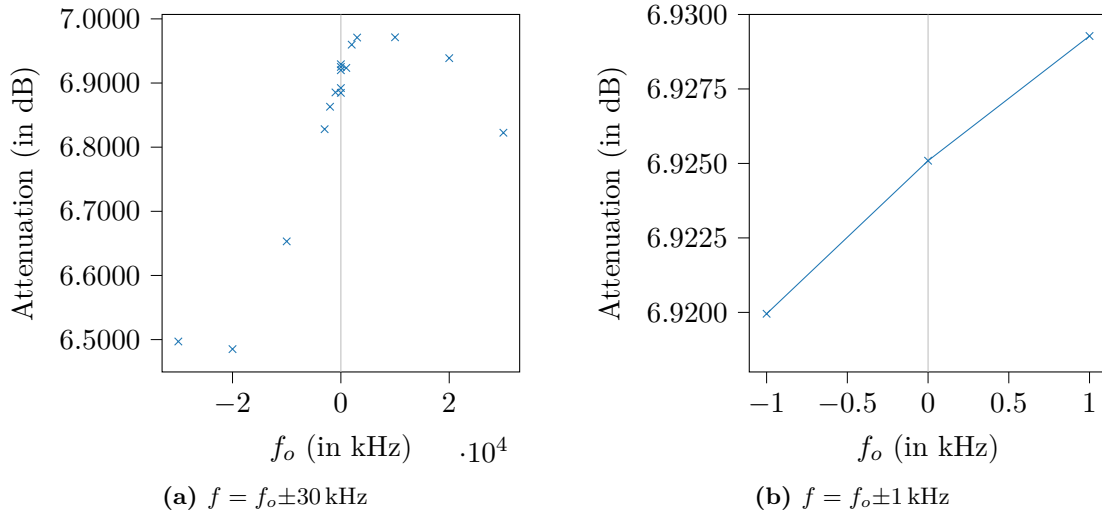


Figure 4.12: Influence of an offset frequency $f - 3 \text{ GHz}$ on the attenuation

4.2.2.5 Influence of Case Temperature Variations on Attenuation

To get insight into the importance of a stable case temperature, its influence on the attenuation $\Delta A / \Delta \vartheta_{\text{case}}(\vartheta_{\text{case}})$ and the temperature stability both in the “RF lab” and the final mounting position inside the FLUTE LLRF cabinet are measured.

To measure $\Delta A / \Delta \vartheta_{\text{case}}(\vartheta_{\text{case}})$, the following experimental setup is used.

The bottom of the attenuator is fixed to a rectangular iron profile with zip ties. Then the iron profile is heated with the tip of a soldering iron (set to 150°C) for 1 min and then allowed to cool for 20 min. This cycle is repeated three times and the device temperature and the attenuation are measured once every 2 s. Due to heat flowing from the soldering iron to the iron profile and through device itself, a strong hysteresis between the heating and cooling cycle can be observed in Figure 4.13.

To get $\Delta A / \Delta \vartheta_{\text{case}}(\vartheta_{\text{case}})$ from the plot in Figure 4.13 an approximately linear relationship $A(\vartheta_{\text{case}})$ is assumed. To get the slope, the ϑ_{case} component of the measured data points $(\vartheta_{\text{case}} | A(\vartheta_{\text{case}}))$ are rounded to one decimal place. Then data points with the same $A(\vartheta_{\text{case}})$ are averaged together and a linear regression is applied to the result. See Figure 4.14 for the resulting plot. The linear regression estimator yields

$$\frac{\Delta A}{\Delta \vartheta_{\text{case}}}(\vartheta_{\text{case}}) \approx \frac{\Delta A}{\Delta \vartheta_{\text{case}}} = \left[\frac{\Delta A}{\Delta \vartheta_{\text{case}}} \right]_{\max} = 0.00432449 \text{ dB } ^\circ\text{C}^{-1}. \quad (4.28)$$

Next, the temperature stability in both the “RF lab” and in the FLUTE LLRF cabinet is measured. For that in each environment the temperature is recorded over night with a thermo element connected to the Keysight 34907A inside the Keysight 34972A every two seconds.

From the data in Figure 4.15, the corresponding stabilities are calculated to be

$$\sigma_{\vartheta_{\text{ambient, RF lab}}} = 0.1067^\circ\text{C} \quad (4.29)$$

$$\sigma_{\vartheta_{\text{ambient, LLRF cabinet}}} = 0.0288^\circ\text{C}. \quad (4.30)$$

This assumes the case of the attenuator and the ambient around it being in thermal equilibrium. With the thick brass case and its only weakly mechanically mounting to the metal support, the attenuator posses a significant thermal time constant $\tau_{\text{th}} = R_{\text{th}} C_{\text{th}}$. Therefore, thermally the attenuator is a lowpass filter and cannot follow fast changes in the ambient temperature. This means only slow changes of the ambient temperature have an influence on A , so short changes, like opening a door, have only a minor effect.

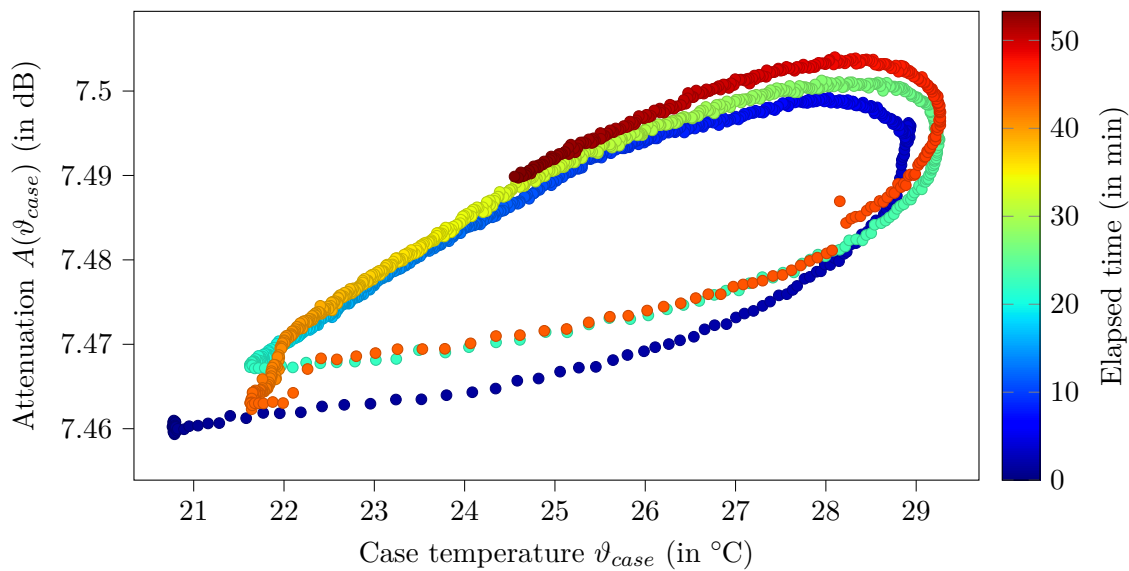


Figure 4.13: Raw measurement result of the influence of the case temperature ϑ_{case} on the attenuation; color coded is the relative elapsed time of the measurement

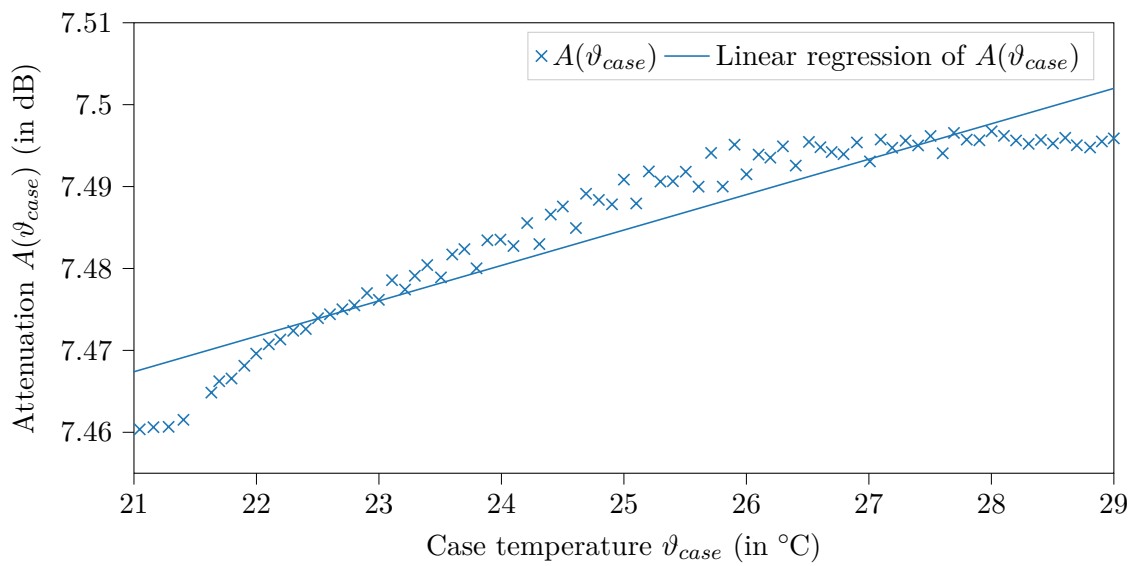


Figure 4.14: Influence of the case temperature ϑ_{case} on the attenuation

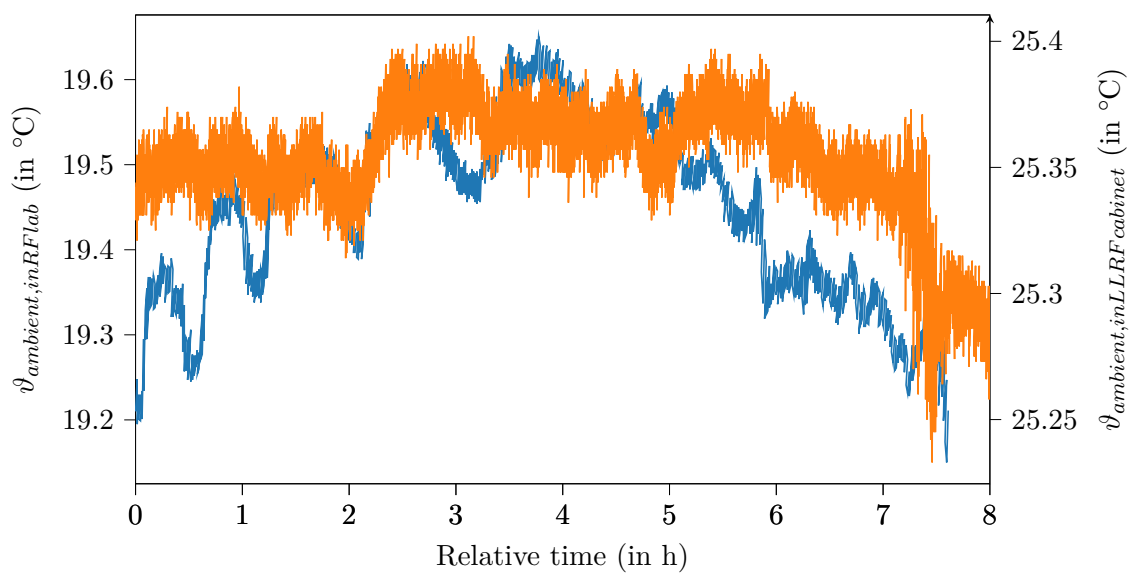


Figure 4.15: Comparison between the temperature stability in the “RF lab” and inside the FLUTE LLRF cabinet

4.2.2.6 $V_{control}$ Frequency response

Using a non inverting adder with a *TS912IN* operational amplifier, a sine wave with constant offset is made, which is then used to drive the control voltage $V_{control}$. The result for different sine wave frequencies is shown in Figure 4.16.

This result is to be interpreted purely qualitatively, as neither measurement device and software is designed, nor is the circuit used optimal. But the traces in Figure 4.16 verify that the ZX73-2500-S+ attenuator is able to follow changes of $V_{control}$ at least up to a few ten kHz. If the attenuator should be set to a new value, this is equivalent to applying a step at the attenuators $V_{control}$ input, which according to the Fourier transform of a $\text{rect}(t)$ pulse, a $\text{sinc}(f)$ contains high frequencies.

This is at several orders of magnitude bigger than the control system can input, compute and output new values to the attenuator.

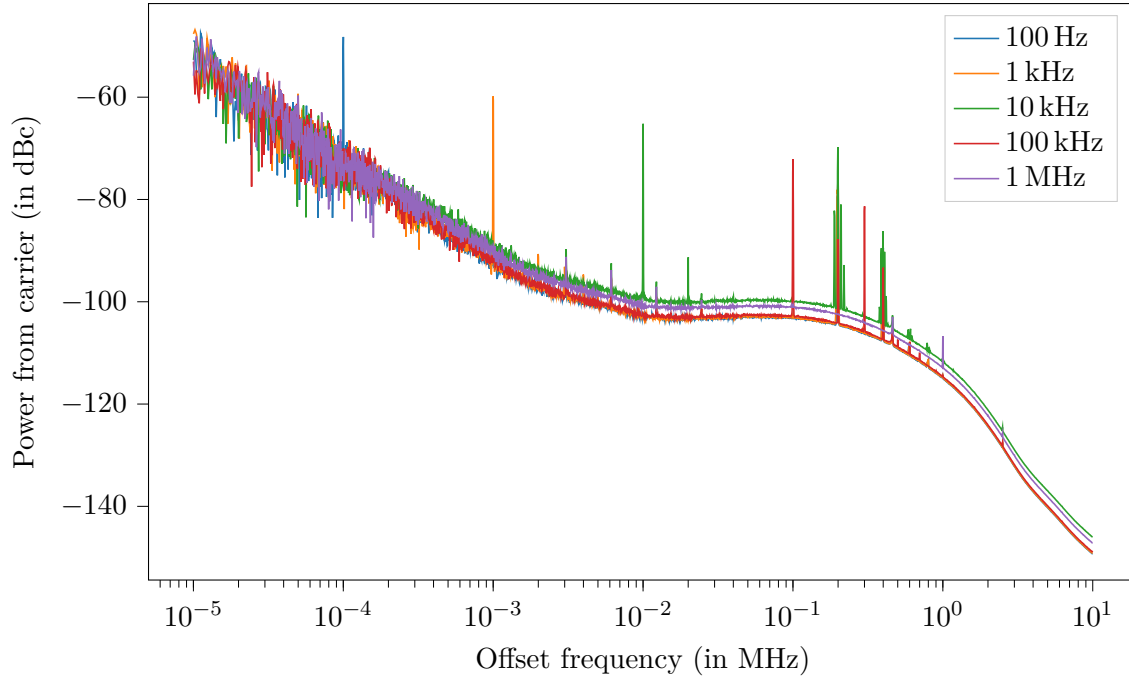


Figure 4.16: Spectrum (measured with Holzworth HA7062A (subsubsection B.6.1)) showing the effect of modulating $V_{control}$ with different frequencies (Modulation amplitude: 1 V)

4.2.2.7 Combined Maximum Error of the Attenuation and Conclusion

Using Equation 4.5 and setting $\Delta x_j = \sigma_{x_j}$ and $\Delta A/\Delta x_j = [\Delta A/\Delta x_j]_{\max}$, the upper bound on the deviation of the attenuation, that is the error ΔA in the worst case, can now be calculated:

$$\Delta A_{\max} = \sum_{j=0}^3 \left| \frac{\Delta A}{\Delta x_j} \cdot \Delta x_j \right| \quad (4.31)$$

$$= \left| \frac{\Delta A}{\Delta V_{control}} \cdot \Delta V_{control} \right| + \left| \frac{\Delta A}{\Delta V_+} \cdot \Delta V_+ \right| + \left| \frac{\Delta A}{\Delta f} \cdot \Delta f \right| + \left| \frac{\Delta A}{\Delta \vartheta_{case}} \cdot \Delta \vartheta_{case} \right| \quad (4.32)$$

$$= \underbrace{0.242 \text{ dB V}^{-1} \cdot 0.173 \text{ mV}}_{41.9 \mu\text{dB}} \quad (4.33)$$

$$+ \underbrace{0.0035592 \text{ dB V}^{-1} \cdot 0.154 \text{ mV}}_{548 \text{ ndB}} \quad (4.34)$$

$$+ \underbrace{0.00000466 \text{ dB Hz}^{-1} \cdot 0 \text{ Hz}}_{0 \text{ dB}} \quad (4.35)$$

$$+ \underbrace{0.004325 \text{ dB } ^\circ\text{C}^{-1} \cdot 0.11 \text{ }^\circ\text{C}}_{475.75 \mu\text{dB}} \quad (4.36)$$

$$= 518 \mu\text{dB} = 0.000518 \text{ dB} \quad (4.37)$$

This shows even in the worst case, the ZX73-2500-S+ attenuator is stable within the requirement.

The other requirements from Table 4.2 are also fulfilled, see Table 4.3.

Table 4.3: Controllable RF attenuator evaluation test results

Requirement	Value/Range set	Value/Range actual	Verdict
attenuation adjustment	$\geq \pm 0.2 \text{ dB}$	$\pm 0.3 \text{ dB}$	pass
attenuation stability	$\leq \pm 0.001 \text{ dB}$	0.000518 dB	pass
nominal attenuation at operating point	$\leq 10 \text{ dB}$	6.6 dB	pass
attenuation resolution	$\leq 0.001 \text{ dB}$	0.000089 dB	pass
setup time	$\leq 10 \text{ ms}$	1 ms	pass
operating temperature range	$(25.0 \pm 0.1) \text{ }^{\circ}\text{C}$	$(25.0 \pm 0.1) \text{ }^{\circ}\text{C}$	pass
supply voltage	3 V to 12 V	3 V	pass
control voltage	3 V to 12 V	8 V to 12 V	pass

4.2.3 Test of the Attenuator with FLUTE

In this section the attenuator is mounted at FLUTE and its function is verified against the data gathered in the lab in earlier sections.

The attenuator is installed at its final mounting location inside the LLRF cabinet in the FLUTE bunker basement and is connected between the output of the vector modulator (after the oscillator, not shown in Figure 3.1) and the input of the pre-amplifier. With the controllable attenuator at its operating point, the signal path now contains an attenuation of about 6 dB at all times. To compensate for, the attenuation at another attenuator inside the LLRF system is lowered accordingly.

After all components of FLUTE are warmed up to operational temperatures, the attenuation versus control voltage curve $A(V_{\text{control}})$ is measured again (compare the lab measurement Figure 4.7).

To do so, the control voltage V_{control} is varied in 0.5 V steps (see Figure 4.17), with each step kept for 20 min. Synchronous to that, the RF power of the cavity is recorded (see Figure 4.18), from which the attenuation A can be calculated. Computing the averaging over each step yields $A(V_{\text{control}})$. It is depicted in Figure 4.19 together with its uncertainty.

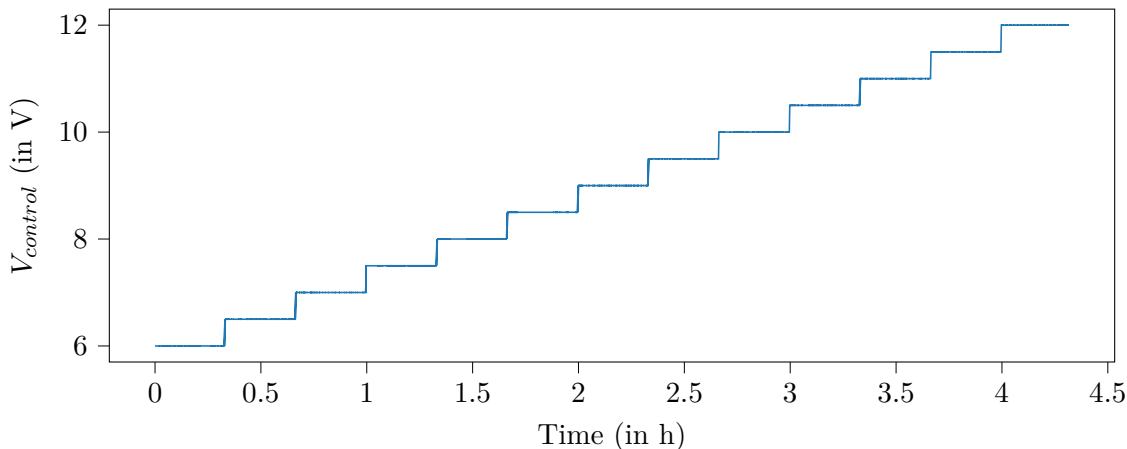


Figure 4.17: Time signal V_{control} used to calculate Figure 4.19

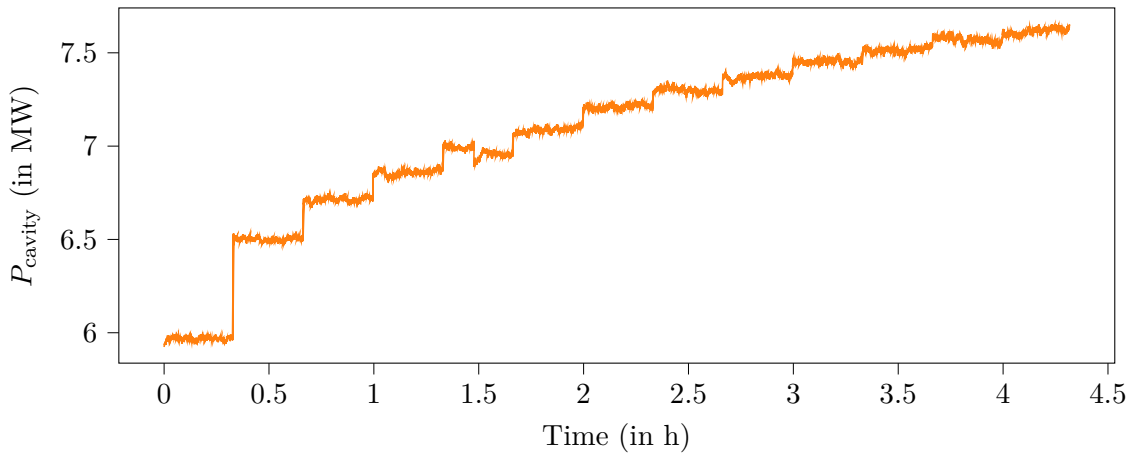


Figure 4.18: Time signal $A(V_{\text{control}})$ used to calculate Figure 4.19

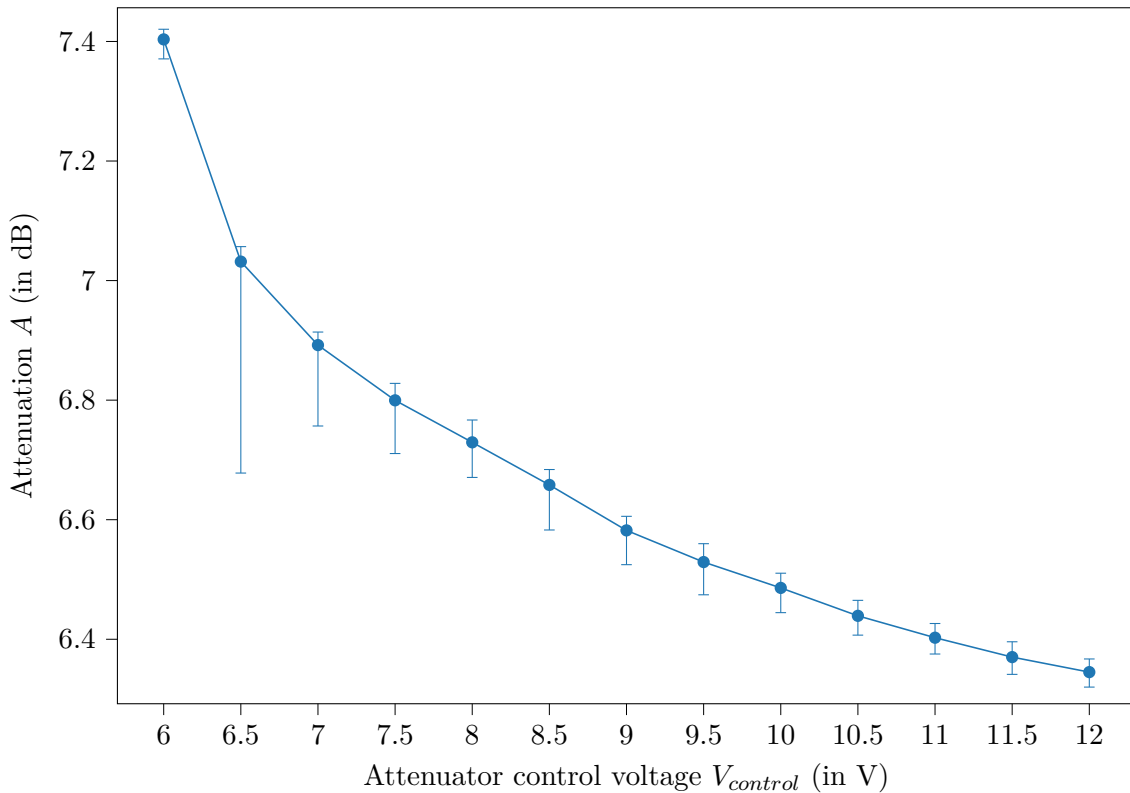


Figure 4.19: Measured $A(V_{\text{control}})$ with FLUTE; error bars show the span between minimum and maximum values in each V_{control} step

5. Controller Design and Evaluation

In this chapter a control system is designed and evaluated to stabilize FLUTEs RF system. Referring back to the block diagram of a generic control system in Figure 2.1, there are three blocks to determine. First the plant transfer function, which describes the system that is to be controlled. Second, based on the plant, an appropriate controller type is chosen and its parameters are calculated. Third a measurement filter is used to improve the quality of the feedback signal path. As the choice of the measurement filter influences the controller design, its design is treated before the controller.

5.1 Plant Identification

5.1.1 Principle

Before choosing an appropriate controller, some insight of the system response has to be obtained. Therefore in this section the plant's transfer function is estimated. In the context of this chapter "plant" refers to everything from the attenuation set at the controllable attenuator to the system output, e.g. the cavity RF power.

In the time domain, a LTI system is described by its impulse response $h(t)$, that is the reaction of the plant to an impulse at the input. Using this definition directly, the plant's impulse response $p(t)$ could be measured by applying a short peak in the attenuation setting on the attenuator. The effect on the output is not easy to measure and a single measurement of this kind is very susceptible to noise. Therefore it is more common to measure the step response[34], which is the output of a system, when a step function is applied to its input. As the step function is the time integral of the impulse function, the step response can be converted to the impulse response by differentiation in time.

Instead of measuring a single step response, often several step responses are measured and their average is computed to reduce the variance of the estimation. When measuring a step response the minimum needed measuring time depends on the systems time constants, but they are often not known beforehand.

That is why when there is no prior knowledge of the system, the identification is sometimes done with a Pseudo Random Binary Sequence (PRBS) to excite the system with step functions of different lengths. The PRBS is chosen in a way that some of the steps will probably last longer than a few dominant time constants of the system.

To get the transfer function $P(s) = \mathcal{L}\{p(t)\}$ of the plant from its step response(s), several methods are common, including correlation based and frequency response based algorithms.

5.1.2 Identifying the Plant Attenuator+RF

The input PRBS signal is generated with the Python script in Listing 5.1. Based on the value of a pseudo random number generator, the sequence toggles the attenuator between $V_{\text{control}} = 7 \text{ V}$ and $V_{\text{control}} = 11 \text{ V}$. Using Figure 4.7, this equals a span in attenuation of

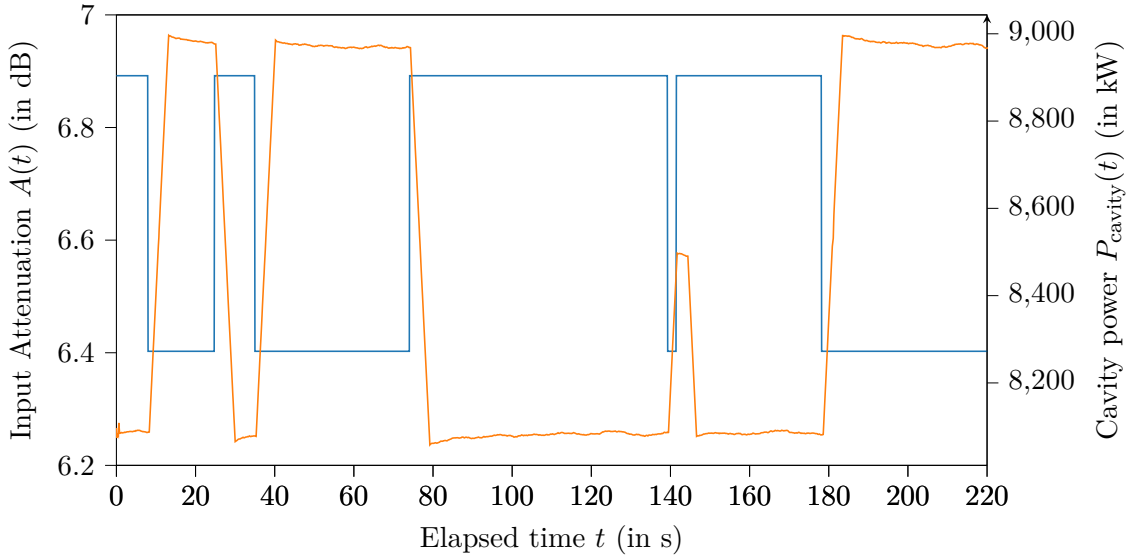


Figure 5.1: Section of the input sequence (blue) and the system response (orange); Note the inverse relation: A higher attenuation A causes a lower cavity power P_{cavity}

6.892 dB to 6.4026 dB. With the parameter `toggleP`, the average length of one constant voltage level can be controlled.

Listing 5.1: Function to get a pseudo random binary sequence

```

1 def randomBinarySequence(N,toggleP):
2     u=[False]*N
3     for i in range(1,len(u)):
4         if(np.random.binomial(1, toggleP, 1)[0]):
5             u[i]=not u[i-1]
6         else:
7             u[i]=u[i-1]
8     return list(map(lambda x: 7 if x==False else 11,u))

```

In a test run over six hours (after all FLUTE subsystems had stabilized), the attenuator was driven with such a PRBS. The result is shown in Figure 5.1.

The time signals $A(t)$ and $P_{\text{cavity}}(t)$ are then split into a *estimation* data set (about 80 % of the samples) and a *validation* data set (the remaining $\approx 20 \%$). This is done so the bulk of the available information is used to estimate the model, but there is data left that the model hasn't seen before. This smaller portion is used to validate the models performance, hence it is called the validation data set.

The two data sets are then loaded into the MATLAB *System Identification Toolbox*. With the toolboxes pre-processing tools, first the means of both the input and output are removed, which is required by the estimators used. Then, using the “process model” estimator, linear, continuous time transfer functions with different numbers of zeros and poles are estimated (See screenshot of the Graphical User Interface (GUI) in Figure A.1). After that, to check the accuracy of the estimations, the System Identification Toolbox is used to simulate the output of the estimated systems (see Figure 5.2). For that the aforementioned validation data set is used: The measured output is compared with the outputs predicted by the models.

Using the Matlab function `zpk()` the models are converted into the zero-pole-gain representation. In Table 5.1 the estimated models are listed with their zeros, poles, gains and the model fit, as it is computed by the System Identification Toolbox. P1, P2 and P3 are

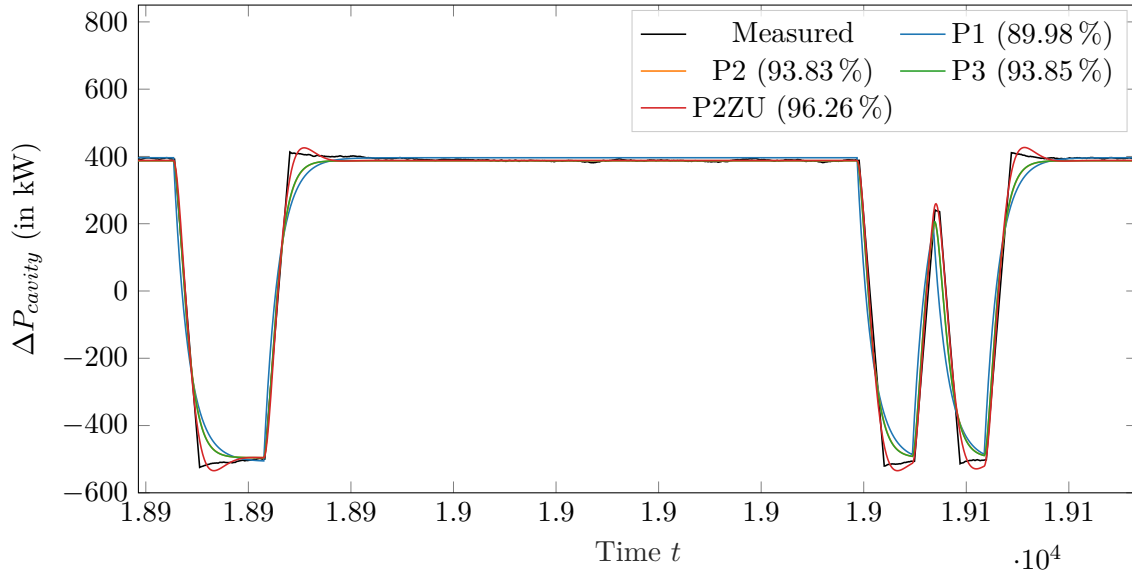


Figure 5.2: Validation of the estimated process models for the plant; the legend also shows the model fits in percent

Table 5.1: Process models of the plant as estimated by the Matlab System Identification Toolboxes process model estimator

Model name	Zeros	Poles	Gain	Model fit
P1		$(s + 0.3505)$	-646.94	89.98 %
P2		$(s + 0.6875)(s + 0.7039)$	-873.18	93.83 %
P3		$(s + 1 \times 10^6)(s + 0.7376)(s + 0.669)$	-8.9019×10^8	93.85 %
P2ZU	$(s - 2846)$	$(s^2 + 0.8014s + 0.3195)$	0.20296	96.26 %

models with one, two and three poles and a gain as free parameters. P2ZU consists of a complex pole pair, a zero and a gain.

Figure 5.2 and Table 5.1 show the P2ZU model to have the best fit. Therefore it is accepted as the plants transfer function. Using the Matlab function `tf()`, its time continuous transfer function can be stated as

$$P(s) = \frac{0.6352s - 1808}{3.13s^2 + 2.508s + 1}. \quad (5.1)$$

Using the Matlab function `c2d()`¹ and the sample time $T_s = 0.2\text{ s}$, $G(s)$ can be converted to the time discrete transfer function

$$P[z] = \frac{-10.91z^{-1} - 10.41z^{-2}}{1 - 1.84z^{-1} + 0.8519z^{-2}}. \quad (5.2)$$

The high model fit percentage of 96.26 % justifies the choice of a linear model with few parameters and further estimation attempts using other (non-) linear models are not needed. Considering the accuracy of the model, it is important to note this estimation is only valid at the time the measurements are taken. With FLUTE being a large experimental setup being still under commission, it is always possible that small changes to certain (sub-) systems can lead to minor or major influences to others. For the time being, the estimation is redone a day later and for both measurements days, different parts of the about six hour

¹Without specifying a different method, `c2d()` discretizes the continuous-time model zero-order hold on the input.

measurements each are used as the estimation and validation data sets. Doing so shows no significant change in the estimated coefficients and the resulting model fits, indicating the estimated models are at least plausible.

To account for errors in the estimated model (and possible other errors), when designing the controller, sufficient gain and phase margins are set to ensure stable operation.

5.2 Measurement Filter

Like all measurements of physical quantities, the measuring of the system output of the control system is subjected to noise. In addition to these disturbances of thermal or electrical origins, also high frequency variations of the system output has detrimental effects on the control systems performance. For example the magnitudes of the bunch-by-bunch changes of the measured cavity power are often in the same order as the long-term drifts. Trying to correct for them instead of the long term drifts often leads to overcompensating and can even make the system unstable.

To remove the high frequency components a low pass filter is used as the measurement block $H(s)$.

In pre-tests the incoming signal was simply filtered with a moving average filter. Commonly, the moving average is defined as the mean of a signal x inside a window of length L , centered around the current time or sample index n , that is shifted along the signal. This smooths out small variations thus the moving average acts as a low pass filter. This *non-causal* version of the moving average can only be used with already measured data as to compute the moving average at n , future values at $n + i$ are needed:

$$\text{MA}_{x,\text{non-causal},L}[n] = \frac{1}{L} \sum_{i=n-\frac{L-1}{2}}^{n+\frac{L-1}{2}} x[i] \quad (5.3)$$

When filtering real-time data, future values are not available and a shifted, *causal* version, of the moving average

$$\text{MA}_{x,\text{causal},L}[n] = \frac{1}{L} \sum_{i=n-(L-1)}^n x[i] \quad (5.4)$$

is used.

In case of the cavity RF power, experiments show a window length of about $L = 100$ or more is necessary to sufficiently smooth the measured power signal. When comparing the original signal with the filtered one, it is apparent that in addition to the desired smoothing effect, the filtered signal also is delayed in time, with the delay being dependent on the window size. To quantify the delay, the alternative definition of the moving average as a digital FIR filter is used. One possibility to describe a FIR filter is by giving its impulse response, i.e. the output signal when the input of the filter is an impulse with unity height. In case of the moving average filter, the coefficient sequence of the corresponding FIR filter has the length $N = L$ and is equal to the the impulse response $h[n]$:

$$h[n] = \frac{1}{N} \underbrace{[1, 1, \dots, 1]}_N \quad (5.5)$$

The delay introduced by a digital filter can be quantified with the filter's group delay

$$\frac{\tau_g(f)}{T_s} = \frac{d\phi(f)}{df} \quad (5.6)$$

which is given normalized to the sampling time T_s [35, p. 70]. In case of a FIR filter with linear phase (with a symmetrical impulse response), the group delay is always constant over all frequencies and is only dependent on the filter length N [35, p. 165]:

$$\frac{\tau_g(f)}{T_s} = \frac{d\phi(f)}{df} = \frac{d\phi}{df} = \frac{N}{2} \quad (5.7)$$

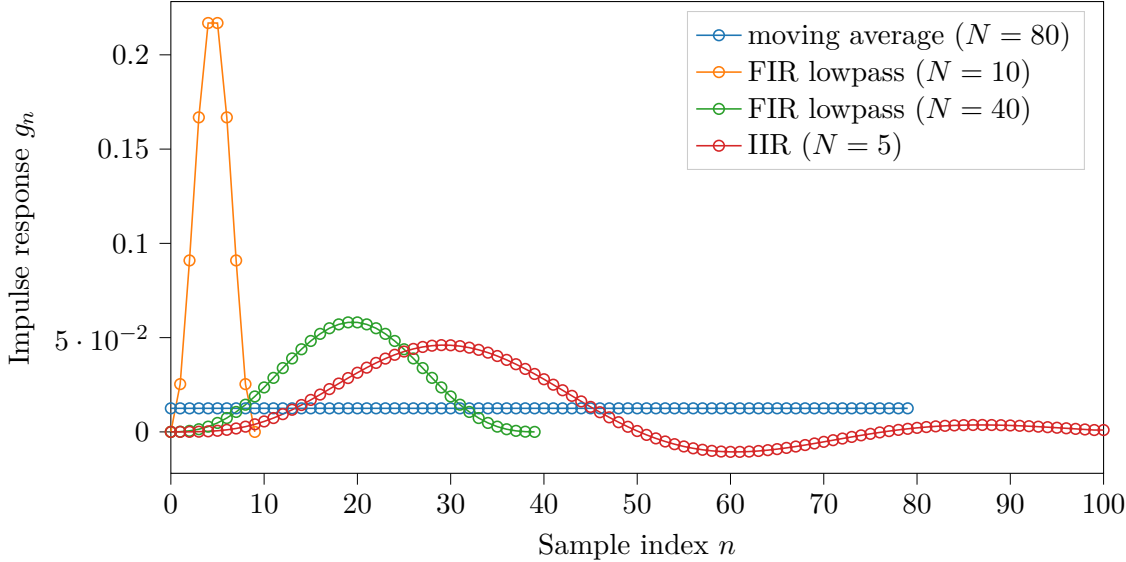


Figure 5.3: Impulse responses of a moving average filter ($N = 100$), a FIR lowpass ($N = 50$, $f_c = 0.1$ Hz) and a IIR Butterworth lowpass ($N = 50$, $f_c = 0.1$ Hz)

With a sampling time of $T_s = 1/5$ Hz = 200 ms and $N = 100$ the group delay is 10 s. In case of a steady operation this is acceptable, as the disturbances to compensate happen on a timescale in the order of several minutes. But in case of ongoing transients due to user changes to the control system parameters or short error bursts on the measured signal, this long delay causes problems and therefore should be reduced.

Therefore a more sophisticated digital filter is designed to replace the simple moving average.

On the one hand, a FIR filter is designed with the Kaiser window method. This method starts with the desired frequency response, which is usually given piece-wise. In case of the low pass filter it is a step function at a cutoff frequency f_c . Then the IDFT is used to compute the corresponding impulse response $h_{\text{IIR}}[n]$, which is in general infinitely long. Windowing with e.g. a Kaiser window and then truncating the impulse response yields the impulse response of the desired FIR filter $h_{\text{FIR}}[n]$.[36, p. 533]. With SciPy using `b=signal.firwin(N, fc, fs)`, the coefficients of a FIR with this method can be calculated.

On the other hand, an IIR filter is designed with the impulse invariance method and an analog Butterworth filter. This method could be interpreted as sampling the infinitely long analog impulse response.[36, p. 497] In SciPy using `b,a=signal.butter(N,fc,'lowpass',fs,)`, the coefficients of an IIR can be calculated with this method. For an IIR filter, the group delay cannot be calculated with Equation 5.7 and it is in general frequency-dependent.

Figure 5.3 shows the impulse responses of the moving average, the FIR lowpass and the IIR lowpass (truncated to $N = 100$).

In Figure 5.4, the three filter types described above are compared by filtering a ten minute long segment of pre-recorded data. The filtering is done with the SciPy function `signal.lfilter()` which does causal filtering and does not compensate group delay², so the results are the same as they would be for real-time data.

The plot shows the FIR lowpass filter requiring ten times the number of coefficients to achieve about the same result as the IIR lowpass filter. Also the moving average filter

²In contrast to `signalfiltfilt()`, which applies the filter both forward and backward achieving zero phase/group delay, but this cannot be done for incoming real-time data.

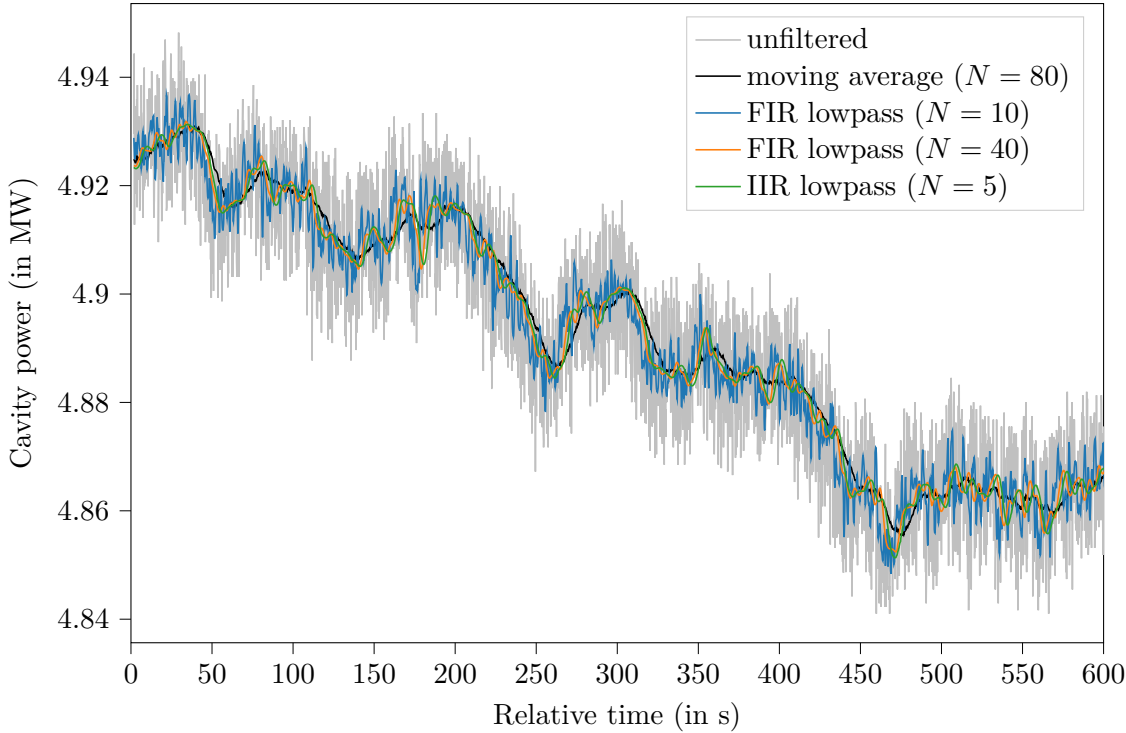


Figure 5.4: Effects of the three different lowpass filters in Figure 5.3 on noisy data

has double the number of coefficients as the FIR lowpass filter, but there is still high frequency noise in the output (caused by the $\text{sinc}(\cdot)$ shape of its frequency response $H[f] = \text{DFT}\{h[n]\}$).

Compared to the FIR lowpass, the moving average offers no benefit besides its easy implementation. When comparing the FIR with the IIR approach, the IIR has the advantage of needing less coefficients, thus occupying less memory, which is not really an advantage when the control system is implemented on a personal computer, which typically has enough free memory to hold millions of floating point numbers. Also the IIR filter has a non-constant group delay and is not guaranteed to be stable like all FIR filters are.

For these reasons, in the following a FIR lowpass filter is used.

One example filter generated with `signal.firwin()` with a cutoff frequency $f_c = 10\text{ mHz}$ and order $N = 10$ has the transfer function

$$H[z] = \frac{1}{b_{10}z^{10} + b_9z^9 + b_8z^8 + b_7z^7 + b_6z^6 + b_5z^5 + b_4z^4 + b_3z^3 + b_2z^2 + b_1z + b_0} \quad (5.8)$$

with the coefficient vector $\vec{b} = [b_{10}, \dots, b_0]$, with

$$\vec{b} = [0.0876, 0.0896, 0.0911, 0.0922, 0.0929, 0.0931, 0.0929, 0.0922, 0.0911, 0.0896, 0.0876]. \quad (5.9)$$

Instead of stating the transfer function, a plot of the poles and zeros is a more intuitive representation. In Figure 5.5, the poles and zeros of the FIR filter with $N = 10$ are compared to one with $N = 40$. In addition, Figure 5.6 shows the magnitude responses of such filters.

For a fixed cutoff frequency and variable order N , the trade-off for choosing N is between the group delay introduced by the filter (see Equation 5.7) and the width of the transition band or in other words the sharpness of the filter. This can be seen by comparing the cases

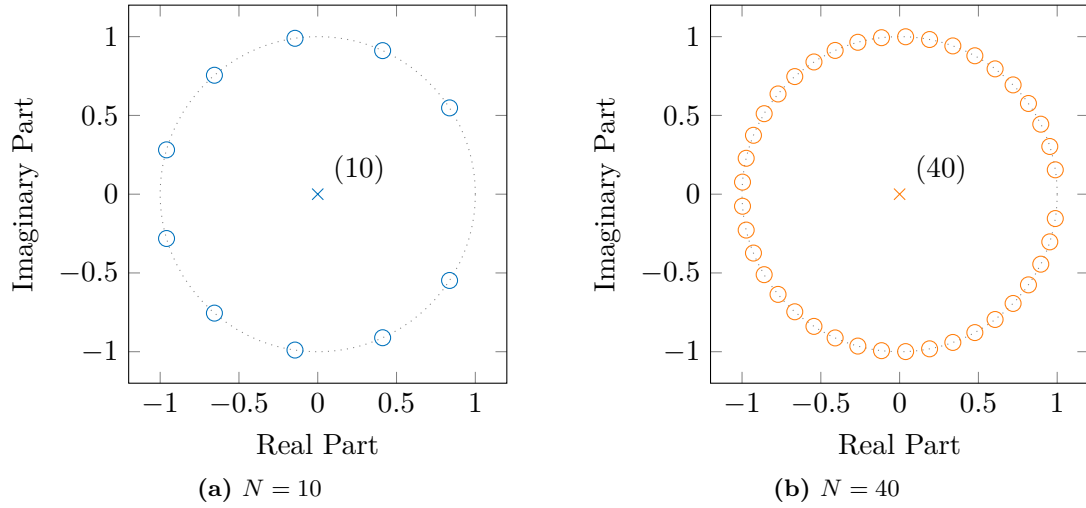


Figure 5.5: Pole-Zero maps for two FIR filters with a common cutoff frequency $f_c = 10 \text{ mHz}$ but different filter orders N ;
○ denotes zeros, × denotes poles, (k) is a k -times pole

$N = 10$ and $N = 40$ for the FIR filters in Figure 5.4: While the smoothing-effect of the longer filter is obviously better, it also causes a higher group delay, which results in the filter result of the $N = 40$ filter being shifted in time by $\frac{40}{2}T_s = 4\text{s}$ compared to $\frac{10}{2}T_s = 1\text{s}$ in case of $N = 10$. While a high smoothness is desired for the control system to reject high frequency noise, using a filter with a too high order can introduce a group delay high enough to shift the closed-loop from negative to positive feedback, thus making it unstable.

For the controller design in the next section and the later implemented real-time system, the cutoff frequency and the filter order are kept variable to leave room for improvement.

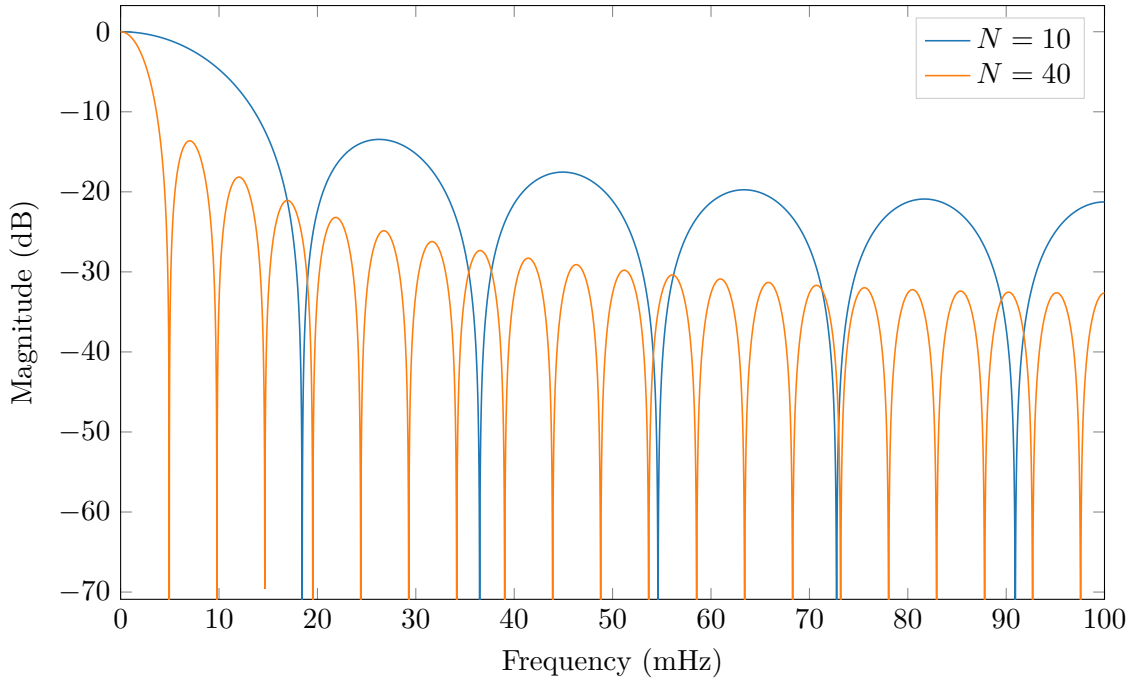


Figure 5.6: Magnitude response of two FIR filters with a common cutoff frequency $f_c = 10 \text{ mHz}$ but different filter orders N

Real-time implementation of a FIR Filter in Python

Similar to Equation 5.4, a FIR filter designed with the SciPy function `signal.firwin()` can be used in a causal manner to filter real-time data.

Applying the filter on pre-recorded data, like in Figure 5.4 can be done with `signal.lfilter()`. To use `signal.lfilter()` on sample-wise incoming real-time data, the “initial in” input and “final out” output of `signal.lfilter()` can be used to keep the filters state. This is demonstrated in Listing 5.2 by looping through pre-recorded data point-by-point.

Listing 5.2: Demonstration of the `zi` and `zf` variables when using `signal.lfilter()`

```

1 x=df2["F:RF:LLRF:01:GunCav1:Power:Out Value"].to_numpy()
2 y=np.array([])
3 zf=signal.lfilter_zi(b, 1)
4 for i in range(len(x)):
5     y0,zf=signal.lfilter(b, 1, [x[i]], zi=zf)
6     y=np.append(y,y0[0])

```

5.3 Controller Design

Based on the estimated model of the plant $P(s)$ (or $P[z]$) in section 5.1 and the type of measurement filter designed in section 5.2, in this section an appropriate controller to stabilize the plant is designed and its performance is evaluated.

Tuning the controller and testing its capabilities is performed both *offline* with simulations using the building blocks $P[z]$, $H[z]$ and the yet to be defined $G[z]$ and *online* using a software implementation of the control system with the real hardware, i.e. FLUTE and the controllable attenuator.

5.3.1 Choosing a Controller Type

The plant has been identified using a linear model in section 5.1 resulting in the LTI system $P(s)$ (or $P[z]$). The matching controller does not necessarily have to be a LTI system, but choosing a LTI system simplifies design and analysis and is a justifiable choice here, as there are no good reasons against it, yet.

The class of LTI controllers is dominated by the PID controller and its variants. PID stands for “proportional”, “integral” and “derivative”, which are LTI systems themselves, performing scaling, integration or differentiation. Depending on the application, variants, such as the PI controller, or the PD controller are used as well.

According to [37, p. 111] PID control is applicable for plants with order two or less. Compared to other types of controllers, using a PID controller has many advantages. It is quick to design and does not depend on an accurate plant model. Also after the designing step, the few free parameters can easily be presented to an operator and online fine tuning is possible.³

In the next section such a PID controller is designed. As it is to be implemented in software later, the design is done in discrete time.

5.3.2 Designing a Discrete Time PID Controller

The output signal $u(t)$ of a generic time continuous PID controller (see Figure 5.7) consists of the weighted sum of three error signals.

The first is simply the controller input error signal $e(t)$ scaled by the gain k_p . This is the proportional part of the PID controller. The integral part is calculated by computing the

³In contrast a compensating controller is based on an accurate model of the plant and changes on the fly are difficult.[38]

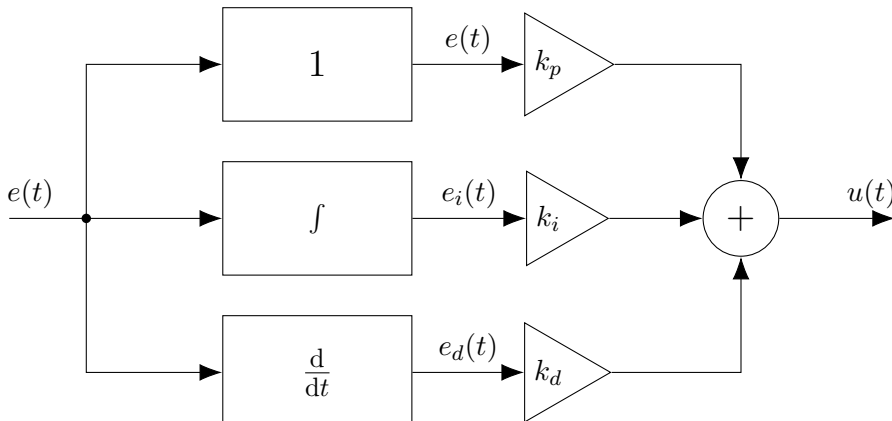


Figure 5.7: Block diagram of a generic PID controller

running time integral

$$e_i(t) = \int_0^t e(\tau) d\tau. \quad (5.10)$$

This is then scaled by the constant k_i . To get the derivative part, the derivative

$$e_d(t) = \frac{d}{dt} e(t) \quad (5.11)$$

is calculated and weighted with k_d . All three are then summed to get $u(t)$ in the so called parallel form[39, p. 5]:

$$u(t) = k_p e(t) + k_i \int_0^t e(\tau) d\tau + k_d \frac{d}{dt} e(t) \quad (5.12)$$

Often instead of the parallel form, the PID controller is stated in *standard form*. Instead of using the gains $k_{p,i,d}$, the parameters proportional gain K , integral time T_i and derivative time T_d are used.[37, p. 76] With the conversions

$$K = k_i \quad (5.13)$$

$$T_i = \frac{k_p}{k_i} = \frac{K}{k_i} \quad (5.14)$$

$$T_d = \frac{k_d}{k_p} = \frac{k_d}{K} \quad (5.15)$$

the PID controller in standard form is

$$u(t) = K \left[e(t) + \frac{1}{T_i} \int_0^t e(\tau) d\tau + T_d \frac{d}{dt} e(t) \right]. \quad (5.16)$$

The transfer function $G(s)$ is given by the Laplace of $u(t)$ using the computation rules[40]

$$\mathcal{L} \left\{ \int_0^t y(\tau) d\tau \right\} = \frac{1}{s} Y(s) \quad (5.17)$$

$$\mathcal{L} \left\{ \frac{d}{dt} y(t) \right\} = sY(s) \quad (5.18)$$

as

$$G(s) = K \left[1 + \frac{1}{sT_i} + sT_d \right]. \quad (5.19)$$

To get the discrete transfer function, either the Laplace transform $G(s) = U(s)/E(s)$, is discretized or the \mathcal{Z} transform of $u[n]$ is calculated. First, to get $u[n]$, the derivative in Equation 5.11 is approximated by

$$e_d[n] = \frac{e[n] - e[n-1]}{T_s}. \quad (5.20)$$

This assumes $e(t)$ is sampled with a sampling rate of $f_s = 1/T_s$ to get $e[n]$. In a similar fashion, the integral in Equation 5.10 is approximated by

$$e_i[n] = e_i[n-1] + e[n]T_s. \quad (5.21)$$

Using the shift rule of the \mathcal{Z} transform[40]

$$y[n-k] \xrightarrow{\mathcal{Z}} z^{-k} Y(z), \quad (5.22)$$

the discrete transfer function of the PID controller is

$$G[z] = K \left[1 + \frac{T_s}{T_i} \frac{z}{z-1} + \frac{T_d}{T_s} \frac{z-1}{z} \right]. \quad (5.23)$$

In the time domain, this becomes

$$u[n] = k_p e[n] + k_i \left(\underbrace{e_i[n-1] + T_s e[n]}_{e_i[n]} \right) + k_d \left(\underbrace{\frac{1}{T_s} e[n] - e[n-1]}_{e_d[n]} \right) \quad (5.24)$$

5.3.2.1 Controller Tuning

Next the three free parameters $k_{p,i,d}$ or $K, T_{i,d}$ are to be chosen in such a way that the controller has optimal performance. This process is called *tuning*. Tuning of the parameters can be performed online or offline.

Online tuning is done by using the physical⁴ plant. The most popular member of this class is the Ziegler-Nichols tuning[41]. The method relies on experiments and tabulated values. The mostly used variant uses one measured step response.

Using this method at FLUTE produced mixed results. While being a very simple and fast process, the resulting controller is often unstable. This is partially due to errors when extracting the tabulated values from the noisy step response, but also the method intrinsically leads to poor stability margins.[37, p. 142] Nonetheless the Ziegler-Nichols method yields a usable starting point, if the strategy is to fine tune the controller manually by intuition and experience of the user.

As the Ziegler-Nichols method does not yield an acceptable parameter set and the method combined with fine tuning by hand takes a considerable amount of time, next tuning the parameters offline using only the plants transfer function and the measurement filter is done. The offline tuning can be done analytically or using different numerical optimization strategies. In [42] analytical methods, such as the internal model control design or the pole placement design are discussed. Both require the system's transfer function in a closed form.

Tuning by numerical optimization chooses the parameters by a simulation or measured data. Goal of the optimization is to minimize a cost function J like

$$J(\theta) = \sum_{n=0}^{\infty} e_{\theta}[n]^2 \quad (5.25)$$

with the parameter vector $\theta = [k_p, k_i, k_d]$ or $\theta = [K, T_i, T_d]$:

$$\theta_{\text{opt}} = \underset{\theta}{\operatorname{argmin}} J(\theta) \quad (5.26)$$

A convenient way to do such an optimization by simulation using the transfer function of the estimated plant is the Matlab *PID Tuner*.

Tuning the Controller with the Matlab PID Tuner

The Matlab PID Tuner accepts different kinds of system models used by the Matlab/Simulink ecosystem. It is possible to directly use estimated models, models defined via their transfer function or the zero-pole-gain representation, Simulink models or combinations of those⁵.

The manual of the PID Tuner[43] describes the expected input (see Figure 5.8). The feedback path has to have unity gain, i.e. there is no measurement filter allowed. Therefore the measurement filter is moved before the junction where the output $y[n]$ would normally be measured. Then the measurement filter $H[z]$ is combined with the plant $P[z]$ to form $Sys[z]$. For that reason $y[n]$ becomes an internal signal of $Sys[z]$. However the new system output $y'[n] = h[z] * y[n]$ is not too different from the old one, since $H[z]$ is designed to remove high frequency noise but retain the rest of $y[n]$.

The manufacturers documentation [44] does not disclose any internals of the PID Tuner nor state which optimization technique is used, but three tuning objectives are stated:

⁴“Physical” in the sense that one could touch it. (But should one?)

⁵Series connection can be established by multiplying the models transfer functions.

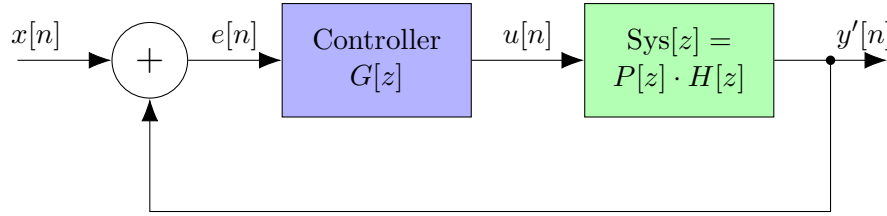


Figure 5.8: Required system architecture for the Matlab PID Tuner; PID Tuner input is the system block $Sys[z]$ (green), generated output is the controller $G[z]$ (blue)

- Stability: The closed loop should be stable (that is BIBO stable as defined in 1)
- Performance: The closed loop system tracks the input well and rejects disturbances as rapidly as possible (see subsection 2.3.1)
- Robustness: A gain and phase margin accounts for errors in the system model (see section 5.1)

Using Listing 5.3, the estimated plant $P[z]$ is loaded, a measurement filter $H[z]$ is generated and the combination $Sys[z] = P[z]H[z]$ is fed into the PID Tuner.

Listing 5.3: Matlab script to generate an input system for PID Tuner

```

1 % design lowpass measurement filter H
2 N=10;
3 lpFilt1 = designfilt('lowpassfir', 'FilterOrder', N, 'CutoffFrequency', ...
4 0.01, 'SampleRate', 0.2, 'DesignMethod', ...
5 'window', 'Window', 'kaiser');
6
7 % convert filter to a dynamic system
8 [z1,p1,k1]=zpk(lpFilt1);
9 H1=zpk(z1,p1,k1,0.2);
10
11 % load estimated transfer function and convert it to discrete form
12 load('P2ZU.mat')
13 P=c2d(idtf(P2ZU),0.2);
14
15 Sys1=tf1*H1; %Combine plant P and measurement filter H
16 pidTuner(Sys1); %Launch pidTuner
  
```

Using the PID Tuner GUI (see Figure A.2), the controller is designed by changing the design parameters **Response Time** (RT) and **Transient Behavior** (TB). Changing the response time (in seconds) influences how fast the controller acts on changes. With the transient behavior setting, the allowed over- and under-shoots, that is the deviation above and below the final value for $t \rightarrow \infty$ can be set qualitatively.

With this tool four different controllers are designed, two for each measurement filter's order of $N = 10$ and $N = 40$. The transient behavior with 0.2 for all controllers is chosen as a compromise between speed and overshoot behavior. The optimized PID parameters (for a discrete time PID controller in parallel form) are listed in Table 5.2.

Table 5.2: Parameters of a discrete time PID controller in parallel form calculated with the Matlab PID Tuner; N is the order of the used measurement filter

Name	N	RT (in s)	TB	k_p	k_i	k_d
$G_1[z]$	10	5	0.2	-0.000 577	-0.000 197	-0.000 421
$G_2[z]$	10	10	0.2	-0.000 155	-0.000 111	-5.43×10^{-5}
$G_3[z]$	40	5	0.2	-0.000 559	-2.27×10^{-5}	-0.000 396
$G_4[z]$	40	10	0.2	-0.000 35	-9.68×10^{-5}	-0.000 316

5.3.3 Analyzing the Input Tracking and Disturbance Rejection

The PID Tuner defaults to show the input tracking step response (as in Figure A.2). The input tracking is calculated based on Equation 2.34. To calculate it, the Matlab function `step()` is used, which generates the step response plot of a dynamic system, in this case F_T . As the whole system only consists of linear building blocks, using an arbitrary step height of 1 is possible. The response is then normalized in such a way that the final value is also 1.

In Figure 5.9 and Figure 5.10 the input tracking step responses for all four controllers are plotted. Note the different t scales. As expected, for longer measurement filters, i.e. filters of higher orders, the controller has to act less aggressive. This causes longer settling times. Especially Figure 5.10 shows that setting a shorter response time does not automatically cause the controller to set the output faster to its final value. While for the shorter response time, the set value is reached quicker, there is also a strong oscillation, so choosing the longer response time (see $G_4[z]$) can be beneficial.

As the set-point for FLUTE only changes occasionally, basically a fixed set-point controller is needed. Therefore the disturbance rejection is more important than the input tracking when analyzing the controllers performance. The step responses of the disturbance rejection F_{DR} are calculated in a similar way as the input tracking, using Equation 2.37 and `step()`. The y axes are normalized so that the initial value is 1 and the final value for $t \rightarrow \infty$ is 0.

In Figure 5.11 and Figure 5.12 the results for all controllers in Table 5.2 are plotted.

This shows that even for an optimistically low measurement filter order of $N = 10$, the settling time is in the order of slightly under a minute. This is sufficient for the application, but has more of a practical drawback: when fine-tuning the PID parameters manually on the machine, it is necessary to wait a few minutes after setting new parameters before assessing the change.

Especially when looking at the plots of $G_3[z]$, it is obvious that there can be stability issues when using a too aggressive controller. For that reason in the next section the stability of the four controllers is analyzed.

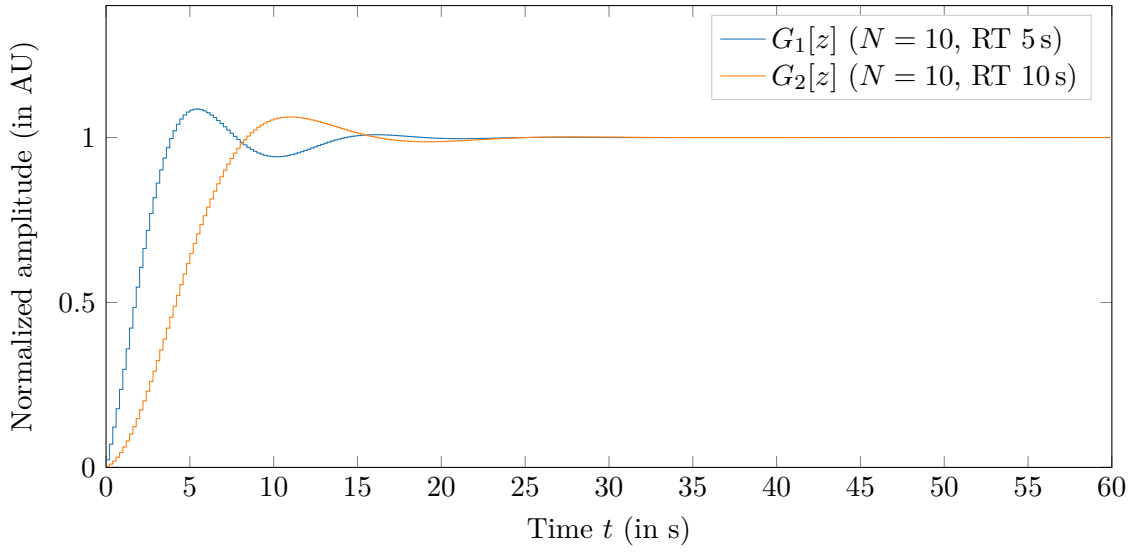


Figure 5.9: Step response of the input tracking F_T for controller $G_1[z]$ and $G_2[z]$, designed with the plant $P[z]$ and a measurement filter of order $N = 10$, response time goal to 5 s and 10 s

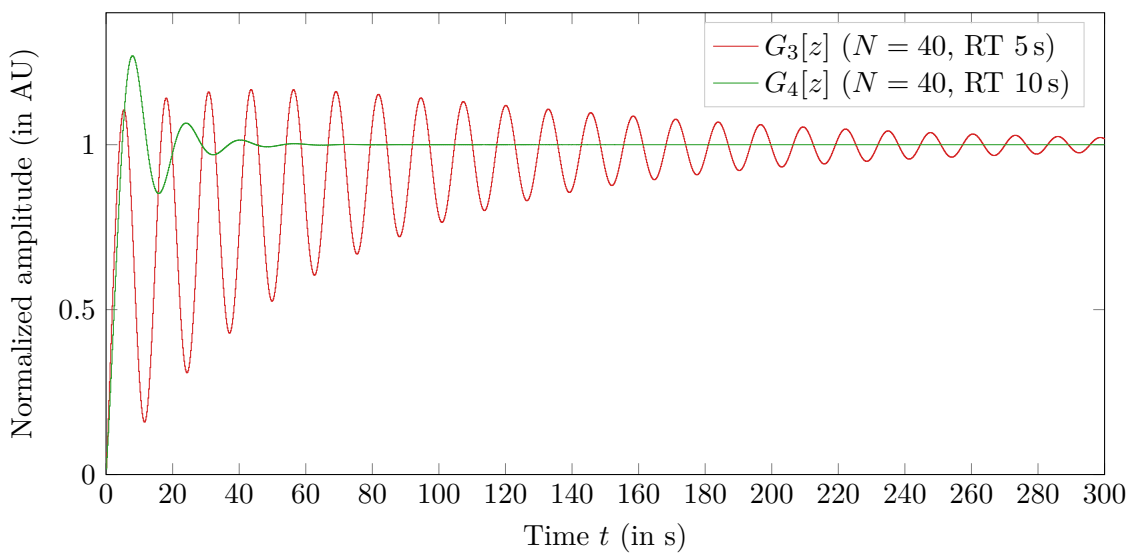


Figure 5.10: Step response of the input tracking F_T for controller $G_3[z]$ and $G_4[z]$, designed with the plant $P[z]$ and a measurement filter of order $N = 40$, response time goal to 5 s and 10 s

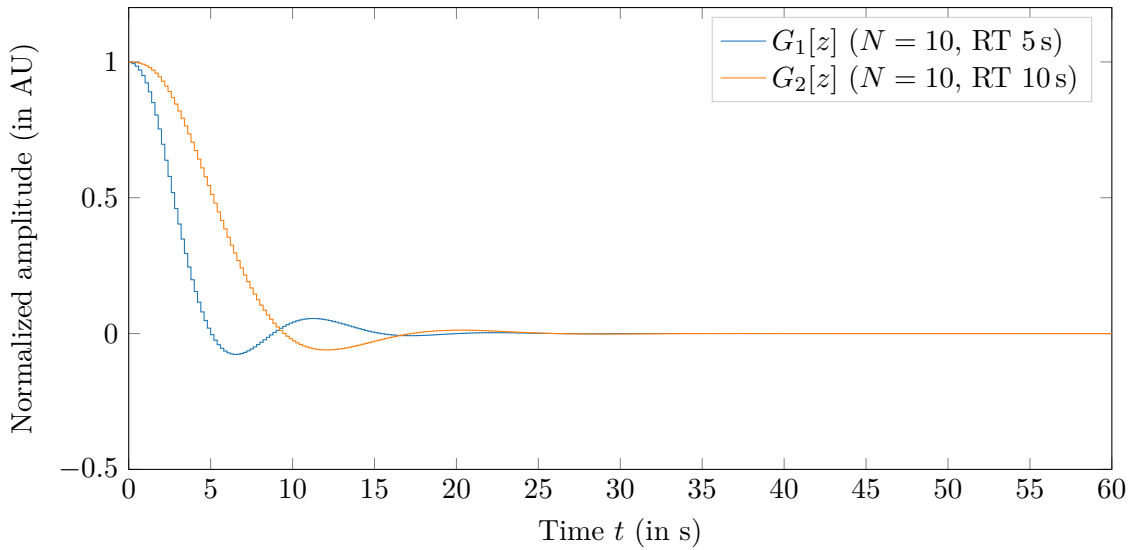


Figure 5.11: Step response of the disturbance rejection F_{DR} for controller $G_1[z]$ and $G_2[z]$, designed with the plant $P[z]$ and a measurement filter of order $N = 10$, response time goal to 5 s and 10 s

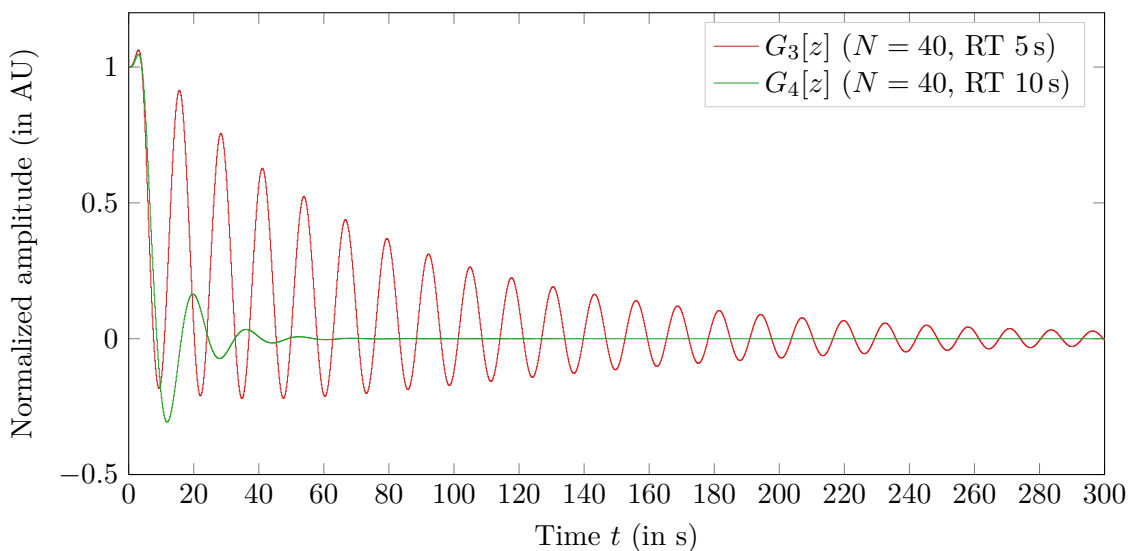


Figure 5.12: Step response of the disturbance rejection F_{DR} for controller $G_3[z]$ and $G_4[z]$, designed with the plant $P[z]$ and a measurement filter of order $N = 40$, response time goal to 5 s and 10 s

5.3.4 Analyzing the Stability

In this section the stability of the controllers $G_i[z]$ from the last section is evaluated.

For that the Nyquist criterion according to 2 is used. With the Matlab function `nyquist()`, the locus $w = F_o[w = j2\pi f]$ of the open loops

$$F_o[z] = G[z]P[z]H[z] \quad (5.27)$$

are calculated. For all controllers designed, they are plotted in Figure 5.13.

This shows the gain margin for $G_3[z]$ (in combination with the $N = 40$ filter), that is the distance to the critical point $w = (-1, 0j)$, is already very small. So in addition to its oscillatory behavior and the longer settling time, there is also the risk that the system can become unstable if there are even small system parameter changes.

In Figure 5.14 another issue is highlighted. If a controller is designed with a certain measurement filter order $N = N_0$ in mind, but is used together with a filter of order $N = N_1 > N_0$, it is very likely the closed loop system becomes unstable. In the figure the controller $G_1[z]$ is used together with the $N = 40$ filter. Both the disturbance rejection and the Nyquist plot show the closed loop to be unstable.

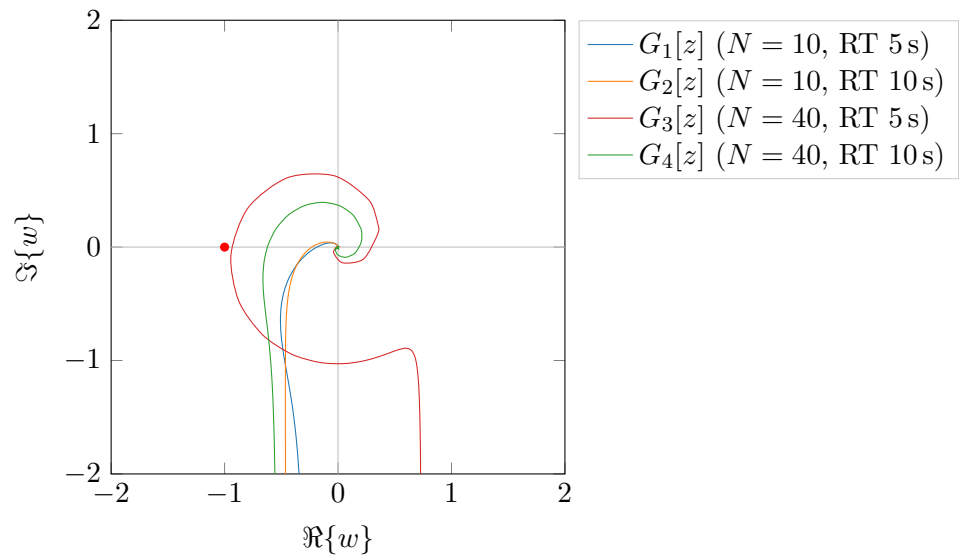


Figure 5.13: Nyquist plot to analyze the stability of the closed-loop control system based on the locus plot of the open-loop system; Note the critical point $(-1, 0j)$ is always on “left” of the curve indicating stability

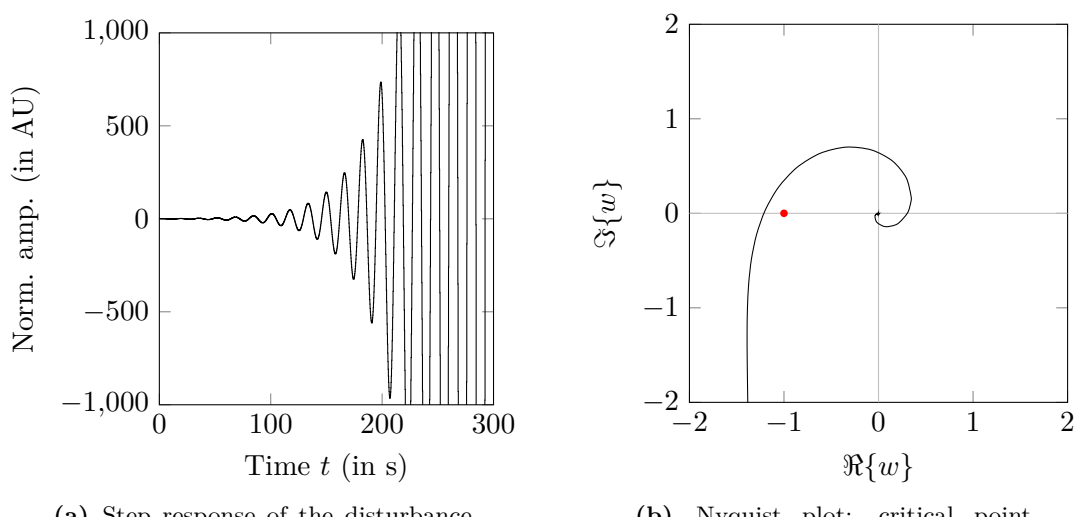


Figure 5.14: Two signs of an unstable closed loop system, in this case caused by a measurement filter with too high order and/or a too aggressive controller

5.3.5 Offline Evaluation with Measured Data

Now the performance of the controller $G_1[z]$ together with the filter order $N = 10$ should be evaluated with measured data before testing it with FLUTE. This simulation is called offline evaluation.

Offline evaluation of the control system is potentially less accurate due to an incomplete or erroneous model. But on the upside it requires no access to FLUTE and no potential downtime of the machine. Also with modern computers the simulation time advances much faster than real-time. Another big advantage is repeatability. With a pre-recorded data-set as the disturbance input, simulations are consistent and do not depend on a changing environment or system parameters.

The offline evaluation is done with Simulink, a block diagram development and simulation environment based on Matlab. The Simulink model (see Figure A.3) uses the disturbance

$$d[n] = \Delta P_{\text{cavity}}[n] = P_{\text{cavity}}[n] - \mu P_{\text{cavity}} \quad (5.28)$$

with μP_{cavity} being the time average of $P_{\text{cavity}}[n]$ over one hour. $P_{\text{cavity}}[n]$ is re-sampled to $T_s = 0.2\text{s}$. With this calculation of $d[n]$, it is assumed that the disturbance is the deviation of the cavity power from a (theoretical) set-point of μP_{cavity} .

With the simulation the effect of adding $d[n]$ to a system without any feedback and a system with the controller $G_1[z]$ and the measurement filter is compared. The result is shown in Figure 5.15

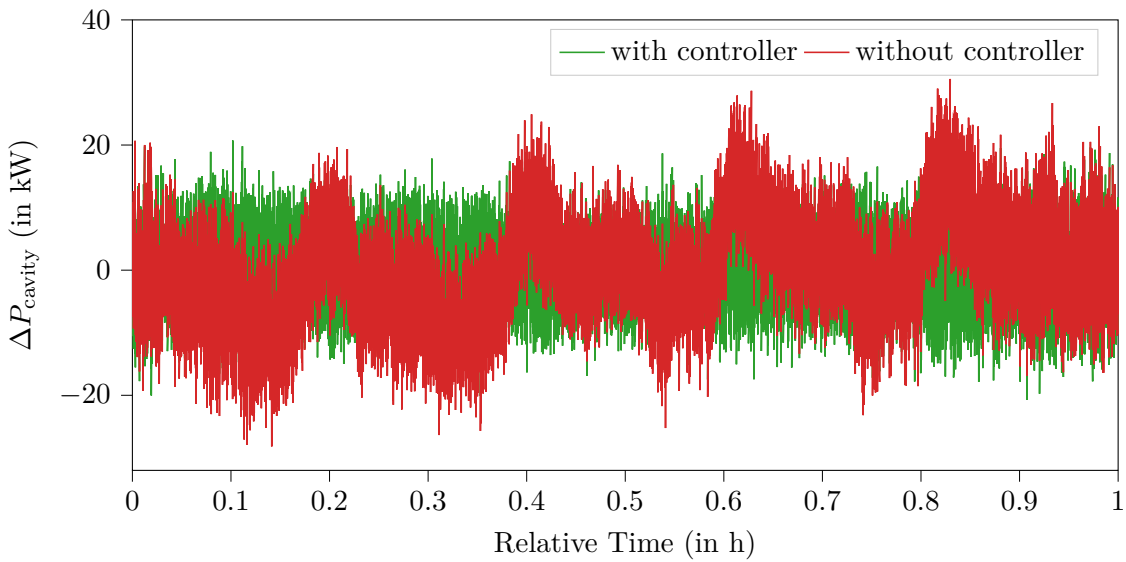


Figure 5.15: Output of the Simulink model in Figure A.3; step size $T = 0.2$ s, end time 3600 s. Simulation time on a computer equipped with an Intel i7-3770: 3.5 s

5.4 Implementation of the Control System in Software

In this section the findings from the beginning of this chapter are used to implement a time discrete control system, that is a time discrete PID controller that is used to drive the controllable attenuator based on filtered measurements from the system.

The system should be implemented as software that runs on most personal computers and requires few external dependencies to make it as portable as possible. The other core requirements can be summarized to be:

- Communicate with EPICS (over an Ethernet connection) to read in data such as $P_{\text{cavity}}[n]$
- Provide means to filter the incoming data with a measurement filter $H[z]$ with variable order N and cutoff frequency f_c
- Calculate the control error $e[n]$ and based on that the controller output $u'[n]$. Then convert the controller output, an attenuation, to the matching control voltage V_{control}
- Communicate with the Keysight 34972A over VXI-11 (over an Ethernet Network) to set the control voltage $V_{\text{control}}[n]$ of the attenuator
- The control routine of the program needs to be light-weight enough so a scheduler can call it faster than five times a second to achieve a sampling time of 0.2 s
- Show the input, the output and the error signals to the user on a GUI
- Provide graphical input elements to let the user modify the measurement filter and the controller parameters (k_p , k_i , k_d)
- Log the input, output and parameters to disk for later reference

Since many other choices depend on it, first the programming language has to be picked. As Python was used in earlier chapters and the communicating abilities to both EPICS and the Keysight 34972A were already proven, it is the obvious choice.

From there on the GUI framework is the next decision to be made. For Python popular choices are *Tkinter*, a built in implementation of the Tk/tcl GUI toolkit, *wxPython*, a Python binding to the cross-platform GUI library wxWidgets, or *PyQt*[45], a set of Python

bindings for the Qt GUI framework[46]. While Tkinter has the advantage of being built into the Python language, wxPython offers more functionality and is more widely adopted. PyQt profits from the large Qt ecosystem, so is it for example possible to develop the GUI separately from the code using *Qt Designer*.

For (live-) plotting of data in the GUI, the standard library in Python is *matplotlib*[47]. It can be used with all three plotting libraries. However the biggest drawback is the possible update speed of the plots. With more than about a hundred points on the screen, the update frequency drops to well below 1 Hz. A much faster alternative is *pyqtgraph*[48], a scientific plotting library written in Python and using the Qt GraphicsView. It is only compatible only with PyQt (or the PySide alternatives).

Therefore PyQt and pyqtgraph are used to build handle the GUI and plot the live data. Also Qt Designer is used to model the GUI graphically.

The control algorithm is implemented by directly using the equations derived in subsection 5.3.2. The time domain representation of the PID controller is (restated from Equation 5.24)

$$u[n] = k_p e[n] + k_i \left(\underbrace{e_i[n-1] + T_s e[n]}_{e_i[n]} \right) + k_d \left(\underbrace{\frac{1}{T_s} e[n] - e[n-1]}_{e_d[n]} \right) \quad (5.29)$$

When translating Equation 5.29 to code, the recursion ($e_i[n]$ depending on $e_i[n-1]$) is solved by introducing a variable that keeps track of $e_i[n]$ over time. The last value of $e[n]$, $e[n-1]$ is kept in memory for the derivative part. An example in pseudo code is listed in Listing 5.4.

Listing 5.4: PID controller implemented in pseudo code

```

1 while(true) {
2     e      := x_set - x_actual
3     e_i    := e_i.old + e*T_s
4     e_d    := (e-e.old)/T_s
5     e_i.old := e_i
6     e.old   := e
7     wait_sec(0.2)
8 }
```

To get the timing right and to allow the GUI to be responsive while the control algorithm runs in the background, a scheduler that activates a callback function every 0.2 s should be used. Since in section 4.2 the Advanced Python Scheduler (AP scheduler) is used successfully, it should also be used for the control system. Unfortunately the AP scheduler is not compatible with PyQt and using it interferes with the internal Qt timing systems. For this reason, a timer is constructed instead with the `QTimer` class.[49]

Logging the data to disk is done by using the same `QTimer`, as is used for the control algorithm, to write one line of CSV data to disk each time the timer is triggered.

With these building blocks ready, the GUI is build with Qt Designer and based on the `.ui` file generated from Qt Designer the GUI Application is implemented. For a screenshot of the program running see Figure A.4.

5.5 Evaluation of the Control System (Online)

After evaluating the controller offline, it is now time to evaluate the performance of the control system on the machine. To do so, FLUTE is operated with and without the control system switched on for 6 h each. Before the test, FLUTE is allowed to run a few hours for all components to reach operating temperatures. The result of the test is shown in Figure 5.16. Note, that in this test about 7 h into the experiment there was an unexpected shutdown of FLUTE and the corresponding block of data is removed before further processing.

The time plot Figure 5.16 and also the spectrogram in Figure 5.17 show the cavity RF power approximately reaches stationarity in the [0, 6] hour interval respectively in the [6, 12] hour interval. This allows the spectrum for these two blocks to be estimated using a periodogram method. In Figure 5.19 the spectra for each case are shown. The corresponding time data is plotted in Figure 5.18

With the periodogram data, the control system success can be measured with the most prominent noise metric.

Next, the cases controller on and controller off should be compared with the relative standard deviation. Measuring and displaying the relative standard deviation $STD\%$ is also supported on the LLRF CSS panel at FLUTE, so while the experiments run, the values are checked from time to time. It can be observed that different values are shown over time although the plotted time signal looks stationary by eye. This suggests that the relative standard deviation does not only depend on the window size T over which it is calculated, but also heavily on the absolute position in time t . This effect is more visible for small window sizes. The issue is illustrated in Figure 5.20, where $STD\% = STD\%(t, T)$ is plotted as a function of the time t and the window size T .

For that reason, for small window sizes, time averages of $STD\%$ should be used instead of single values. For the measured $STD\%(t, T)$ for the controller off and the controller on cases, $STD\%(T)$ is plotted in Figure 5.21. This plot shows what could already be guessed from Figure 5.20: with the $STD\%$ metric, the system seems *less* stable with the controller on, if the $STD\%$ is calculated over small window sizes e.g. $T = 1$ min. For very long windows, the dependency on the window position becomes very small. So for the comparison with the other metrics, $STD\%(T = 4$ h) is used.

With the metrics from section 2.4, the success of the control system is assessed in Table 5.3. This shows for example the mean squared error is improved by a factor of about 371 by using the control system.

Table 5.3: Quantitative assessment of the controllers performance

Metric	Controller off	Controller on	Controller off/Controller on
$\%STD(4\text{ h})$	0.001 155 9	$5.992\ 25 \times 10^{-5}$	9.2891
MSE	37.639	0.101 33	371.44
MPN	487 309.29	14 386.25	33.873

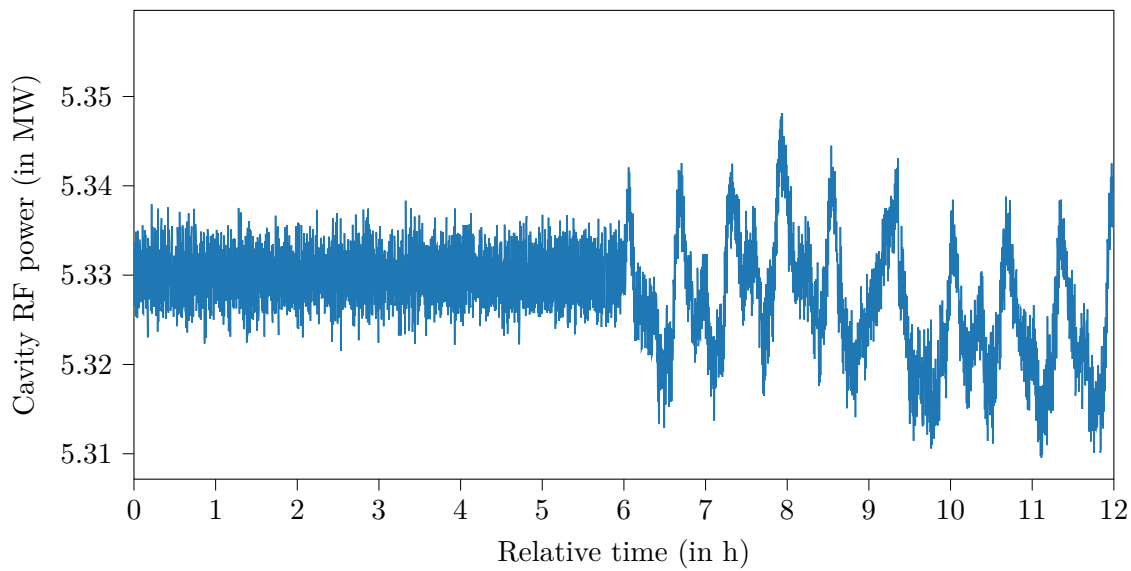


Figure 5.16: Cavity power over about 15 h (about three hours of downtime removed for clarity around the 7 h mark); control system switched off at 6 h (recording started 2021/05/01 20:00)

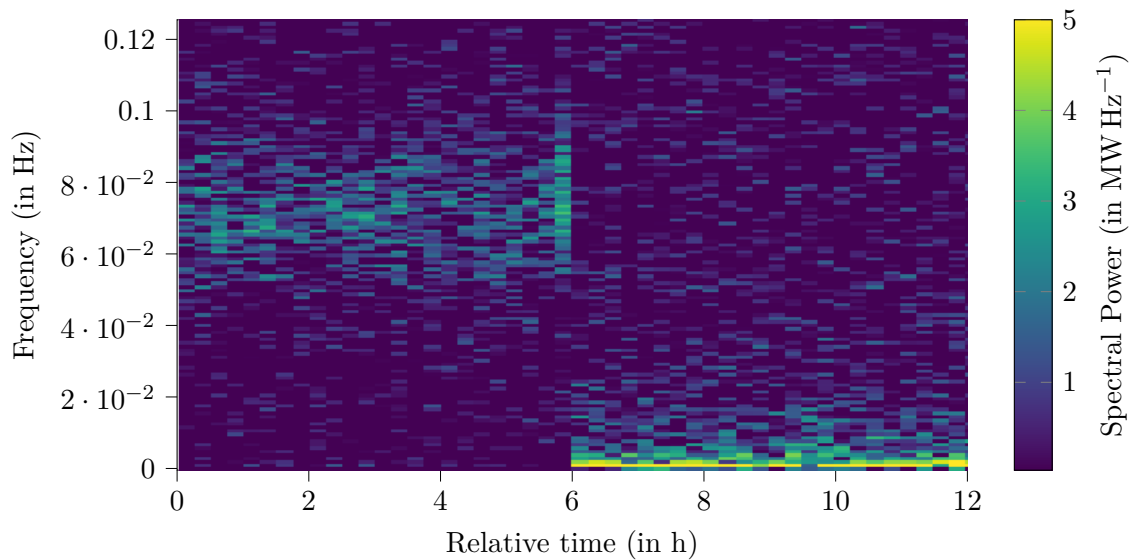


Figure 5.17: Spectrogram of the cavity power in Figure 5.16

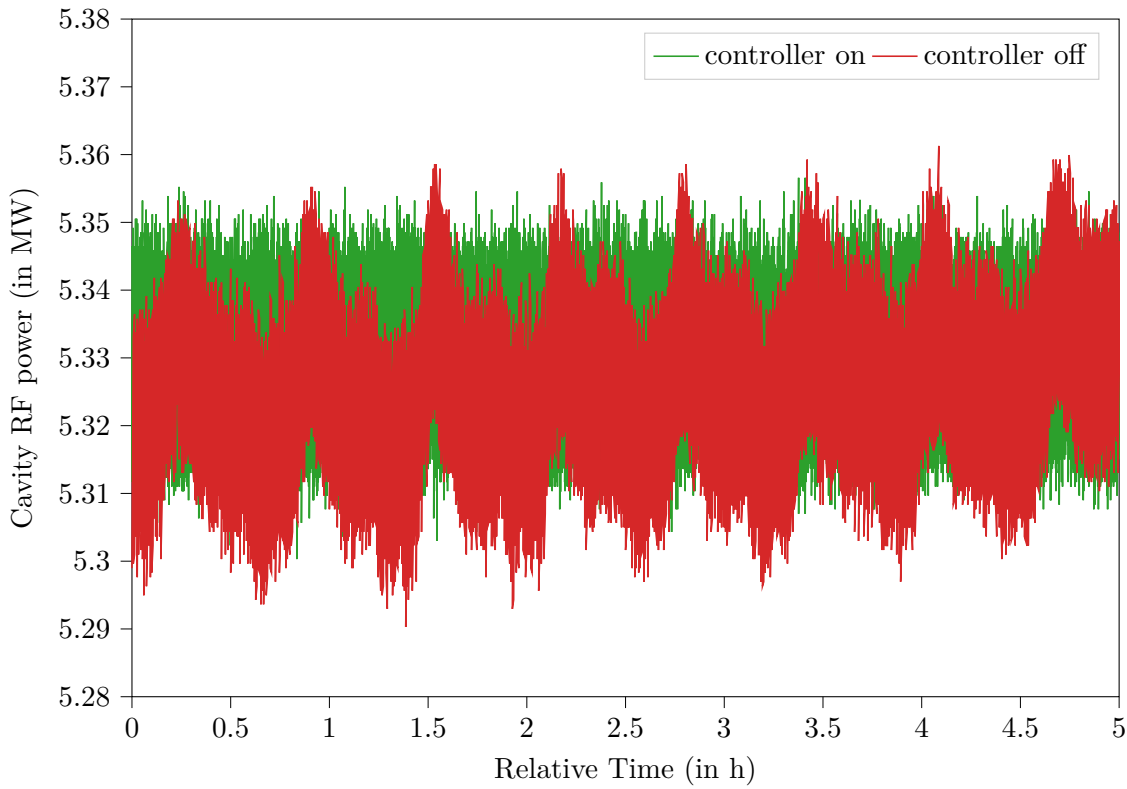


Figure 5.18: Time plots comparing between the control system on and off

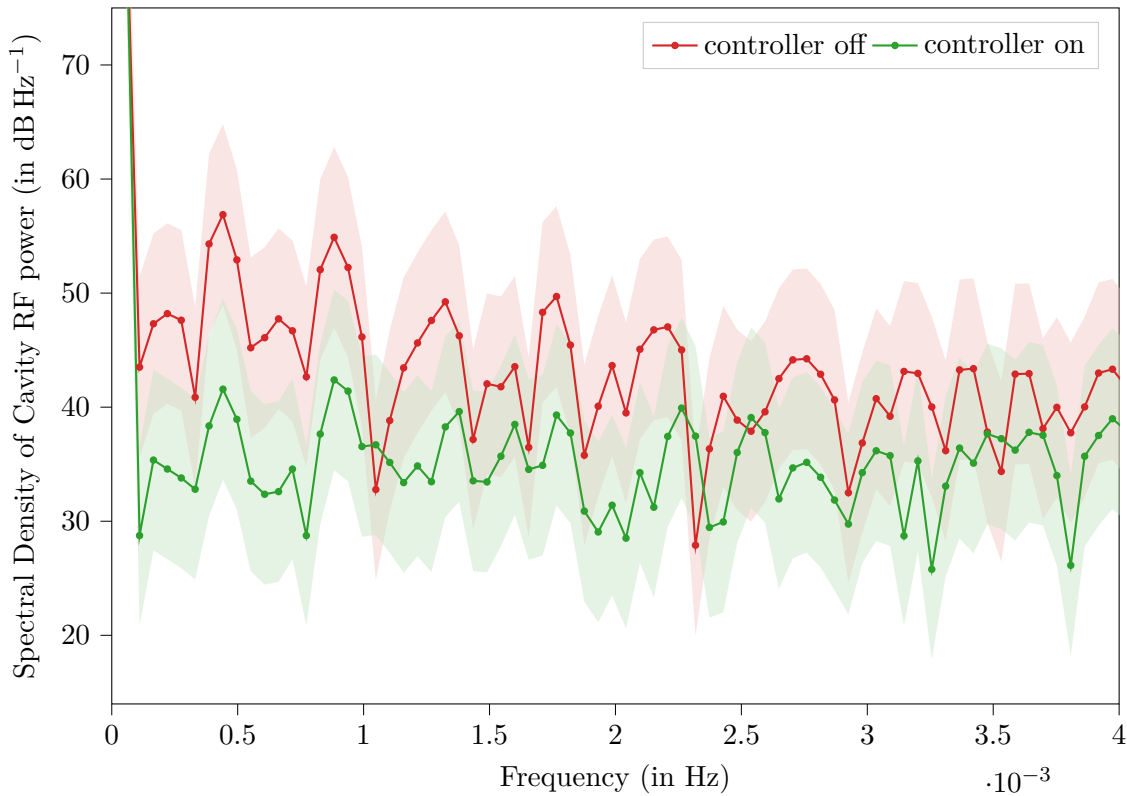


Figure 5.19: Power spectrum of the plots in Figure 5.16 computed with Welch's method; shaded areas show the uncertainty according to Equation 2.31

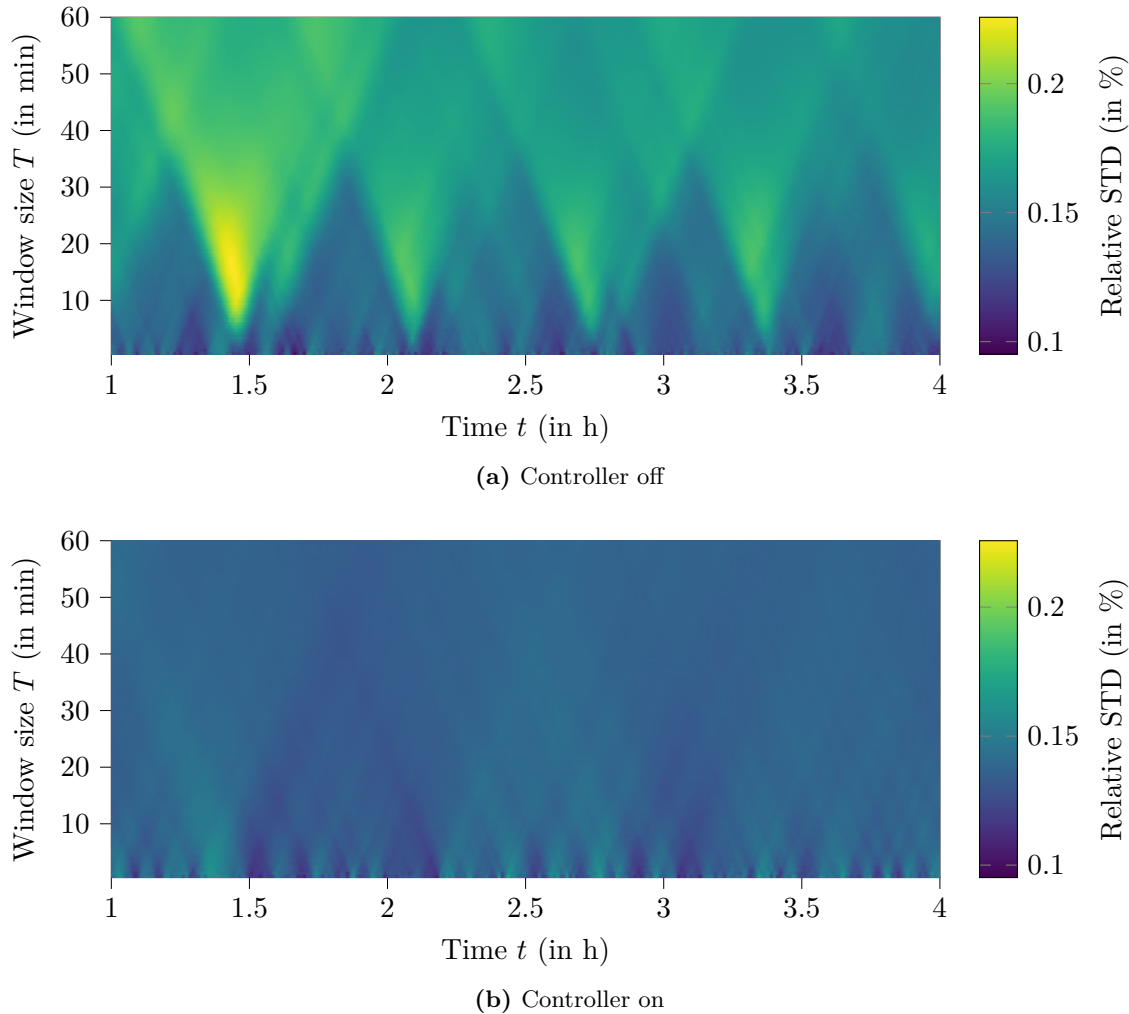


Figure 5.20: Relative standard deviation $STD\%(t, T)$

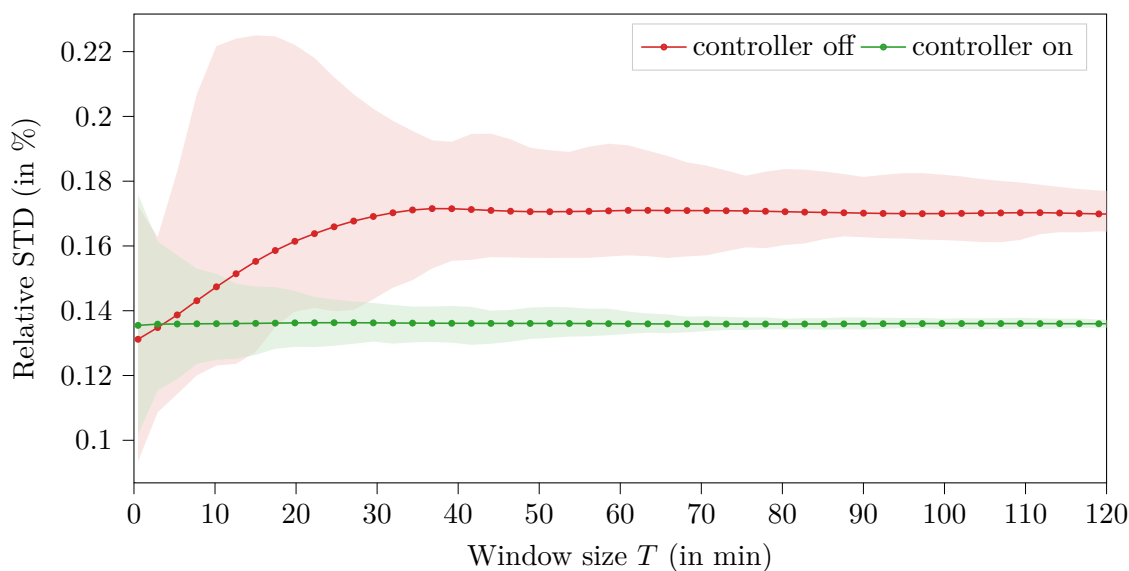


Figure 5.21: Relative standard deviation $STD\%(T)$, shaded areas show $\min\{STD\%(t, T_0)\}$ and $\max\{STD\%(t, T_0)\}$, solid lines show $\text{mean}\{STD\%(t, T_0)\}$ for a fixed window size $T = T_0$

5.6 Further Improvements to the Control System

In this section, two methods for improving the control system's performance are examined. First the closed-feedback loop is supplemented with an additional input for one disturbance source, the gun's body temperature. A different approach tested is switching from the gun cavity RF power to the electron charge, as measured by the Faraday cup at the end of the low-energy section, as the controlled signal.

5.6.1 Changing the Controller Architecture: Disturbance Feed-Forward of the Gun Temperature

Instead of changing only the parameter of the PID controller or switching to another type of controller, the strategy presented here relies on changing the architecture over the standard form (see Figure 2.1) to include a feed-forward path⁶.

To use the disturbance $d(t)$ ($|d(t)| < \infty$) explicitly in the control system, it has to be measurable separately from the control system's output $y(t)$. This can practically only be done if either all disturbance sources or the dominant ones can be identified and measured with some physical sensor. If the signal $d(t)$ is obtainable, it can be fed into the signal path near the controller. In the literature, two locations for the disturbance signal to be injected to are described. The method used decides, among other things, which (if any) filtering of $d(t)$ has to be done.

One technique is to regard the disturbance to be similar to the error signal $e(t)$, i.e. the controller input. [50] In this case, the pre-processing, in general, has to include a scaling operation, because the units and magnitudes of $e(t)$ and $d(t)$ are different. If $d(t)$ has non-zero mean, it needs to be subtracted to achieve linear behavior. This means, the needed disturbance filter is

$$D_1(s) = k_{\text{disturbance},1} D'(s), \quad \text{with } D'(s) = \mathcal{L} \left\{ d(t) - \mu_{d(t)} \right\}. \quad (5.30)$$

The second method is to add the filtered disturbance signal to the controller output. [14], [51] In general, this also requires the same pre-processing as before,

$$D_2(s) = k_{\text{disturbance},2} D'(s), \quad \text{with } D'(s) = \mathcal{L} \left\{ d(t) - \mu_{d(t)} \right\}, \quad (5.31)$$

but with a different scaling factor $k_{\text{disturbance},2} \neq k_{\text{disturbance},1}$. This method has the advantage of being potentially faster, because the controller does not occur in the signal path for the disturbance feed-forward, so its dynamics add no additional delay to $d_2(t)$.

In both cases it is common to add another filter to $D_{1,2}$. This is often a lowpass filter $H_d()$ to remove noise. The disturbance filter than becomes

$$D(s) = k_{\text{disturbance}} \cdot H_d(s). \quad (5.32)$$

The new controller architecture is shown in Figure 5.22. Drawn there is the plant $P(s)$ being split into $P_1(s)$ and $P_2(s)$. This is neither necessary nor possible under all circumstances but feeding forward the disturbance that acts earlier on the plant would lessen the delay of $d(t)$ ⁷. Besides its main purpose of quickly reacting to a disturbance change, the feed-forward also has the inherent benefit of having no influence of the systems stability. Since $d(t)$ is assumed to be finite, the output has to react to $d(t)$ also with a finite response, as the filtered $d(t)$ is only added to $y(t)$.

–Todo: Results and plots–

⁶The calculations here are done in continuous time to be comparable with the control system model in section 2.3

⁷A disturbance that acts on the middle of the plant is different from the one that acts on the end.

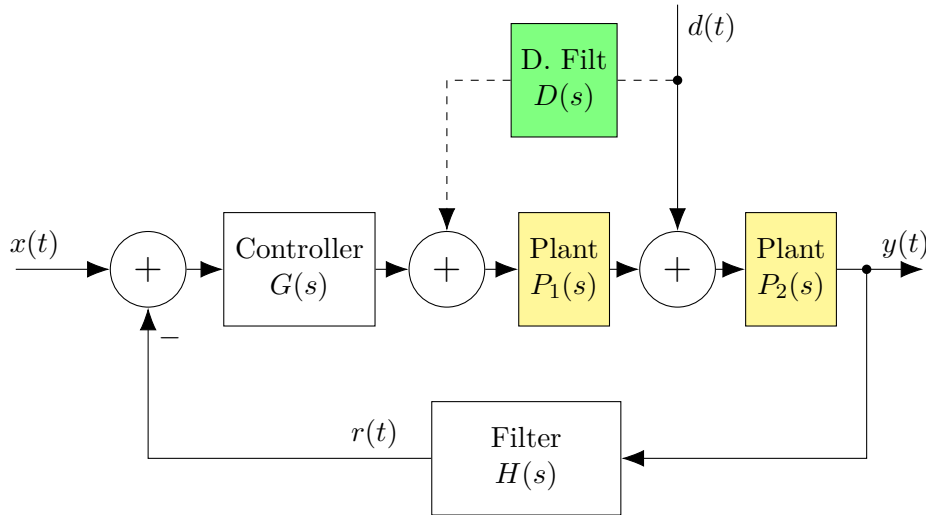


Figure 5.22: Schematic for a control system that uses disturbance feed-forward of the measurable disturbance $d(t)$ in addition to the feed-back loop; changes to the classical control system architecture in Figure 2.1 highlighted in yellow(changed) and green(added) (based on [14, p. 221])

5.6.2 Feed-Back on Faraday-Cup Measurements

With the relation

$$P_B = \frac{I \Delta W}{q}, \quad (5.33)$$

the power the cavity transfers to the beam P_B is related to the current of the beam I and the energy gain ΔW . [7, p. 43]

The Faraday cup mounted at the end of the low energy section together with the Charge Sensitive Amplifier (CSA) measures the integrated beam current. The CSA is reset with every new pulse, so it measures

$$Q_{FC} = \int_0^{T_{pulse}} I(t) dt = \int_0^{4.5 \mu s} I(t) dt. \quad (5.34)$$

The Faraday cup does not discriminate between the origin nor the location in time of the electron beam in the $[0, T_{pulse}]$ interval. In particular that means it is sensitive to the dark current emitted with the RF supply switched on, but without any laser pulses. This is different from the the measurements of the Integrating Current Transformer (ICT) and the charge output of one of the Beam Position Monitors (BPMs). [16]

The advantage of using Q_{FC} over the RF power P_{cavity} is that the measurement of the charge relates more closely to the electron energies.

Because the Faraday cup measures dark current, the control system, with Q_{FC} as an input, can be tested with the laser off, the same as is was with the cavity power.

Figure 5.23 and Figure 5.24 show the cavity power and the (uncalibrated) charge reading of the Faraday cup for three different cases: the control system switched off, the control system on with the cavity power used as control input and the control system with the Faraday cup's readout (via the CSA) as an input.

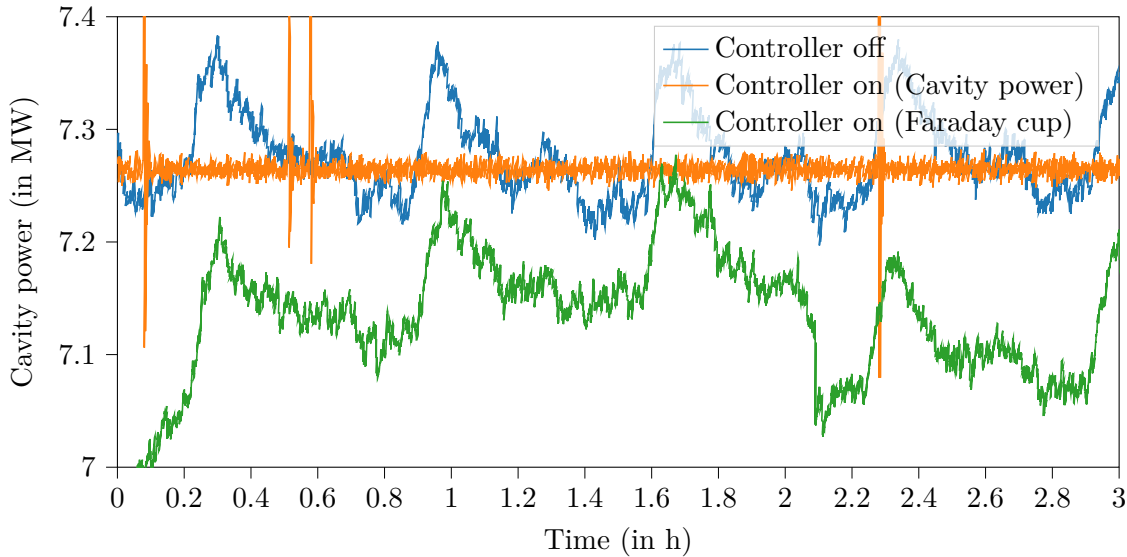


Figure 5.23: Cavity power without control interaction, with the controller acting on the cavity power and with the controller acting on charge; Note the three curves are measured at different times and have no relation to one another

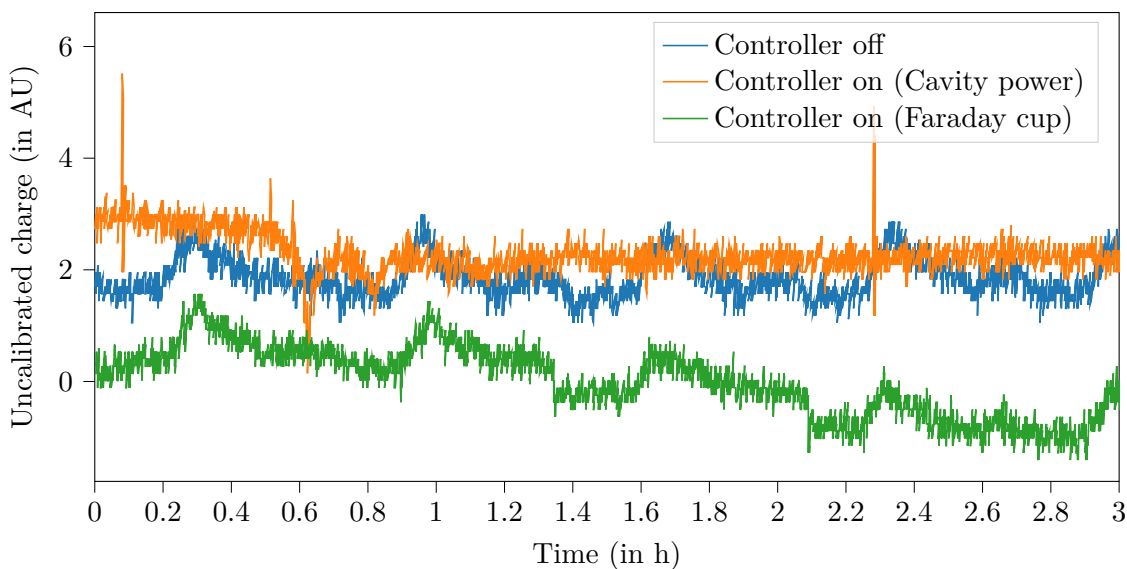


Figure 5.24: Electron charge without control interaction, with the controller acting on the cavity power and with the controller acting on charge; Note the three curves are measured at different times and have no relation to one another

6. Summary and Outlook

For the operational phase of FLUTE, a stable electron generation will be vital to perform scientific experiments. But also in its current commissioning phase, having a stable electron gun is highly desired. Not only for setting up the beam diagnostic devices, but also for intermediate- and pre-experiments and the comissioning phase of the LINAC section a reliable low energy section is expected.

At the start of the thesis, the stability of the gun was unsatisfactory. As the main source of the instability, the cooling system of the electron gun's body could be identified. But there are other systems and effects that negatively influence the electron generation. These still have not been fully identified and understood, yet.

However this thesis shows that with a control system that interacts with the low power input signal of the klystron, it is possible to improve the stability by creating a closed-loop feedback system using readouts from the EPICS control system as “sensors” and a controllable RF attenuator in the signal path as “actuator”. The system transfer function (plant) between the attenuator and the power in the electron gun cavity shows PT_2 behavior, so control with a PID controller is possible and its positive effects on the stability are shown.

However the studies here also show the limitations of a traditional LTI control system. The parameterization of the necessary measurement filter is a trade-off between stability of the controller and noise in the system, which in both cases degrades output stability.

The control system could be further optimized by switching to a totally different controller architecture. A possible choice might be model predictive control, which exploits the already identified plant transfer function but determines the output through an optimization process rather than a linear system.

Also the future of the current electron gun and RF supply is unclear. Switching to another gun and/or a different RF system could lead to an entirely different behavior of the whole system.

Appendix

A Complementary Material Controller Design

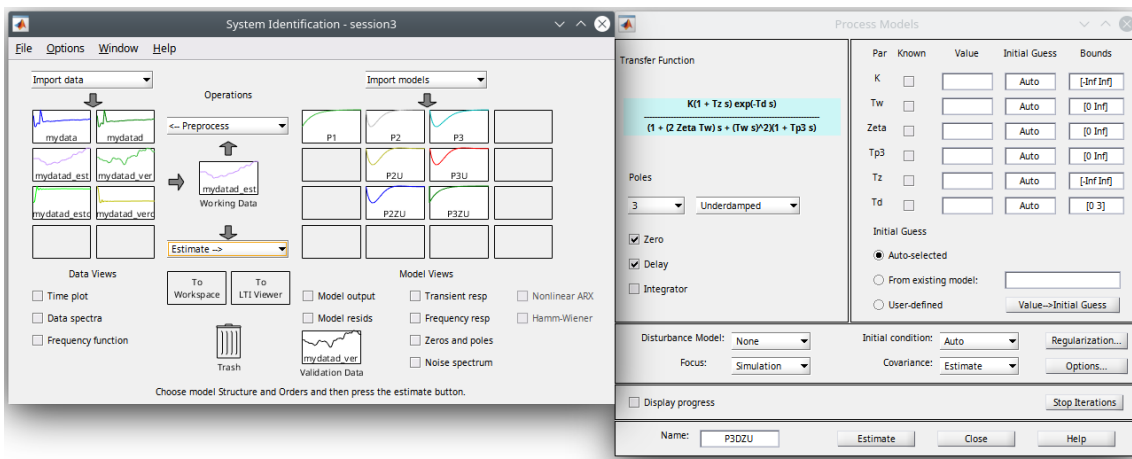


Figure A.1: Screenshot of the Matlab System Identification Toolbox; to the right the process models estimator window

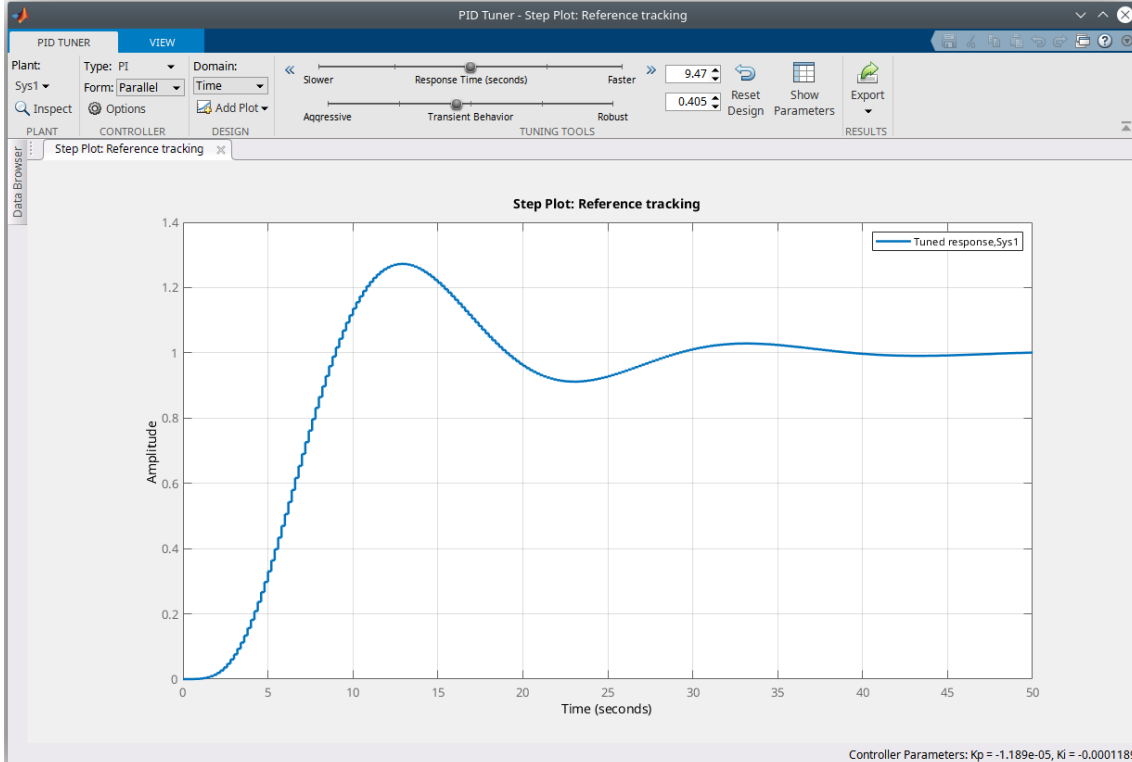


Figure A.2: Screenshot of the Matlab PID Tuner from the Control Systems Toolbox

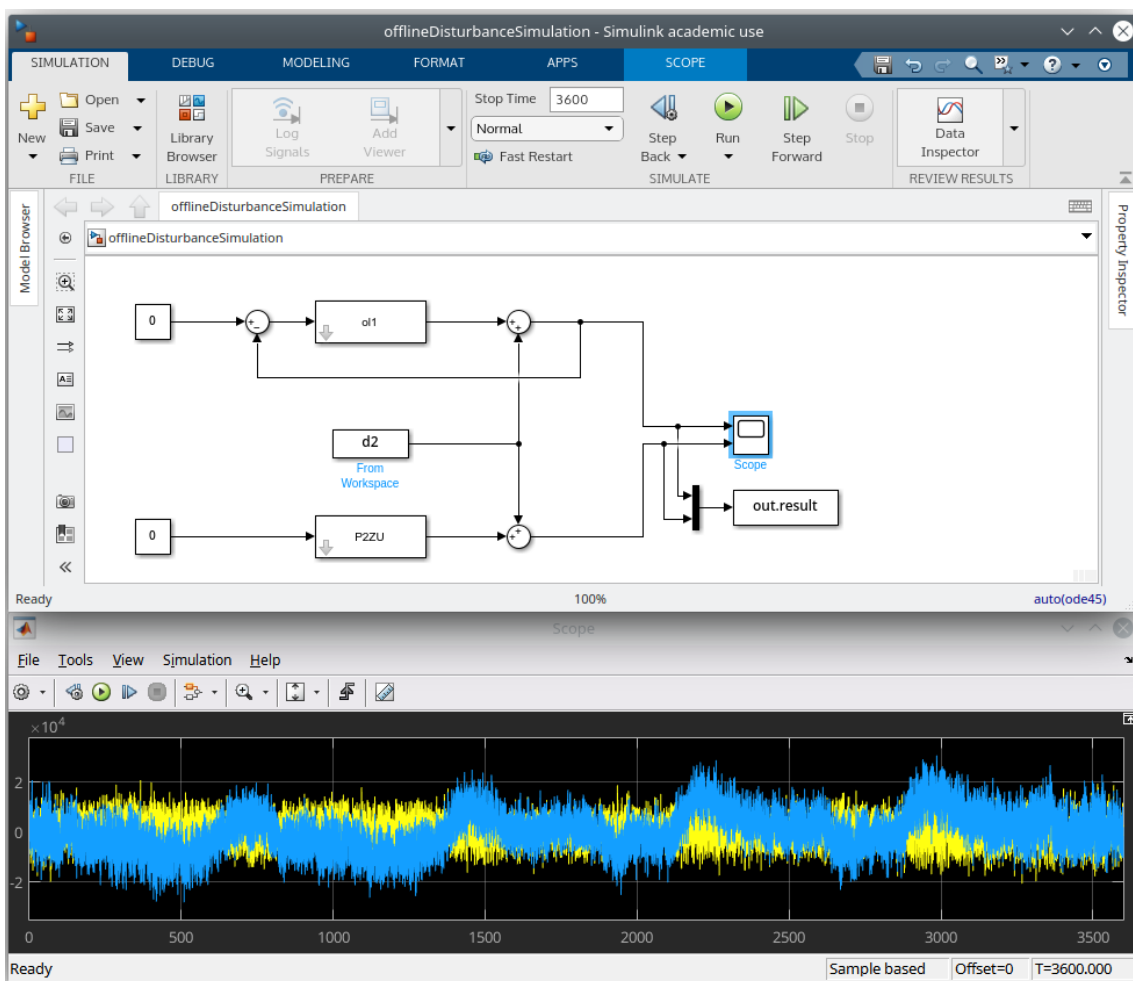


Figure A.3: Simulink model to evaluate the designed controller together with the measurement filter ($ol1$) compared to the uncontrolled system (in $P2ZU$) using measured disturbance data (in the vector $d2$); below a view of the scope data



Figure A.4: Screenshot of the control system's GUI application

B Lab Test and Measurement Equipment

B.1 Benchtop multimeters

B.1.1 Agilent 34411A

Table B.1: Agilent 34411A specifications

Specification	Value
Digits	6 1/2
Measurement method	cont integrating multi-slope IV A/D converter
Accuracy (10 V range, 24 hours)	0.0015 %+0.0004 % (% of reading + % of range)
Bandwidth	15 kHz (typ.)

Table B.2: Agilent 34411A some SCPI commands

Description	Example command	Example return
Read current measurement	READ?	+2.84829881E+00 (2.848 V)

B.1.2 Keysight 34470A

Table B.3: Keysight 34470A specifications

Specification	Value
Digits	7 1/2
Measurement method	cont integrating multi-slope IV A/D converter
Accuracy (10 V range, 24 hours)	0.0008 %+0.0002 % (% of reading + % of range)
Bandwidth (10 V range)	15 kHz (typ.)

Table B.4: Keysight 34470A some SCPI commands

Description	Example command	Example return
Read current measurement	READ?	+9.99710196E+00 (9.997 V)

B.2 Data Acquisition/Switch Unit

B.2.1 Keysight 34972A

Table B.5: Keysight 34972A specifications

Specification	Value
	34907A (Multifunction module)
DAC range	$\pm 12\text{ V}$
DAC resolution	$16\text{ bit} (2^4\text{ V}/2^{16} = 366.21\text{ }\mu\text{V per bit})$
DAC maximum current	10 mA
	34901A (20 channel multiplexer)

Table B.6: Keysight 34972A some SCPI commands

Description	Example command	Example return
Read current measurement	READ?	+2.00200000E+01 (20.02 °C)
Set DAC voltage of ch 204 to 3.1 V	SOUR:VOLT 3.1, (@204)	

B.3 RF signal generator

B.3.1 Rohde and Schwarz SMC100A

Table B.7: Rohde and Schwarz SMC100A specifications

Specification	Value
Frequency range	9 kHz to 3.2 GHz
Maximum power level	17 dBm
SSB phase noise (@ 1 GHz, $f_o = 20$ kHz, $BW = 1$ Hz)	-111 dBc
Level error	<0.9 dB

Table B.8: Rohde and Schwarz SMC100A some SCPI commands

Description	Example command	Example return
Set RF power level to 10.5 dBm	SOUR:POW 10.5	
Set RF frequency to 3.1 GHz	SOUR:FREQ:FIX 3.1e9	
Enable the RF output	OUTP on	

B.4 RF power meter

B.4.1 HP E4419B

Table B.9: HP E4419B specifications

Specification	Value
Digits	4
Accuracy (abs. without power sensor) Power probe: E4412A	±0.02 dB
Frequency range	10 MHz to 18 GHz
Power range	-70 dBm to 20 dBm

Table B.10: HP E4419B some SCPI commands

Description	Example command	Example return
Measure power on input 1	MEAS1?	+2.89435802E+000 (2.894 dBm)

B.5 Vector Network Analyzer

B.5.1 Agilent E5071C

Table B.11: Agilent E5071C specifications

Specification	Value
Frequency range	9 kHz to 8.5 GHz

B.6 Phase noise analyzer

B.6.1 Holzworth HA7062C

Table B.12: Holzworth HA7062C specifications

Specification	Value
DUT input frequency	10 MHz to 6 GHz
Measurement bandwidth	0.1 Hz to 40 MHz offsets

Acknowledgments

First I would like to thank Prof. Anke-Susanne Müller and the whole FLUTE team for providing me with the opportunity to write my thesis at their research facility. FLUTE proved to be a one-of-a-kind machine and I really appreciate the work that has been put into it.

Many thanks go also to Prof. Dr.-Ing. John Jelonnek from the Institute for Pulsed Power and Microwave Technology for taking the responsibility of being my first reviewer. Also many thanks to his PhD students Benjamin Ell and Alexander Marek for being very patient while listening to and optimizing my presentations.

I'm especially in debt to my excellent advisor Dr. Nigel John Smale, for always having the time to go over both fundamentals and nifty details of electronics and physics alike. Without his support I wouldn't even be able to switch on FLUTE by now and much less a successful thesis would've been possible.

Thanks to Igor Križnar for constructive discussions and programming the GUI panel to control the charge sensitive amplifier.

Thanks Olena Manzhura for her support and for prove-reading the thesis multiple times.

And lastly but maybe most importantly, a big thanks goes out to my family, that is my mom Sonja, Stefan and my grand-parents Ernst and Gretel, for supporting me during my whole course of studies.

Bibliography

- [1] J. Schäfer, B. Härrer, A. Papash, and A.-S. Müller, “Transfer line for ultra short bunches from FLUTE to cSTART”, 2019, 54.01.01; LK 01.
- [2] S. Naknaimueang *et al.*, “FLUTE, a Linac Based THz Source”, *Conf. Proc. C*, vol. 110904, C. Petit-Jean-Genaz, Ed., pp. 1458–1460, 2011.
- [3] A. Malygin, A. Bernhard, E. Bründermann, A. Böhm, S. Funkner, I. Križnar, S. Marsching, W. Mexner, A. Mochihashi, A.-S. Müller, M. Nasse, G. Niehues, R. Ruprecht, T. Schmelzer, M. Schuh, M. Schwarz, N. Smale, P. Wesolowski, and M. Yan, “Commissioning Status of FLUTE”, en, *Proceedings of the 9th Int. Particle Accelerator Conf.*, vol. IPAC2018, Canada, 2018. DOI: 10.18429/JACOW-IPAC2018-THPMF068.
- [4] M. J. Nasse, E. Huttel, S. Marsching, A.-S. Müller, S. Naknaimueang, and R. Rossmanith, “FLUTE: A Versatile Linac-based THz Source Generating Ultra-short Pulses”, in *Proc. 4th Int. Particle Accelerator Conf. (IPAC’13)*, (Shanghai, China), JACoW Publishing, pp. 2147–2149.
- [5] M. Yan, A. Bernhard, E. Bründermann, S. Funkner, I. Križnar, A. Malygin, S. Marsching, W. Mexner, A. Mochihashi, A.-S. Müller, M. Nasse, G. Niehues, R. Ruprecht, T. Schmelzer, M. Schuh, N. Smale, P. Wesolowski, and S. Wüstling, “FLUTE Diagnostics Integration”, en, *Proceedings of the 9th Int. Particle Accelerator Conf.*, vol. IPAC2018, Canada, 2018. DOI: 10.18429/JACOW-IPAC2018-WEPAL029.
- [6] F. Hinterberger, *Physik der Teilchenbeschleuniger und Ionenoptik mit durchgerechneten Beispielen und 99 Übungsaufgaben mit vollständigen Lösungen*. Berlin, Heidelberg, New York: Springer, 1997, ISBN: 9783540612384.
- [7] T. Wangler, *RF linear accelerators*. Weinheim: Wiley-VCH, 2008, ISBN: 9783527623426.
- [8] K. I. Park, *Fundamentals of Probability and Stochastic Processes with Applications to Communications*. Springer International Publishing, Dec. 4, 2017, 288 pp., ISBN: 3319680749.
- [9] F. Puente León, *Messtechnik*. Springer-Verlag GmbH, 2019, ISBN: 3662597667.
- [10] A. Lapidoth, *A Foundation in Digital Communication*. Cambridge University Press, Mar. 26, 2019, 920 pp., ISBN: 1107177324.
- [11] P. Stoica, *Introduction to spectral analysis*. Upper Saddle River, N.J: Prentice Hall, 1997, ISBN: 0132584190.
- [12] D. Rowell. (2008). 2.161 Signal Processing: Continuous and Discrete, Massachusetts Institute of Technology: MIT OpenCourseWare, [Online]. Available: <https://ocw.mit.edu/courses/mechanical-engineering/2-161-signal-processing-continuous-and-discrete-fall-2008/#>.
- [13] P. Welch, “The use of fast Fourier transform for the estimation of power spectra: A method based on time averaging over short, modified periodograms”, *IEEE Transactions on Audio and Electroacoustics*, vol. 15, no. 2, pp. 70–73, Jun. 1967. DOI: 10.1109/tau.1967.1161901.

- [14] O. Föllinger, *Regelungstechnik*. Vde Verlag GmbH, Jun. 2016, ISBN: 3800742012.
- [15] W. F. Guthrie, *NIST/SEMATECH e-Handbook of Statistical Methods (NIST Handbook 151)*, en, 2020. DOI: 10.18434/M32189.
- [16] M. Nasse, A. Bernhard, E. Bründermann, A. Böhm, S. Funkner, B. Härrer, I. Križnar, A. Malygin, S. Marsching, W. Mexner, A.-S. Müller, G. Niehues, R. Ruprecht, T. Schmelzer, M. Schuh, N. Smale, P. Wesolowski, and M. Yan, “First Electron Beam at the Linear Accelerator FLUTE at KIT”, en, *Proceedings of the 10th Int. Particle Accelerator Conf.*, vol. IPAC2019, Australia, 2019. DOI: 10.18429/JACOW-IPAC2019-MOPTS018.
- [17] M. Schuh, R. Aßmann, I. Birkel, A. Borysenko, H.-H. Braun, A. Böhm, M. Felber, K. Flöttmann, R. Ganter, N. Hiller, M. Hoffmann, E. Huttel, S. Höninger, V. Judin, S. Marsching, A.-S. Müller, S. Naknaimueang, M. Nasse, R. Rossmanith, R. Ruprecht, H. Schlarb, V. Schlott, M. Schwarz, L. Stingelin, M. Weber, and P. Wesolowski, “Status of FLUTE”, en, *Proceedings of the 5th Int. Particle Accelerator Conf.*, vol. IPAC2014, Germany, 2014. DOI: 10.18429/JACOW-IPAC2014-MOPR0066.
- [18] K. Batchelor, H. Kirk, J. Sheehan, M. Woodle, and K. McDonald, “Development of a high brightness electron gun for the Accelerator Test Facility at Brookhaven National Laboratory”, Jan. 1988. [Online]. Available: <https://www.osti.gov/biblio/7058521>.
- [19] J. Fraser, R. Sheffield, E. Gray, and P. Giles, “Photocathodes in accelerator applications”, Jan. 1987.
- [20] R. Bossart, H. Braun, M. Dehler, and J. C. Godot, “A 3 GHz photoelectron gun for high beam intensity”, Sep. 1995. [Online]. Available: <https://cds.cern.ch/record/288412>.
- [21] R. Bossart, H. Braun, M. Dehler, and J. C. Godot, “CLIC-note 297 - A 3 GHz photoelectron gun for high beam intensity”, 1996.
- [22] S. Höninger, “Charakterisierung der Elektronenquelle für den Linearbeschleuniger FLUTE”, PhD thesis, Karlsruhe Institute of Technology - IBPT, 2014.
- [23] G. Burt, *Introduction to RF for Accelerators*, T. C. Institute, Ed.
- [24] L. R. Dalesio, M. R. Kraimer, and A. J. Kozubal, “EPICS Architecture”, *ICALEPCS*, vol. 91, 1991.
- [25] Control System Studio. (2021). Control System Studio, [Online]. Available: <https://controlsystemstudio.org/about> (visited on 05/26/2021).
- [26] W. Mexner, E. Blomley, E. Bründermann, C. Fehlinger, A.-S. Müller, R. Ruprecht, T. Schmelzer, M. Schuh, N.-J. Smale, S. Marsching, and I. Kriznar, “Update on the status of the FLUTE control system”, en, 2018. DOI: 10.5445/IR/1000098087.
- [27] M. Newville and A. Gratton. (2019). PyEpics: Python Epics Channel Access, [Online]. Available: <https://cars9.uchicago.edu/software/python/pyepics3/>.
- [28] RadiaBeam, *Faraday Cups*. [Online]. Available: http://www.radiabeam.com/upload/catalog/pdf/14272334342015-03-24_faraday-cups.pdf.
- [29] P. Synotech, *PCB 421A25 Charge Amplifier*.
- [30] Mini-Circuits, *ZX73-2500+ Voltage Variable Attenuator*.
- [31] R. W. Waugh, “A Low-Cost Surface Mount PIN Diode π Attenuator”, vol. 35, no. 5, pp. 280–284, 1992.
- [32] The LXI Consortium. (May 29, 2021). LXI instrument communication, [Online]. Available: <https://www.lxistandard.org/about/vxi-11-and-lxi.aspx>.

- [33] A. Grönholm. (2021). Advanced Python Scheduler, [Online]. Available: <https://apscheduler.readthedocs.io/>.
- [34] L. Wang, *From plant data to process control : ideas for process identification and PID design*. London New York: Taylor & Francis, 2000, ISBN: 0748407014.
- [35] Kammeyer, *Digitale Signalverarbeitung Filterung und Spektralanalyse*. StuttgartLeipzig-Wiesbaden: Teubner, 2002, ISBN: 9783519461227.
- [36] A. Oppenheim, *Discrete-time signal processing*. Upper Saddle River, NJ: Pearson, 2010, ISBN: 9780131988422.
- [37] Åström and Hägglund, *PID controllers*. Research Triangle Park, N.C: International Society for Measurement and Control, 1995, ISBN: 1556175167.
- [38] S. Zacher and M. Reuter, *Regelungstechnik für Ingenieure*. Vieweg+Teubner Verlag, Dec. 7, 2010, 514 pp., ISBN: 9783834898371.
- [39] S. J. Dodds, *Feedback Control*. Springer-Verlag GmbH, Jul. 1, 2015, ISBN: 1447166744.
- [40] F. León, *Signale und Systeme*. BerlinBoston, Mass: De Gruyter Oldenbourg, 2015, ISBN: 9783110403855.
- [41] J. G. Ziegler and N. B. Nichols, “Optimum Settings for Automatic Controllers”, *Transactions of the ASME*, vol. 64, pp. 759–768, 1942.
- [42] I. D. Díaz-Rodríguez, S. Han, and S. P. Bhattacharyya, *Analytical Design of PID Controllers*. Springer International Publishing, May 29, 2019, 316 pp., ISBN: 3030182274.
- [43] The Mathworks. (Jun. 16, 2021). Open PID Tuner for PID tuning - MATLAB pidTuner, [Online]. Available: <https://de.mathworks.com/help/control/ref/pidtuner.html> (visited on 06/16/2021).
- [44] The Mathworks. (Jun. 16, 2021). PID Tuning Algorithm - MATLAB & Simulink, [Online]. Available: <https://de.mathworks.com/help/control/getstart/pid-tuning-algorithm.html> (visited on 06/16/2021).
- [45] R. Computing. (2021). PyQt, [Online]. Available: <https://riverbankcomputing.com/software/pyqt/> (visited on 06/17/2021).
- [46] The Qt Company. (2021). Qt Framework, [Online]. Available: <https://doc.qt.io/> (visited on 06/15/2021).
- [47] J. D. Hunter, “Matplotlib: A 2D graphics environment”, *Computing in Science & Engineering*, vol. 9, no. 3, pp. 90–95, 2007. DOI: 10.1109/MCSE.2007.55.
- [48] L. Campagnola. (2011). PyQtGraph - Scientific Graphics and GUI Library for Python, [Online]. Available: <https://www.pyqtgraph.org/> (visited on 06/14/2021).
- [49] The Qt Company. (2021). QTimer Class, [Online]. Available: <https://doc.qt.io/qt-5/qtimer.html> (visited on 06/12/2021).
- [50] C. Brosilow, *Techniques of model-based control*. Upper Saddle River, N.J: Prentice Hall, 2002, ISBN: 013028078X.
- [51] Y. Luo, W. Ren, Y. Huang, Q. He, Q. Wu, X. Zhou, and Y. Mao, “Feedforward Control Based on Error and Disturbance Observation for the CCD and Fiber-Optic Gyroscope-Based Mobile Optoelectronic Tracking System”, *Electronics*, vol. 7, no. 10, 2018, ISSN: 2079-9292. DOI: 10.3390/electronics7100223. [Online]. Available: <https://www.mdpi.com/2079-9292/7/10/223>.